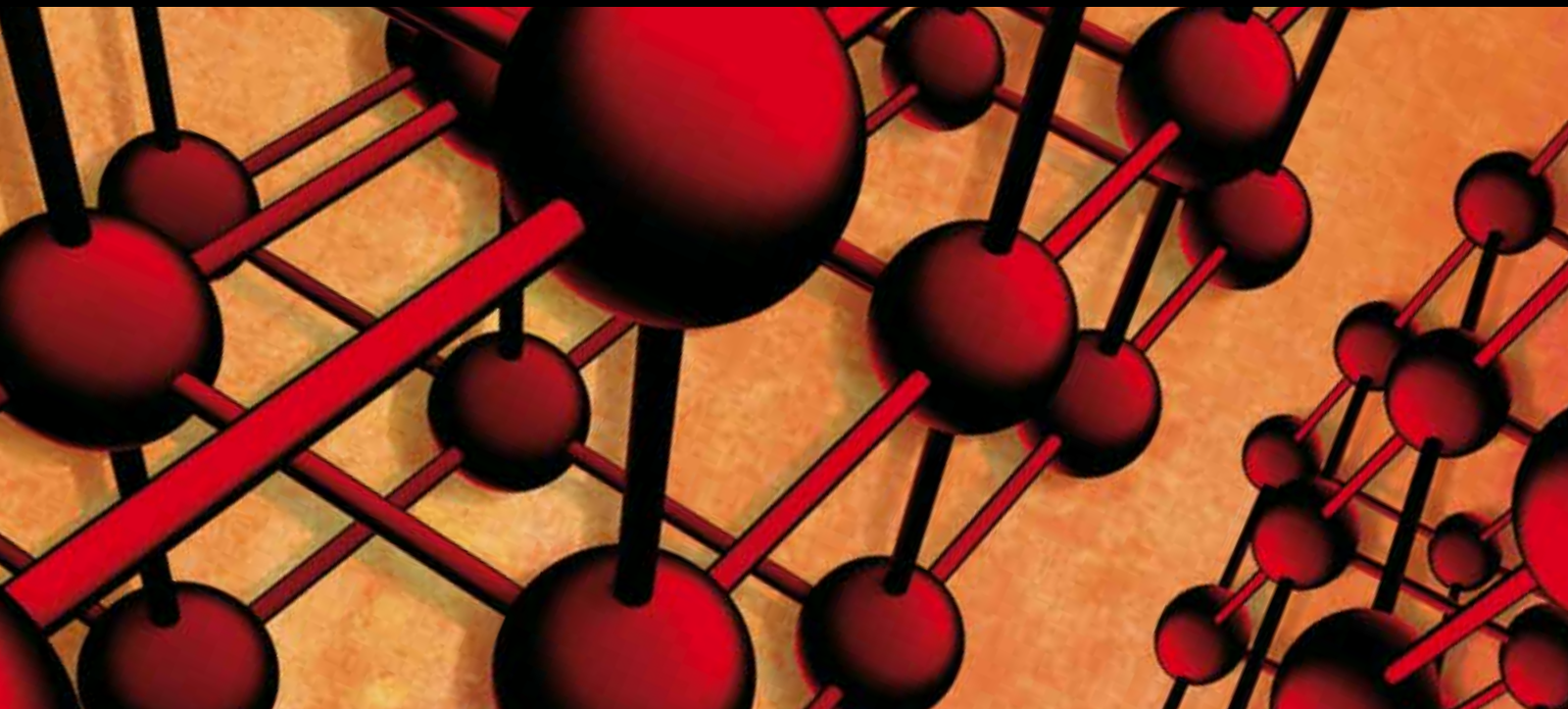


Nanostructured Materials for Microelectronic Applications

Guest Editors: Shou-Jinn Chang, Teen-Hang Meen, Stephen D. Prior,
Artde Donald Kin-Tak Lam, and Liang-Wen Ji





Nanostructured Materials for Microelectronic Applications

Advances in Materials Science and Engineering

Nanostructured Materials for Microelectronic Applications

Guest Editors: Shoou-Jinn Chang, Teen-Hang Meen,
Stephen D. Prior, Artde Donald Kin-Tak Lam,
and Liang-Wen Ji



Copyright © 2014 Hindawi Publishing Corporation. All rights reserved.

This is a special issue published in “Advances in Materials Science and Engineering.” All articles are open access articles distributed under the Creative Commons Attribution License, which permits unrestricted use, distribution, and reproduction in any medium, provided the original work is properly cited.

Editorial Board

K. G. Anthymidis, Greece
Robert S. Averbach, USA
Amit Bandyopadhyay, USA
Zoe Barber, UK
Yucel Birol, Turkey
Susmita Bose, USA
Steve Bull, UK
Peter Chang, Canada
Daolun Chen, Canada
Manish U. Chhowalla, USA
S. Chinnappanadar, India
Martin Crimp, USA
Jie Dai, Singapore
Chapal K. Das, India
João P. Davim, Portugal
Seshu B. Desu, USA
Yong Ding, USA
Sergi Gallego, Spain
John W. Gillespie, USA
Hiroki Habazaki, Japan
Richard Hennig, USA
Dachamir Hotza, Brazil
Chun-Hway Hsueh, Taiwan
Shyh-Chin Huang, Taiwan
Rui Huang, USA
Wei Huang, China
Jacques Huot, Canada
William A. Jesser, USA
Jaehwan Kim, Korea

Sridhar Komarneni, USA
Prashant Kumta, USA
Jui-Yang Lai, Taiwan
Pavel Lejcek, Czech Republic
Markku Leskela, Finland
Bin Li, China
Hai Lin, China
Yuanhua Lin, China
Zhimin Liu, China
Tao Liu, China
Jun Liu, China
Ying Liu, USA
Meilin Liu, Georgia
Yuan Liu, China
Gang Liu, China
Maria A. Loi, The Netherlands
Hai Lu, China
Peter Majewski, Australia
Shuichi Miyazaki, Japan
Paul Munroe, Australia
Ali Nazari, Iran
Luigi Nicolais, Italy
Tsutomu Ohzuku, Japan
Xiaoqing Pan, USA
Ganapathiraman Ramanath, USA
Raju V. Ramanujan, Singapore
Manijeh Razeghi, USA
Mohd Sapuan Salit, Malaysia
Jainagesh A. Sekhar, USA

Jiangbo Sha, China
Liyuan Sheng, China
You Song, China
Aloysius Soon, Korea
Charles C. Sorrell, Australia
Steven L. Suib, USA
Sam-Shajing Sun, USA
Weihua Tang, China
Achim Trampert, Germany
Vladimir Tsukruk, USA
Krystyn Van Vliet, USA
Rui Vilar, Portugal
Min Wang, China
Jörg M. K. Wiezorek, USA
Wei Wu, USA
Gongnan Xie, China
Aiguo Xu, China
Jianqiao Ye, UK
Yadong Yin, USA
Ming-Xing Zhang, Australia
Jian Zhang, Singapore
Kai Zhang, China
Kai Zhang, China
Rui Zhang, China
Tao Zhang, China
Bin Zhang, China
Jun Zhang, China
Yufeng Zhang, China
Jing Zhang, China

Contents

Nanostructured Materials for Microelectronic Applications, Shoou-Jinn Chang, Teen-Hang Meen, Stephen D. Prior, Artde Donald Kin-Tak Lam, and Liang-Wen Ji
Volume 2014, Article ID 383041, 1 page

Parametric Study of High-Efficiency and Low-Emission Gas Burners, Shuhn-Shyurng Hou and Ching-Hung Chou
Volume 2013, Article ID 154957, 7 pages

Design and Evaluation of Photo-Induced Biofeedback Fabric for the Enhancement in Sleeping Sense, Wei-Cheng Chu, Hsin-Ju Lin, and Shu-Ping Chiu
Volume 2013, Article ID 673123, 9 pages

Effects of Deep Cryogenic Treatment on Wear Mechanisms and Microthermal Expansion for the Material of Drive Elements, Yuh-Ping Chang, Gino Wang, Jeng-Haur Horng, Li-Ming Chu, and Yih-Chyun Hwang
Volume 2013, Article ID 945657, 7 pages

Effects of Nitride on the Tribological Properties of the Low Carbon Alloy Steel, Yuh-Ping Chang, Jin-Chi Wang, Jeng-Haur Horng, Li-Ming Chu, and Yih-Chyun Hwang
Volume 2013, Article ID 367543, 8 pages

Properties and Analysis of Transparency Conducting AZO Films by Using DC Power and RF Power Simultaneous Magnetron Sputtering, Neng-Fu Shih, Jin-Zhou Chen, and Yeu-Long Jiang
Volume 2013, Article ID 401392, 6 pages

Design and Fabrication of the Large Thrust Force Piezoelectric Actuator, Shyang-Jye Chang and Jing Chen
Volume 2013, Article ID 912587, 5 pages

The Creep Parameters of SAC305 Unleaded Solders, Chao-Ming Hsu, Ah-Der Lin, and Jao-Hwa Kuang
Volume 2013, Article ID 838075, 10 pages

An Experimental Study on Heat Conduction and Thermal Contact Resistance for the AlN Flake, Huann-Ming Chou, Jin-Chi Wang, and Yuh-Ping Chang
Volume 2013, Article ID 352173, 7 pages

Optical and Structural Properties of Titanium Dioxide Films from TiO_2 and Ti_3O_5 Starting Materials Annealed at Various Temperatures, Shih-Chang Shei
Volume 2013, Article ID 545076, 7 pages

Editorial

Nanostructured Materials for Microelectronic Applications

**Shoou-Jinn Chang,¹ Teen-Hang Meen,² Stephen D. Prior,³
Artde Donald Kin-Tak Lam,⁴ and Liang-Wen Ji⁵**

¹ Department of Electrical Engineering, Institute of Microelectronics, National Cheng Kung University, Tainan 701, Taiwan

² Department of Electronic Engineering, National Formosa University, Yunlin 632, Taiwan

³ Aeronautics, Astronautics and Computational Engineering, University of Southampton, Southampton SO17 1BJ, UK

⁴ College of Physics and Information Engineering, Fuzhou University, Fuzhou 350116, Fujian, China

⁵ Institute of Electro-Optical and Materials Science, National Formosa University, Yunlin 632, Taiwan

Correspondence should be addressed to Shoou-Jinn Chang; changsj@mail.ncku.edu.tw

Received 29 January 2014; Accepted 29 January 2014; Published 6 March 2014

Copyright © 2014 Shoou-Jinn Chang et al. This is an open access article distributed under the Creative Commons Attribution License, which permits unrestricted use, distribution, and reproduction in any medium, provided the original work is properly cited.

The Scope of the Special Issue. Nanostructured materials are a new class of materials, having dimensions in the 1~100 nm range, which provide one of the greatest potentials for improving performance and extended capabilities of products in a number of industrial sectors. Nanostructures can be divided into zero-dimensional (0D when they are quantum dot or nanoparticle structures), one-dimensional (1D when they are elongated), and two-dimensional (2D when they are planar) based on their shapes. The recent emphasis in the nanomaterials research has been on 1D nanostructures perhaps due to the intriguing possibility of using them in the majority of short-term future applications. The most successful examples are seen in the microelectronics, where “smaller” has always meant a greater performance ever since the invention of transistors, for example, higher density of integration, faster response, lower cost, and less power consumption. In recent years, applications of nanostructured nanomaterials on microelectronic devices have been a highly developing field, due to the flexibility and the light weight for daily use, which has the potential to be deployable. Therefore the fields of nanostructure devices have been the subject of reviews.

With the continuous downscaling of material technologies, reliability is more and more becoming a major bottleneck. First of all the electric fields and mechanical stress have increased continuously and are now reaching the maximum values that can be allowed for reliable operation. At this time,

we are introducing nanomaterials and a new design to maintain the effective performance scaling. Some materials like the low carbon alloy steel, transparency conducting AZO films, piezoelectric material, AlN flake, and titanium dioxide films have already been introduced and under investigation. These materials and devices often have unknown reliability behavior and/or introduce new failure mechanisms. In addition, the market is continuously demanding higher reliability levels for present technologies. The chance to share and discuss these crucial nanostructured materials for microelectronic developments is very important.

This special issue selects 9 papers about materials for microelectronic applications and other related fields. This special issue enables interdisciplinary collaboration between material science and engineering technologists in the academic and industrial fields.

Shoou-Jinn Chang
Teen-Hang Meen
Stephen D. Prior
Artde Donald Kin-Tak Lam
Liang-Wen Ji

Research Article

Parametric Study of High-Efficiency and Low-Emission Gas Burners

Shuhn-Shyurng Hou and Ching-Hung Chou

Department of Mechanical Engineering, Kun Shan University, Yung-Kang District, Tainan City 71003, Taiwan

Correspondence should be addressed to Shuhn-Shyurng Hou; sshou@mail.ksu.edu.tw

Received 25 September 2013; Accepted 8 October 2013

Academic Editor: Shouou-Jinn Chang

Copyright © 2013 S.-S. Hou and C.-H. Chou. This is an open access article distributed under the Creative Commons Attribution License, which permits unrestricted use, distribution, and reproduction in any medium, provided the original work is properly cited.

The objective of this study is to investigate the influence of three significant parameters, namely, swirl flow, loading height, and semi-confined combustion flame, on thermal efficiency and CO emissions of a swirl flow gas burner. We focus particularly on the effects of swirl angle and inclination angle on the performance of the swirl flow burner. The results showed that the swirl flow burner yields higher thermal efficiency and emits lower CO concentration than those of the conventional radial flow burner. A greater swirl angle results in higher thermal efficiency and CO emission. With increasing loading height, the thermal efficiency increases but the CO emission decreases. For a lower loading height (2 or 3 cm), the highest efficiency occurs at the inclination angle 15°. On the other hand, at a higher loading height, 4 cm, thermal efficiency increases with the inclination angle. Moreover, the addition of a shield can achieve a great increase in thermal efficiency, about 4-5%, and a decrease in CO emissions for the same burner (swirl flow or radial flow).

1. Introduction

Much attention has been paid to higher thermal efficiencies and lower emissions of domestic gas burners since the ever-increasing demand for energy saving and emission reduction [1–13]. As recognized, the domestic gas burner most extensively used is of the conventional Bunsen type (i.e., partially aerated) [6, 14, 15]. The typical partially aerated burner entrains primary air naturally by a momentum-sharing process between the high velocity gas jet and the ambient air [6]. The most popular fuel used in domestic gas burners is liquefied petroleum gas (LPG), which is also used in this work. Typically, designs of conventional domestic gas burners are mainly relied upon open combustion flame such that energy loss through the dispersion of the flue gas to the surroundings is very large, resulting in relatively low thermal efficiency [13]. Clearly, if the dispersion of the flame or flue gas to the surroundings can be prolonged, then the thermal efficiency can be improved.

Heat and mass transfer are strongly influenced by swirl in a number of natural and technological flows [16]. It has been shown that swirl flow had great potential to lengthen

the residence time and enhance mixing by means of the rotating flow field [10–13]. Swirl flows have been extensively used in many industrial furnaces and boilers as well as internal combustion engines as they can enhance mixing between fuel and oxidant and flame stabilization. However, most of the domestic gas burners are of nonswirl flow type, rather than swirl flow type. Therefore, in order to achieve high efficiency and low emissions, it is of great importance that the swirl flow in a domestic gas burner can be properly designed.

Recently, low-emission, energy-efficient gas burners have attracted much attention. However, there is still lack of studies on the flow type affecting burner performance, especially swirl flow. The objective of this study is to investigate the influence of swirl flow including swirl angle and inclination angle on the burner performance. Domestic gas burners with swirl flow are proposed by adjusting different values of swirl angle and inclination angle. Their thermal efficiencies and CO emissions characteristics will be discussed and compared with those of the conventional nonswirl flow burner. Furthermore, the influences of heating height (loading height) and semiconfined flame (shielded flame) on thermal efficiencies and CO emissions are explored. The results obtained herein

would be helpful for us to understand what parameters govern burner performance and to provide significant design or operation concepts of domestic gas cookers in real applications.

2. Experimental Setup and Method

Figure 1 schematically illustrates the experimental apparatus. LPG contained in a steel cylinder is used as fuel, which consists of 40% propane and 60% butane by volume with a higher heating value of 114 MJ/m³. A wet-gas meter is used to measure the flow rate of LPG. Meanwhile, a U-tube manometer is employed to regulate the supply pressure of LPG, which can be adjusted by the pressure regulator. In this study, a double-ring gas burner, which consists of a burner head (see Figure 2(a)) and outer- and inner-ring burner caps (made of copper), is adopted. The flow rates of outer- and inner-ring burner caps can be separately controlled by means of their own mixing tubes.

The port design of gas burner is the primary factor greatly influencing the flow type and in turn dominating the burner performance (thermal efficiency and emissions). In the present work, we only change the outer-ring flow type (radial flow (nonswirl flow) or swirl flow with various swirl angles and inclination angles) but keep the inner-ring flow type (radial flow) and the other remaining components the same. This is because the outer-ring flow supplies the major heat source and mainly governs the burner performance. As shown in Figure 2(b), the outer-ring burner cap has 50 ports with the same diameter of 0.0028 m along their circumference. Their axes are designed to be oriented towards the horizontal plane of the burner at an inclination angle, β , and thus their tangential projections at a swirl angle, α , with respect to the burner's radius can be generated. Accordingly, swirl flames can be formed in the outer-ring burner cap by supplying a primary air-LPG mixture through the burner ports. Figure 3(a) shows a typical rotating flame, which is produced by the flame jets emerging from the burner ports with swirl flow. Different values of swirl angle ($\alpha = 26, 36, 46, \text{ and } 56^\circ$) and inclination angle ($\beta = 10, 15, 20, \text{ and } 25^\circ$) are designed to access the influence of swirl flow on the burner performance. On the other hand, if $\alpha = 0^\circ$, then the conventional nonswirl flow burner (radial flow burner) is formed (see Figure 3(b)).

In addition to swirl flow, we also examine the effects of adding a shield enclosing the burner on improving thermal efficiency and reducing CO emission. The circular shield is made of stainless steel sheet, whose height is 0.11 m, inner diameter is 0.32 m, and thickness is 0.0008 m (see Figure 4) [15]. The shield has 15212 round holes of 0.00155 m diameter. The semiconfined combustion flame (with the circular shield enclosing the burner) has a potential to suppress the dispersion of the high temperature flame and flue gas, resulting in higher thermal efficiencies. Therefore, comparisons of thermal efficiencies and CO emissions for the semiconfined and open combustion flames are made.

As shown in Figure 5, the sampling and analysis system is adopted to measure the thermal efficiency and CO emission.

According to CNS standard [17], the variations of water temperature versus time were recorded by a *K*-type thermocouple, which is arranged at the midpoint of the water depth. The thermal efficiency of a gas burner is defined as the percentage of the thermal input transferred to the loading water, which can be determined by (1). In other words, it can be calculated by measuring the elapsed time for a standard load of water (4.4 kg) to be heated through a temperature rise of 50°C from the initial temperature (room temperature) and the corresponding fuel (LPG) consumed:

$$\eta = \frac{m \times C_p \times \Delta T}{Q \times \text{HHV}} \times 100\%, \quad (1)$$

where m (kg) denotes the mass of water, C_p (kJ/kg-°C) is the specific heat at constant pressure of water, ΔT equals 50°C, Q (m³) represents the consumption of LPG, and HHV (kJ/m³) designates the higher heating value of LPG.

The CO emissions are measured by a semicircular sampling tube that is located at 1/3 of the loading height from the top and 3 mm away from the edge of the loading vessel. A gas analyzer (Testo 350-XL) is used to continuously measure the concentrations of combustion products. The CO emission resulting from incomplete combustion is greatly taken into consideration because of the hazard of CO poisoning. In this study, CO* is employed to designate the CO emission, which is defined by the following equation [17]:

$$\text{CO}^* = \text{CO}_a \times \frac{\text{O}_{2t}}{\text{O}_{2t} - \text{O}_{2a}}, \quad (2)$$

where CO* is the theoretical CO concentration of dry combustion product, CO_a is the measured CO concentration, O_{2t} is the theoretical O₂ concentration in dry air, and O_{2a} is the measured O₂ concentration.

3. Results and Discussion

Variations of thermal efficiency and CO emission versus swirl angle at a fixed thermal input 4.75 kW for the open flame and semiconfined flame at fuel supply pressure $P = 280 \text{ mm H}_2\text{O}$ and loading height $L = 2.5 \text{ cm}$ are shown in Figures 6 and 7, respectively. As can be seen in Figures 6 and 7, for both open flames and semiconfined flames, the swirl flow burner gives higher thermal efficiency than the radial flow burner. As swirl angle is increased from 0° to 56°, the latter gives higher thermal efficiency than the former by at least 2% for the open flames (Figure 6) and semiconfined flames (Figure 7). The improvement in thermal efficiency of the swirl flow burner is mainly achieved by the increased heat transfer coefficient at the vessel bottom resulting from prolonged residence time of the combustion products in the vicinity of the vessel bottom [15]. Moreover, the enhancement in flow mixing and combustion process can be achieved owing to the rotating flow field [15]. Figures 6 and 7 also show that the addition of the shield yields a great increase in thermal efficiency, about 4-5%, for the same burner with swirl flow or radial flow at a fixed thermal input. The reason is that, as the dispersion of the flame or flue gas into the surroundings can be delayed

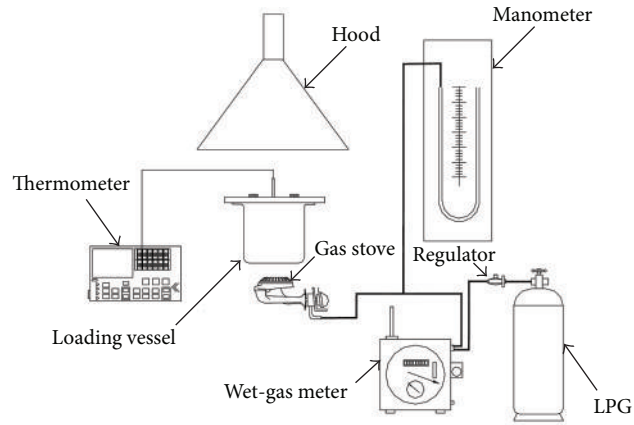


FIGURE 1: Schematic of the experimental apparatus.

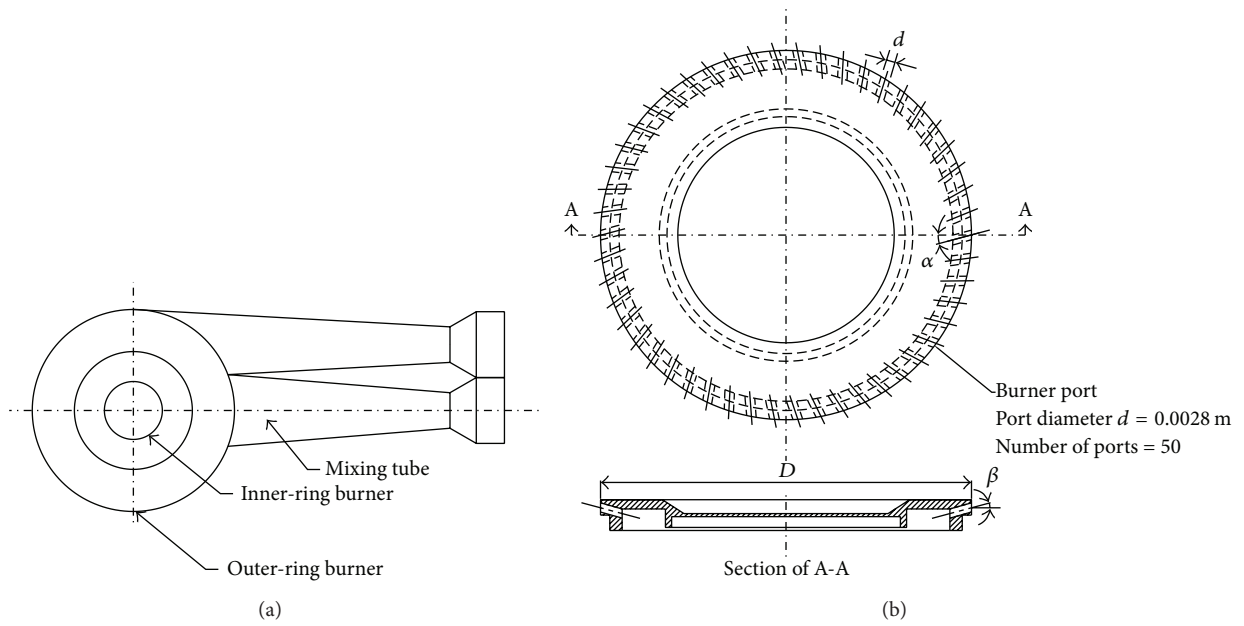


FIGURE 2: Schematic of (a) burner head and (b) outer-ring swirl flow burner.

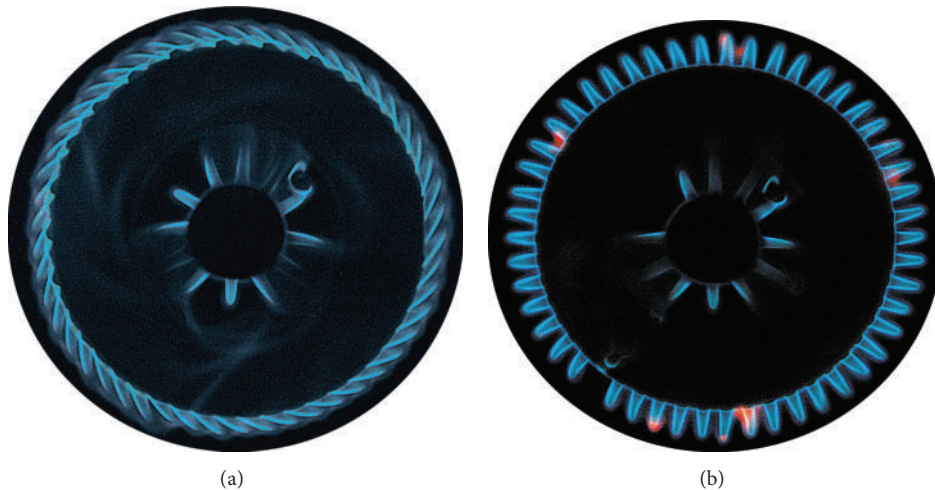
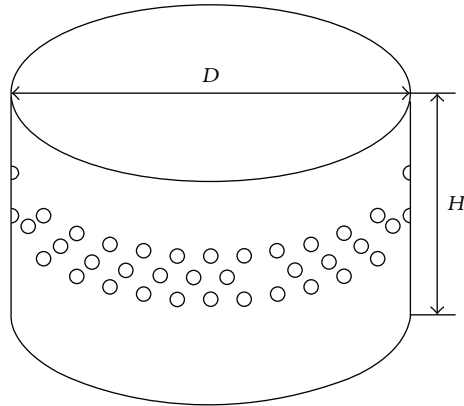


FIGURE 3: Top view of (a) swirling flame burner and (b) nonswirling flame burner.



Diameter of circular shield (D): 0.32 m

Thickness of circular shield (t): 0.0008 m

Height of circular shield (H): 0.11 m

Number of round holes (N): 15212

Diameter of round hole (D_H): 0.00155 m

FIGURE 4: Schematic diagram of the circular shield.

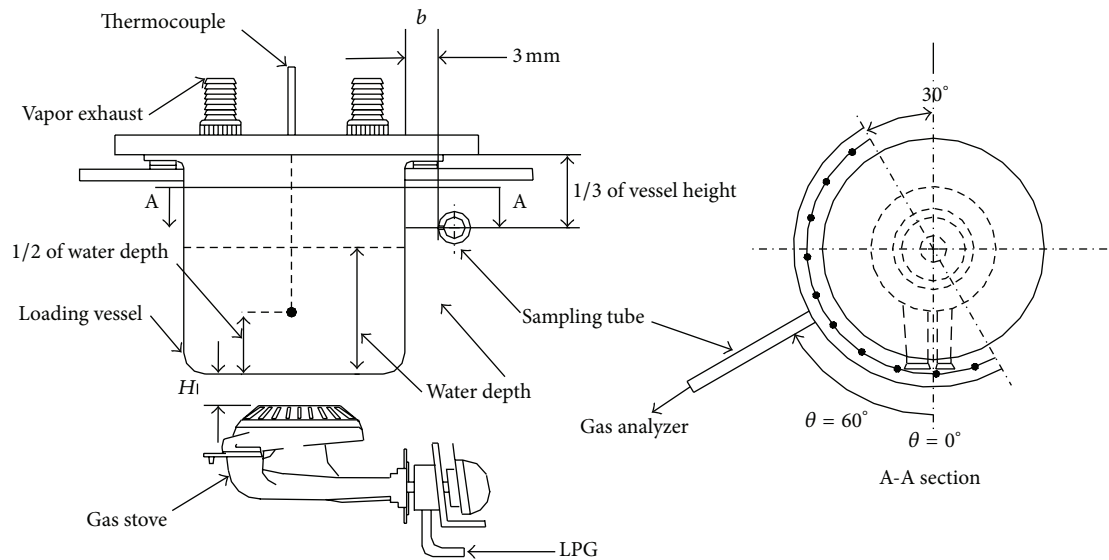


FIGURE 5: Schematic diagram of the sampling and analysis system.

by the shield, a significant improvement of thermal efficiency can be achieved.

Furthermore, it can be seen from the results of Figures 6 and 7 that the swirl flow burner produces slightly higher CO emission than the radial flow burner at fixed values of thermal input and loading height. The port shape of the swirl flow burner is elliptic, different from that of the radial flow burner, which is circular, along the circumference of the outer-ring burner. Therefore, the swirl flow burner has relatively narrow port spacing leading to slightly lower secondary aeration as compared with the radial flow burner. In comparison to the radial flow burner, however, enhanced mixing, extended residence time, and higher heat transfer coefficient between

the flame and the thermal load of the swirl flow burner greatly prevent incomplete combustion and eventually lead to only a relatively small increase in CO emissions.

Since loading height is an important design parameter, particular emphasis is now put on the impact of loading height (L) on thermal efficiency and CO emissions. In addition, inclination angle (β) is a significant port design parameter strongly affecting burner performance. Figures 8 and 9 demonstrate the influence of the inclination angle (β) and loading height (L) on the thermal efficiency and CO emission at a thermal input 4.75 kW for the open flame, respectively. Meanwhile, Figures 10 and 11 show the influence of the inclination angle (β) and loading height (L)

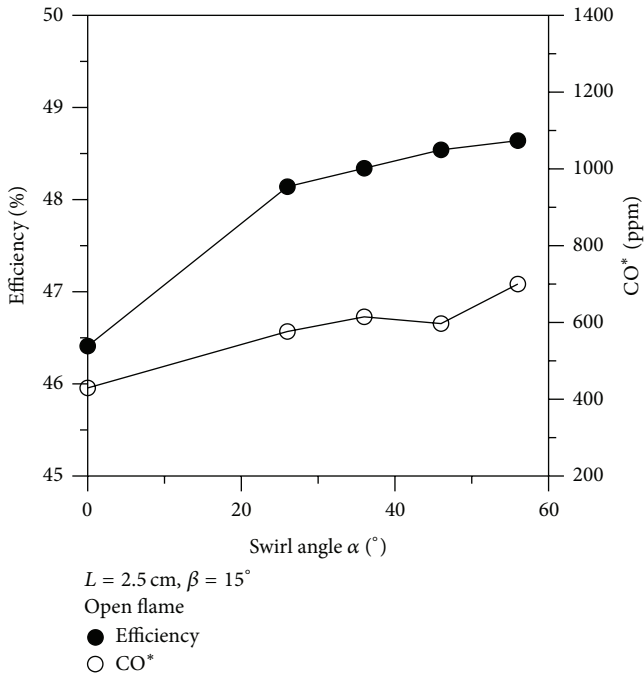


FIGURE 6: Effect of α on η and CO for open flames.

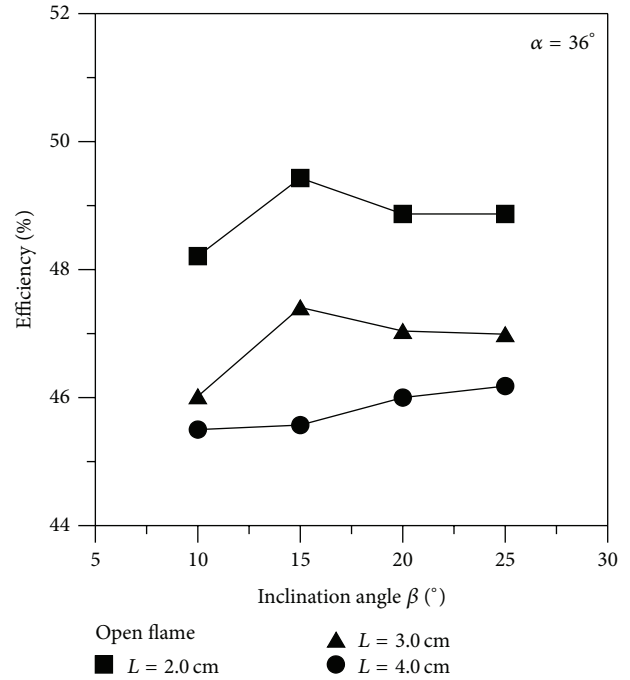


FIGURE 8: Effects of β and L on η for open flames.

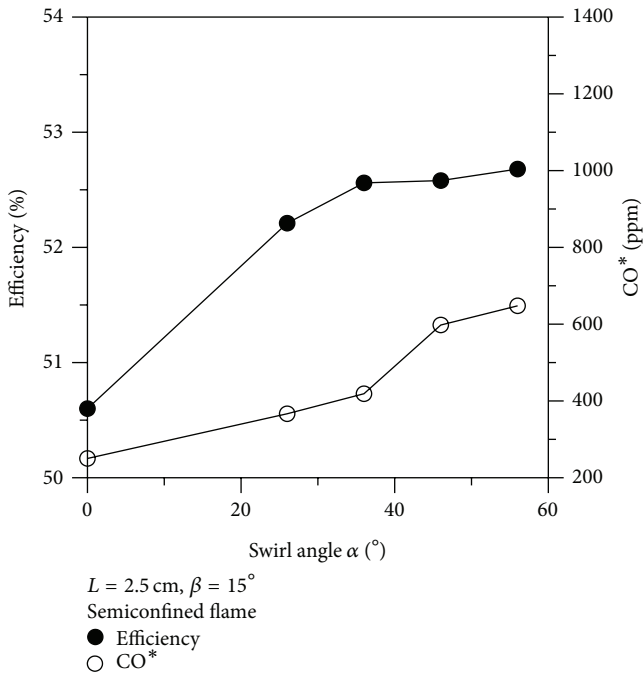


FIGURE 7: Effect of α on η and CO for semiconfined flames.

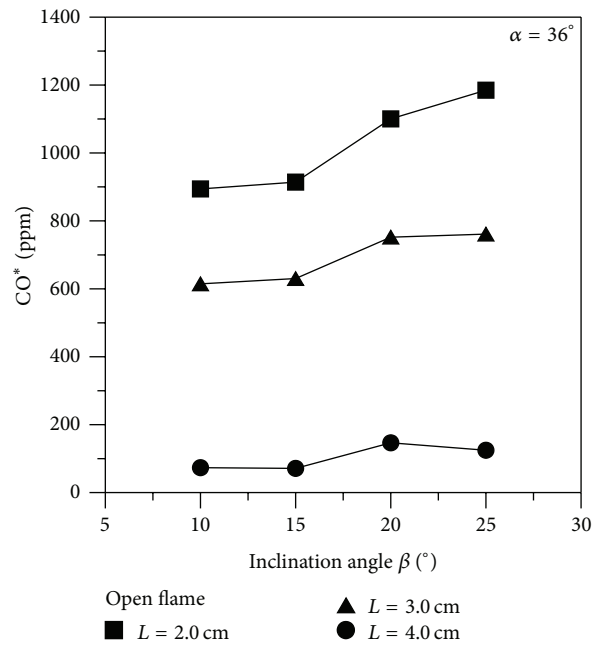


FIGURE 9: Effects of β and L on CO for open flames.

on the thermal efficiency and CO emission for the semiconfined flame, respectively. It can be found from the results of Figures 8–11 that an increase in loading height leads to a decrease in thermal efficiency and a reduction in CO emissions. At a higher loading height, the flame and combustion gases are cooled to a greater extent owing to flow mixing with ambient cool air before they contact the loading

vessel. Therefore, the temperature gradient for heat transfer is decreased.

On the other hand, as the loading height decreases, the slope of water temperature versus time becomes steeper due to an increase in flame impingement on the load such that a smaller amount of fuel consumption is required to heat up a load and higher thermal efficiency is achieved, as shown in Figures 8 and 10. Meanwhile, as loading height decreases,

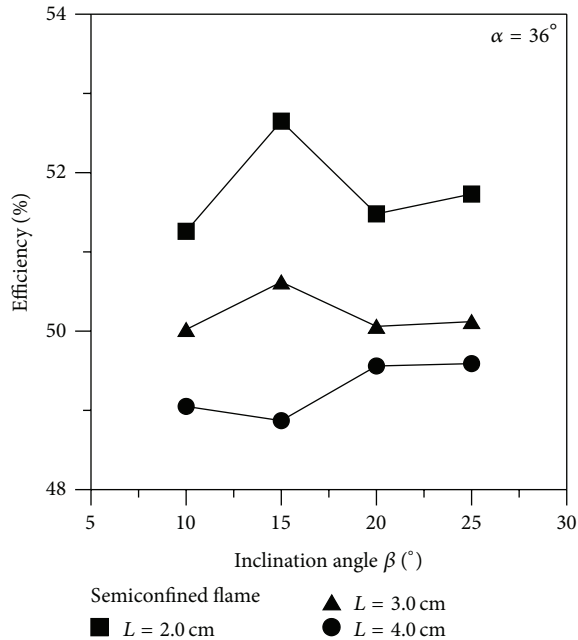


FIGURE 10: Effects of β and L on η for semiconfined flames.

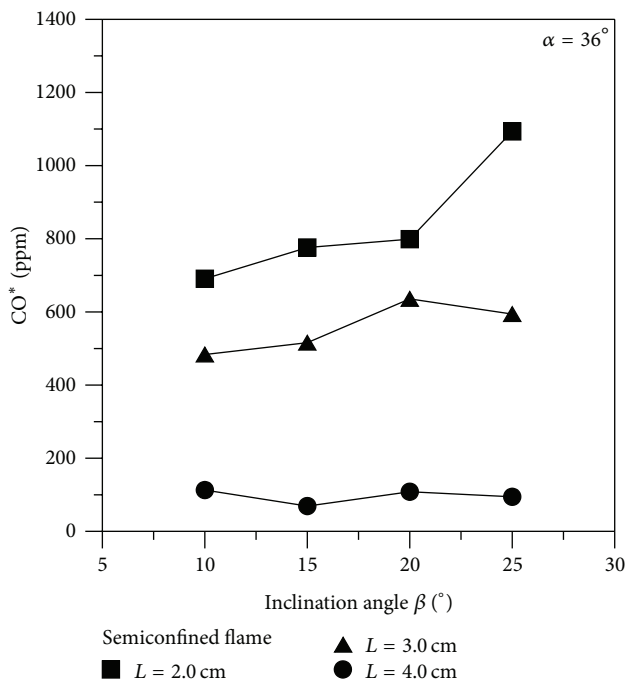


FIGURE 11: Effects of β and L on CO for semiconfined flames.

a larger amount of postflame gases is cooled as a result of contacting with the loading vessel. Consequently, incomplete combustion increases because of increased flame quenching by the load, leading to an increase in CO emission, as shown in Figures 9 and 11. These characteristics have also been observed by Ko and Lin [6].

It is also found from the results of Figures 8–11 that, for a lower loading height ($L = 2$ or 3 cm),

the highest efficiency occurs at $\beta = 15^\circ$. On the other hand, at a higher loading height ($L = 4$ cm), thermal efficiency increases with inclination angle β . The reason is that a greater inclination angle β corresponds to a longer flame and thus the temperature gradient for heat transfer is increased. Moreover, as can be seen, at a lower loading height ($L = 2$ or 3 cm), the CO emissions increase with an increase in inclination angle because of increased quenching (incomplete combustion) by the load, while, at a higher loading height ($L = 4$ cm), the CO emission is quite low and only slightly influenced by the inclination angle.

4. Conclusions

In this study, a domestic gas burner with swirling flames was adopted to investigate the significant parameters, namely, swirl angle, inclination angle, loading height, and shielded flame (semiconfined flame), affecting the burner performance. Concluding remarks are addressed as follows.

- (1) As swirl angle is increased from 0° to 56° , the latter gives higher thermal efficiency than the former by at least 2% for both open flames and semiconfined flames.
- (2) Generally, the increase in loading height results in a decrease in thermal efficiency and a reduction in CO emissions. The opposite holds for the decrease in loading height.
- (3) For a lower loading height ($L = 2$ or 3 cm), the highest efficiency occurs at the inclination angle $\beta = 15^\circ$, and the CO emission increases with an increase in inclination angle. On the other hand, at a higher loading height ($L = 4$ cm), thermal efficiency increases with inclination angle β but the CO emission is quite low and only slightly influenced by the inclination angle.
- (4) The addition of the shield yields a great increase in thermal efficiency, about 4–5%, and a decrease in CO emissions for the same burner (swirl flow or radial flow).

Conflict of Interests

The authors declare that there is no conflict of interests regarding the publication of this paper.

Acknowledgments

The authors greatly appreciate the financial support of this work by the Industrial Technology Research Institute and the National Science Council, Taiwan.

References

- [1] R. Junus, J. F. Stubington, and G. D. Sergeant, "Effects of design factors on emissions from natural gas cooktop burners," *International Journal of Environmental Studies*, vol. 45, no. 2, pp. 101–121, 1994.

- [2] J. F. Stubington, G. Beashel, T. Murphy, R. Junus, P. J. Ashman, and G. D. Sergeant, "Emissions and efficiency from production cooktop burners firing natural gas," *Journal of the Institute of Energy*, vol. 67, no. 473, pp. 143–155, 1994.
- [3] P. J. Ashman, R. Junus, J. F. Stubington, and G. D. Sergeant, "The effects of load height on the emissions from a natural gas-fired domestic cooktop burner," *Combustion Science and Technology*, vol. 103, pp. 283–298, 1994.
- [4] A. Y. Wagner, H. Livbjerg, P. G. Kristensen, and P. Glarborg, "Particle emissions from domestic gas cookers," *Combustion Science and Technology*, vol. 182, no. 10, pp. 1511–1527, 2010.
- [5] Y. C. Ko, S. S. Hou, and T. H. Lin, "Laminar diffusion flames in a multiport burner," *Combustion Science and Technology*, vol. 177, no. 8, pp. 1463–1484, 2005.
- [6] Y. C. Ko and T. H. Lin, "Emissions and efficiency of a domestic gas stove burning natural gases with various compositions," *Energy Conversion and Management*, vol. 44, no. 19, pp. 3001–3014, 2003.
- [7] S. S. Hou and Y. C. Ko, "Effects of heating height on flame appearance, temperature field and efficiency of an impinging laminar jet flame used in domestic gas stoves," *Energy Conversion and Management*, vol. 45, no. 9-10, pp. 1583–1595, 2004.
- [8] S. S. Hou and Y. C. Ko, "Influence of oblique angle and heating height on flame structure, temperature field and efficiency of an impinging laminar jet flame," *Energy Conversion and Management*, vol. 46, no. 6, pp. 941–958, 2005.
- [9] S. S. Hou, "Improvement in thermal efficiency and reduction in CO emissions of domestic gas burners via various heat transfer mechanisms," Final Report for ITRI, Industrial Technology Research Institute, Hsinchu, Taiwan, 2005 (Chinese).
- [10] A. Tamir, I. Elperin, and S. Yotzer, "Performance characteristics of a gas burner with a swirling central flame," *Energy*, vol. 14, no. 7, pp. 373–382, 1989.
- [11] A. Tamir, "A swirling-flame combustor for lean mixtures," *Combustion Science and Technology*, vol. 90, no. 1–4, pp. 193–209, 1993.
- [12] S. Jugjai, S. Tia, and W. Trewetaskorn, "Thermal efficiency improvement of an LPG gas cooker by a swirling central flame," *International Journal of Energy Research*, vol. 25, no. 8, pp. 657–674, 2001.
- [13] S. Jugjai and N. Rungsimuntuchart, "High efficiency heat-recirculating domestic gas burners," *Experimental Thermal and Fluid Science*, vol. 26, no. 5, pp. 581–592, 2002.
- [14] H. R. N. Jones, *The Application of Combustion Principles to Gas Burner Design*, British Gas, 1989.
- [15] S. S. Hou, C. Y. Lee, and T. H. Lin, "Efficiency and emissions of a new domestic gas burner with a swirling flame," *Energy Conversion and Management*, vol. 48, no. 5, pp. 1401–1410, 2007.
- [16] V. Shtern, A. Borissov, and F. Hussain, "Temperature distribution in swirling jets," *International Journal of Heat and Mass Transfer*, vol. 41, no. 16, pp. 2455–2467, 1998.
- [17] "The method of test for gas burning appliances of domestic use," CNS General no. 13605, The Chinese National Standard, 1995.

Research Article

Design and Evaluation of Photo-Induced Biofeedback Fabric for the Enhancement in Sleeping Sense

Wei-Cheng Chu,¹ Hsin-Ju Lin,¹ and Shu-Ping Chiu²

¹ Department of Fashion Design, Shu-Te University, No. 59, Hengshan Road, Yanchao District, Kaohsiung City 824, Taiwan

² Graduate School of Design Doctoral Program, National Yunlin University of Science and Technology, No. 672, Demin Road, Nanzi District, Kaohsiung City 811, Taiwan

Correspondence should be addressed to Wei-Cheng Chu; wjphilip@stu.edu.tw

Received 10 September 2013; Accepted 8 November 2013

Academic Editor: Shoou-Jinn Chang

Copyright © 2013 Wei-Cheng Chu et al. This is an open access article distributed under the Creative Commons Attribution License, which permits unrestricted use, distribution, and reproduction in any medium, provided the original work is properly cited.

Based on overcoming the sleeping obstacle for people, the purpose of this study is to design a photo-induced biofeedback fabric which is a kind of optical fiber fabric with the function of enhancing sleeping sense and to evaluate its effect. The fabrics with two layers including background layer and pattern layer were designed firstly. The pattern layers with 3 kinds of wavelengths of sine waves and the light controller with 3 kinds of flashing frequencies were then prepared. Guiding the light into the optical fiber, it will emit out of the optical fiber and stimulate our visual system to change the form of brain wave. Finally, EEG and sleeping scale were applied to evaluate the effect of enhancing sleeping sense. The results were shown that human's brain wave can be changed from sober status to shallow-sleeping status and the effect of enhancing sleeping sense can be achieved for all pattern layers in frequencies of 0, 5 and 10 Hz. Furthermore, female is more significant than male and participants age from 30 to 49 are the most significant. Besides, the stronger the participant's stress is, the more significant the sleeping sense is.

1. Introduction

According to the investigation of Taiwan Society of Sleep Medicine (TSSM), more than 4.5 million people have sleeping obstacle and 2.5 million people have suffered from chronic insomnia in Taiwan in 2006. Only a few people would like to consult doctors for this general issue. Therefore, how to enhance sleeping sense by using an effective and natural method has become an important issue and needs to be studied. Because the sleeping quality is strongly relative to stress [1, 2], stress relaxation and providing sound sleeping quality are the main aims of this paper.

In general, methods of stress relaxation are listed as follow: medical control treatment, exercise and homework treatment, breathing control treatment, musical treatment, Biofeedback treatment, and so forth [3, 4]. The principle of Biofeedback was adopted in this paper and was applied to train the people with sleeping obstacle to realize that it is their own ability to exercise self-control and self-adjustment, as well as it is also to make them understand that it is one's own responsibility to overcome this stress problem [5–7].

Referring to the aforesaid method of biofeedback treatment, a unique home decoration fabric with the functions of stress relaxation and sleeping sense enhancement was created by the combination of textile, photoelectric system, and medical technology. This is in a way with the hope to stimulate the activity of the brain wave by the light emitting out of the optical fibers which were weaved into fabric and sewn on it, other than by medication. It is expected that such innovation can release the stress exerted in our busy life and provide a new natural way choice of stress relaxation and enhancing sleeping sense for the people.

2. Materials and Methods

2.1. Biofeedback Fabrics Design. There are two layers in this biofeedback fabric including pattern layer and background layer. The background layer is woven with the warp and the weft densities of 36 ends per inch by 150 denier white synthetic filament yarn (SFY) and plastic optical fiber (POF) of 0.25 mm diameter. By sewing the Plastic Optical Fibers

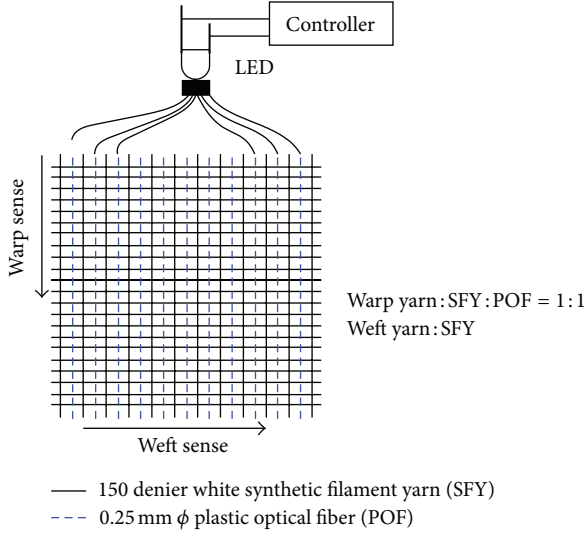


FIGURE 1: A design draft of background layer.

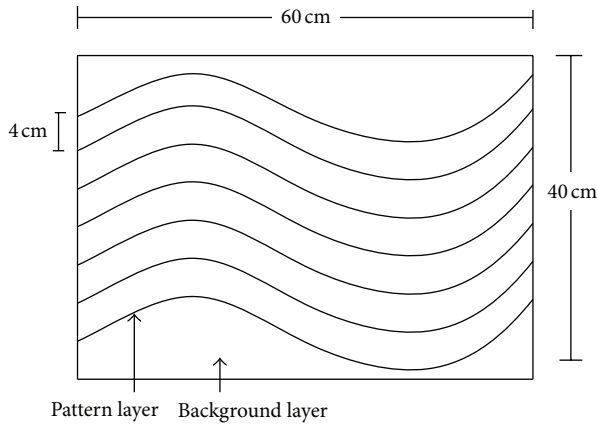


FIGURE 2: A design draft of pattern layer with $\lambda = 60$ cm sine wave.

(POFs) of 1.5 mm diameter on the surface of the background layer in a form of sine wave with various wavelengths as the pattern layer, the light can be guided into one end of the POFs and then emit out of the lateral of the POFs. The emitting light can stimulate a change of the brain wave by the reaction of man's visual system. Besides, a light controller was designed for obtaining various flashing frequencies of light. The details of the design for our study were described as follows.

(1) *Background Layer.* The background layer draft was shown in Figure 1. A plain weave fabric was applied to this background layer. The warp yarn of the background layer is composed of synthetic filament yarn and plastic optical fiber (POF) in ratio of 1:1 for color appearance in background layer. The weft yarn is applied with the same SFY as the warp yarn. All of the POFs of the warp yarn were gathered into

TABLE 1: Analysis of differences of the participants' brain waves in phases of f_1 , f_2 , and f_3 at resumed stages for all samples by ANOVA test.

Sample	Brain wave		f_1	f_2	f_3	F	P
Sample 1	B ₁	M	4.99	5.19	4.76	.201	.818
	Alpha	SD	2.20	2.73	2.94		
	B ₂	M	3.90	4.14	3.89	.310	.734
	Beta	SD	1.36	1.31	1.46		
	B ₃	M	3.52	3.69	3.29	.498	.610
	Theta	SD	1.42	1.64	1.64		
	B ₄	M	6.36	7.37	6.21	.824	.442
	Delta	SD	3.50	4.23	3.69		
Sample 2	B ₁	M	6.00	6.09	5.93	.035	.966
	Alpha	SD	2.32	2.28	2.33		
	B ₂	M	4.13	4.23	4.38	.458	.634
	Beta	SD	0.86	1.01	1.15		
	B ₃	M	4.08	4.30	4.16	.303	.739
	Theta	SD	1.04	1.16	1.15		
	B ₄	M	4.27	8.61	7.88	.820	.444
	Delta	SD	3.19	4.98	4.27		
Sample 3	B ₁	M	5.93	5.89	5.65	.128	.880
	Alpha	SD	2.26	2.31	2.28		
	B ₂	M	4.52	4.39	4.27	.395	.675
	Beta	SD	1.02	1.10	1.08		
	B ₃	M	4.29	4.30	4.49	.165	.848
	Theta	SD	1.01	1.14	2.06		
	B ₄	M	6.89	7.76	7.79	.931	.398
	Delta	SD	2.62	3.50	2.51		

a strand and connected to a 0.3 watt natural LED light with a flashing frequency adjusted by a light controller.

(2) *Pattern Layer.* The pattern layer draft was shown in Figure 2. For the curvature of pattern layer, plural sine waves with wavelengths (λ) of 60 cm in sample 1 (S_1), 30 cm in sample 2 (S_2), and 10 cm in sample 3 (S_3) in a ratio of amplitude to wavelength 1 : 2, were arranged horizontally with a distance of 4 cm between each line. The plastic optical fibers of 1.5 mm diameter with significant side emitting light characteristic were sewn on the background layer with transparent Polyamide 6 filament yarns of 0.2 mm diameter. All of the POFs of pattern layer were gathered into a strand and connected to a 0.3 watt blue LED light with a flashing frequency adjusted by a light controller.

(3) *Light Controller.* There are four types of light intensities and were provided including dark, glimpse, moderate, and strong. Besides, three types of the flashing frequencies were provided including 0 HZ (f_1), 5 HZ (f_2), and 10 HZ (f_3). The LED can be connected with the strand of POFs by using a black thermoplastic tube.

TABLE 2: Analysis of brain wave differences between resumed stage (RS) and stimulated stage (SS) in phases of f_1 , f_2 , and f_3 for all samples by t -test.

Sample	f_1	M	SD	t	P	f_2	M	SD	t	P	f_3	M	SD	t	P			
Sample 1	B ₁	RS	4.99	2.80	2.637	.110	B ₁	RS	5.19	2.73	2.853	.007	B ₁	RS	4.76	2.94		
		SS	3.68	1.59				SS	3.56	1.50				SS	3.41	1.71		
	B ₂	RS	3.90	1.36	-3.37	.737	B ₂	RS	4.14	1.31	.520	.605	B ₂	RS	3.98	1.45	-4.520	.653
		SS	4.03	1.52				SS	3.95	1.41				SS	4.06	1.47		
	B ₃	RS	3.52	1.42	-3.189	.003	B ₃	RS	3.69	1.64	-2.502	.015	B ₃	RS	3.29	1.64	-2.765	.008
		SS	5.30	2.69				SS	4.92	2.13				SS	4.67	2.18		
	B ₄	RS	6.36	3.50	-4.664	.000	B ₄	RS	7.37	4.23	-3.830	.000	B ₄	RS	6.21	3.69	-3.993	.000
		SS	14.11	8.40				SS	12.68	6.30				SS	11.58	6.37		
Sample 2	B ₁	RS	6.00	2.32	4.039	.000	B ₁	RS	6.09	2.28	4.651	.000	B ₁	RS	5.93	2.33	4.372	.000
		SS	4.12	1.06				SS	3.97	.99				SS	3.91	.97		
	B ₂	RS	4.13	.86	-1.241	.219	B ₂	RS	4.23	1.01	-.062	.951	B ₂	RS	4.38	1.15	.377	.708
		SS	4.47	1.23				SS	4.25	1.02				SS	4.26	1.26		
	B ₃	RS	4.08	1.04	-3.498	.001	B ₃	RS	4.30	1.16	-2.765	.008	B ₃	RS	4.16	1.14	-3.793	.000
		SS	5.64	2.20				SS	5.47	1.99				SS	5.79	2.05		
	B ₄	RS	7.21	3.19	-5.369	.000	B ₄	RS	8.61	4.98	-3.754	.000	B ₄	RS	7.88	4.27	-4.814	.000
		SS	15.01	7.28				SS	14.45	6.91				SS	14.80	6.62		
Sample 3	B ₁	RS	5.93	2.26	.429	.669	B ₁	RS	5.89	2.31	4.140	.000	B ₁	RS	5.65	2.28	3.789	.000
		SS	5.33	2.30				SS	3.95	1.09				SS	3.82	1.34		
	B ₂	RS	4.52	1.02	.830	.410	B ₂	RS	4.39	1.10	.135	.893	B ₂	RS	4.27	1.08	.085	.932
		SS	4.29	1.08				SS	4.35	1.16				SS	4.25	1.26		
	B ₃	RS	4.29	1.01	-3.208	.003	B ₃	RS	4.30	1.14	-2.847	.007	B ₃	RS	4.49	2.06	-1.481	.144
		SS	5.65	2.07				SS	5.64	2.31				SS	5.33	2.34		
	B ₄	RS	6.89	2.62	-4.897	.000	B ₄	RS	7.76	3.50	-4.228	.000	B ₄	RS	7.79	2.51	-3.728	.001
		SS	14.87	8.26				SS	14.69	8.26				SS	12.77	6.86		

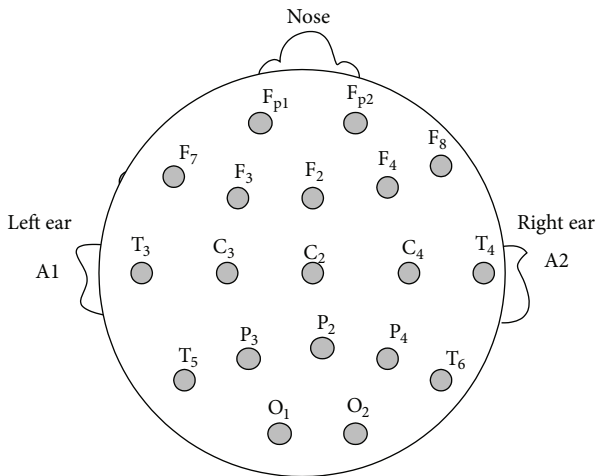


FIGURE 3: Brain wave potential position.

2.2. Evaluating Procedure and Method

(1) *Biofeedback Apparatus for Measuring Brain Wave.* This experiment used PED international Limited Electroencephalogram (EEG) measurement instrument model no: 1-330C-2, J + J engineering as the main equipment to measure

and collect data. This instrument is equipped with Physiobal USE3'S Software for data storing and data analyzing.

This experiment sets the brain wave into 4 categories as follows:

- (1) B₁ is Alpha wave ranged from 8 to 14 HZ;
- (2) B₂ is Beta wave ranged from 14 to 40 HZ;
- (3) B₃ is Theta wave ranged from 4 to 8 HZ;
- (4) B₄ is Delta wave ranged from 0.4 to 4 HZ.

The brain wave electrodes are located in F8 as positive, A2 as negative behind the right ear, and A1 as ground behind the left ear as shown in Figure 3. The biofeedback reaction will go into the encoder unit via the above said EEG measurement instrument. The brain wave reaction of the participant will simultaneously indicate on the computer screen.

(2) *Sleeping Scale.* We widely collected 130 adjectives related to sleeping sense and relaxation from the literature. The 21 preferable adjectives were selected by using KJ (Kawakita Jiro) method which is a grouping method performed by 6 members. Finally, 7 adjectives were chosen including Relaxed (Q1), Soft (Q2), Comfortable (Q3), Stretchable (Q4), Light (Q5), Free (Q6), and Sleepy (Q7); those 21 adjectives by using SDT (Semantic Differential Technique) of 5 scales performed by 30 subjects. After transferring these 7 adjectives into 7 questions and a sleeping scale of SDT with 11 scales (0 to 10),

TABLE 3: Analysis of brain wave differences among f_1 , f_2 , and f_3 for all samples at stimulated stage by ANOVA test.

Sample	Brain wave		f_1	f_2	f_3	F	P
Sample 1	B ₁	M	3.68	3.56	3.41	.224	.799
	Alpha	SD	1.59	1.50	1.71		
	B ₂	M	4.03	3.96	4.06	.041	.960
	Beta	SD	1.52	1.41	1.47		
	B ₃	M	5.30	4.92	4.67	.537	.587
	Theta	SD	2.69	2.13	2.18		
	B ₄	M	14.11	12.68	11.58	.962	.386
	Delta	SD	8.40	6.30	6.37		
Sample 2	B ₁	M	4.12	3.97	3.91	.316	.730
	Alpha	SD	1.06	.99	.97		
	B ₂	M	4.47	4.25	4.26	.333	.717
	Beta	SD	1.23	1.02	1.26		
	B ₃	M	5.64	5.47	5.79	.178	.838
	Theta	SD	2.20	1.99	2.05		
	B ₄	M	15.04	14.45	14.80	.050	.951
	Delta	SD	7.28	6.91	6.62		
Sample 3	B ₁	M	5.33	3.95	3.82	1.117	.332
	Alpha	SD	1.30	1.09	1.34		
	B ₂	M	4.29	4.35	4.25	.058	.944
	Beta	SD	1.08	1.16	1.26		
	B ₃	M	5.65	5.64	5.33	.191	.827
	Theta	SD	2.07	2.31	2.35		
	B ₄	M	14.87	14.69	12.77	.653	.523
	Delta	SD	8.53	8.26	6.86		

they were utilized to evaluate the sleeping sense in this study. For further data analysis, the 6 questions of Q1 to Q6 can be grouped together standing for Relaxed as Q1–Q6 expressed in Table 9 to Table 12.

(3) *Evaluating Procedure.* The evaluating procedure of this experiment was shown in Figure 4 and described below.

- (1) 5 minutes before the evaluation is conducted, the participants have to be informed of the purpose and the procedure in preparation stage and the samples should be prepared as showed in Figure 5.
- (2) For the comparison of sleeping sense after the stimulated stage, filling sleeping scale is conducted in 1 minute before starting the resumed stage.
- (3) Closing the eyes and taking a rest for 3 minutes is necessary in resumed stage (RS), it can assure that the participant's condition has recovered from the former evaluated stage (SS).
- (4) In the stimulated stage (SS), the participants open their eyes and look at the biofeedback fabric for 3 minutes. During this period of time, the participants' visual system will be stimulated and their brain waves

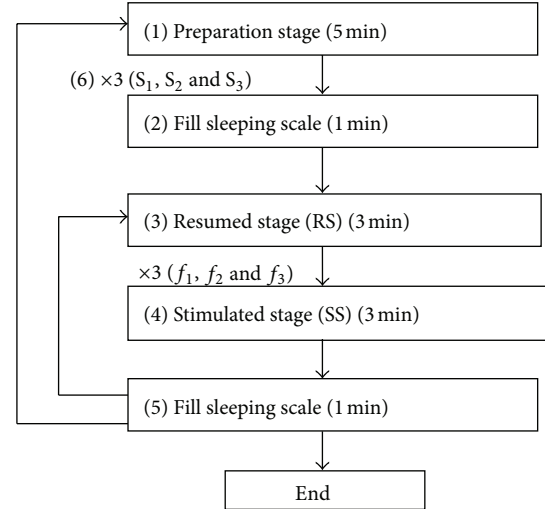


FIGURE 4: A flow chart of the evaluating procedure with EEG instrument and sleeping scale.

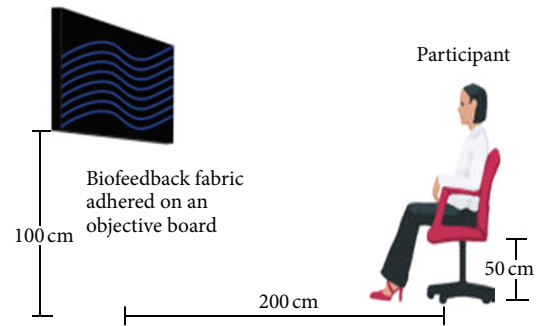


FIGURE 5: An illustration of the relative position in evaluation room.

was changed and then recorded at every 10-seconds interval.

- (5) Filling sleeping scale in 1 minute after each stimulated stage for the comparison of sleeping sense and repeating (3) to (5) steps for 3 types of the flashing frequencies (f_1 , f_2 , and f_3) of the biofeedback fabric are done, and then the experiment is completed for every single sample.
- (6) Repeating (2) to (5) steps for all the 3 samples of the different curvatures (S_1 , S_2 , and S_3) of biofeedback fabric are done, and then the experiment is completed for single subject.

(4) *Evaluating Condition.* Before the starting of this experiment, the relevant conditions and factors which may affect the result of the experiment should be kept constantly and remained throughout the whole experiment. The biofeedback fabric is placed at 100 cm above the ground level and the distance between the biofeedback fabric and participant is 200 cm. The participant sits straight at eyes level with the objective board in horizontal level as shown in Figure 5. The light strength of the evaluating room is kept under 0.001 lx. The participant should be motionless, keeping silence and

TABLE 4: Analysis of female brain wave differences between resumed stage and stimulated stage in phases of f_1 , f_2 , and f_3 by t -test.

f_1	M	SD	t	P	f_2	M	SD	t	P	f_3	M	SD	t	P			
B ₁	RS	4.841	1.899	2.544	.017	B ₁	RS	5.091	2.754	2.342	.031	B ₁	RS	4.773	2.601	1.944	.062
	SS	3.320	1.324				SS	3.293	1.119				SS	3.273	1.464		
B ₂	RS	4.075	1.597	-0.370	.970	B ₂	RS	4.028	1.424	-0.033	.974	B ₂	RS	3.998	1.332	-4.290	.671
	SS	4.098	1.812				SS	4.046	1.582				SS	4.224	1.547		
B ₃	RS	3.313	1.461	-2.654	.013	B ₃	RS	3.390	1.614	-2.485	.019	B ₃	RS	3.311	1.542	-2.488	.019
	SS	5.373	2.628				SS	4.946	1.811				SS	4.998	2.127		
B ₄	RS	6.481	4.502	-3.489	.002	B ₄	RS	6.927	4.667	-3.282	.003	B ₄	RS	6.183	3.704	-3.690	.001
	SS	15.095	8.436				SS	12.790	5.106				SS	12.981	6.098		

TABLE 5: Analysis of male brain wave differences between resumed stage and stimulated stage in phases of f_1 , f_2 , and f_3 by t -test.

f_1	M	SD	t	P	f_2	M	SD	t	P	f_3	M	SD	t	P			
B ₁	RS	5.155	2.538	1.372	.181	B ₁	RS	5.296	2.806	1.685	.103	B ₁	RS	4.750	3.333	1.202	.242
	SS	4.055	1.791				SS	3.844	1.809				SS	3.549	1.970		
B ₂	RS	3.737	1.115	-.532	.599	B ₂	RS	4.258	1.227	.840	.408	B ₂	RS	3.791	1.618	-.208	.837
	SS	3.965	1.236				SS	3.873	1.280				SS	3.907	1.430		
B ₃	RS	3.735	1.412	-1.816	.084	B ₃	RS	4.001	1.673	-1.172	.251	B ₃	RS	3.271	1.801	-1.440	.161
	SS	5.227	2.851				SS	4.908	2.485				SS	4.350	2.275		
B ₄	RS	6.238	2.267	-3.019	.008	B ₄	RS	7.822	3.853	-2.184	.040	B ₄	RS	6.237	3.823	-2.018	.053
	SS	13.133	8.550				SS	12.579	7.502				SS	10.180	6.532		

quiet in the evaluating room in order not to be disturbed. A total of 30 participants are divided into 3 groups by age in this experiment. The age of the first group (Age 1) is 18 to 29, the second group (Age 2) is 30 to 49, and the third group (Age 3) is 50 to 65. Each group consists of 10 participants; male and female are in the same quantity.

3. Results and Discussions

The EEG instrument was applied to measure the brain wave's strength at different flashing frequencies and to evaluate the biological state of the participants at resumed stage and stimulated stage. The measuring data obtained will be further analyzed and compared based on different stimulation condition, participant's age, and gender. Therefore, all the participants' brain waves need to be stabilized at resumed stage of phases of f_1 , f_2 , and f_3 for the comparison of stimulated stage. The participants' brain waves at resumed stage of phases of f_1 , f_2 , and f_3 for sample 1, sample 2, and sample 3 were shown in Table 1. The P values of the differences among all the phases of f_1 , f_2 , and f_3 for all samples and all brain waves (B₁, B₂, B₃, and B₄) are all larger than 0.05; that is, there are no significant differences of their brain wave activities in all phases according to ANOVA test. We can confirm that the brain wave after 3 minutes rest of closing eyes can be stabilized and be able to resume the original status before starting the measurement of stimulated stage.

(1) *Analysis of Brain Wave at Different Stimulated Stage.* The brain wave differences between the resumed stage (RS) and

the stimulated stage (SS) in phases of f_1 , f_2 , and f_3 were analyzed according to the t -test. The results were listed in Table 2 and described as follows. For all the phases of f_1 , f_2 , and f_3 , Alpha waves (B₁) are decreased significantly and transferred into Theta wave (B₃) and Delta wave (B₄) standing for the slight sleeping status. The less the brain wave's frequency (e.g., B₄ < B₃), the more significant increasing is the brain wave's strength (e.g., B₄ > B₃); that is, the reaction of the brain wave can be changed when the participants was stimulated by the light out of the optical fiber in biofeedback fabric, as well as the brain wave strength is more obviously and easily enhanced for the lower frequency of brain wave. The results demonstrated that the brain wave can be changed and reached to a status of slight sleeping (B₄ and B₃) from relaxation status (B₁). As to the high frequency of the Beta wave (B₂), standing for the exciting and sobering status, there is no significant difference between the resumed stage and the stimulated stage because the participants' original status is relaxant. The further analyses of brain waves at the stimulated stage in different flashing frequencies were listed in Table 3. For all the brain waves of B₁, B₂, B₃, and B₄, there are no significant differences among the 3 different flashing frequencies according to ANOVA test. The results showed that the biofeedback fabrics in conditions of 3 kinds of flashing frequencies are all effective.

(2) *Analysis of Brain Wave for Male and Female at Different Stimulated Stage.* The analyses of brain wave strength for female and male at different flashing frequencies were listed in Tables 4 and 5. For female brain waves at different flashing frequencies, their Alpha waves showed slight decreasing and their Theta wave and Delta wave showed significant

TABLE 6: Analysis of brain waves differences between resumed stage and stimulated stage for Age 1 group in phases of f_1 , f_2 , and f_3 by t -test.

f_1		M	SD	t	P	f_2		M	SD	t	P	f_3		M	SD	t	P
B ₁	RS	5.255	2.035	1.876	.078	B ₁	RS	5.023	2.371	1.886	.076	B ₁	RS	4.914	2.610	1.621	.122
	SS	3.616	1.342				SS	3.430	1.230				SS	3.364	1.525		
B ₂	RS	3.897	1.441	.065	.949	B ₂	RS	3.735	1.279	-.215	.832	B ₂	RS	3.506	1.244	-.966	.347
	SS	3.851	1.719				SS	3.878	1.671				SS	4.113	1.550		
B ₃	RS	3.752	1.474	-1.187	.251	B ₃	RS	3.690	1.509	-.786	.442	B ₃	RS	3.585	1.677	-.810	.428
	SS	4.798	2.365				SS	4.259	1.723				SS	4.272	2.092		
B ₄	RS	8.142	4.585	-1.641	.118	B ₄	RS	8.795	4.816	-1.011	.326	B ₄	RS	7.349	4.204	-1.463	.161
	SS	13.215	8.631				SS	11.002	4.950				SS	10.763	6.062		

TABLE 7: Analysis of brain waves differences between resumed stage and stimulated stage for Age 2 group in phases of f_1 , f_2 , and f_3 by t -test.

f_1		M	SD	t	P	f_2		M	SD	t	P	f_3		M	SD	t	P
B ₁	RS	4.946	2.749	.829	.418	B ₁	RS	5.185	3.213	1.139	.269	B ₁	RS	4.975	3.178	1.141	.269
	SS	4.009	2.878				SS	3.791	2.156				SS	3.597	2.117		
B ₂	RS	3.597	1.340	-.659	.518	B ₂	RS	4.100	1.502	.219	.829	B ₂	RS	4.121	1.634	.357	.725
	SS	4.020	1.523				SS	3.949	1.587				SS	3.861	1.623		
B ₃	RS	3.424	1.668	-2.434	.026	B ₃	RS	3.484	1.798	-2.356	.030	B ₃	RS	3.324	1.643	-2.319	.032
	SS	6.280	3.315				SS	5.772	2.489				SS	5.448	2.386		
B ₄	RS	5.703	3.068	-3.678	.006	B ₄	RS	6.777	3.960	-3.192	.005	B ₄	RS	6.595	3.466	-3.128	.006
	SS	16.160	9.302				SS	15.007	7.128				SS	13.945	6.574		

TABLE 8: Analysis of brain waves differences between resumed stage and stimulated stage for Age 3 group in phases of f_1 , f_2 , and f_3 by t -test.

f_1		M	SD	t	P	f_2		M	SD	t	P	f_3		M	SD	t	P
B ₁	RS	4.793	1.974	1.949	.067	B ₁	RS	5.373	2.840	1.978	.063	B ₁	RS	4.395	3.272	.976	.342
	SS	3.437	.972				SS	3.485	1.023				SS	3.271	1.603		
B ₂	RS	4.223	1.382	-.002	.999	B ₂	RS	4.594	1.112	1.113	.281	B ₂	RS	4.057	1.547	-.254	.802
	SS	4.224	1.464				SS	4.052	1.066				SS	4.223	1.370		
B ₃	RS	3.396	1.237	-1.735	.100	B ₃	RS	3.913	1.761	-.978	.341	B ₃	RS	2.964	1.738	-1.556	.137
	SS	4.821	2.284				SS	4.750	2.054				SS	4.302	2.091		
B ₄	RS	5.234	1.929	-3.072	.012	B ₄	RS	6.552	3.922	-2.269	.036	B ₄	RS	4.685	3.195	-2.359	.034
	SS	12.961	7.717				SS	12.044	6.575				SS	10.033	6.417		

TABLE 9: Analysis of sleeping scale differences between f_0 and after stimulated in phases of f_1 , f_2 , and f_3 by t -test for sample 1, sample 2, and sample 3.

Sample 1	M	SD	P	Sample 2	M	SD	P	Sample 3	M	SD	P			
Q1-Q6	f_0	7.32	1.59	0.381	f_0	7.25	1.60	0.467	f_0	7.34	1.21	0.241		
	f_1	6.91	1.95			f_1	6.90			2.07	f_1		7.41	1.35
	f_0	7.32	1.59	0.023	Q1-Q6	f_0	7.25	1.60	0.034	Q1-Q6	f_0	7.34	1.21	0.018
	f_2	6.16	2.19			f_2	6.20	2.11			f_2	6.31	1.99	
	f_0	7.32	1.59	0.000	f_0	7.25	1.60	0.036	f_0	7.34	1.21	0.049		
	f_3	7.88	1.69			f_3	8.09			1.42	f_3		7.82	1.90
Q7	f_0	0.40	0.86	0.000	f_0	0.47	1.01	0.000	f_0	0.27	0.64	0.000		
	f_1	2.87	1.55			f_1	3.20			1.73	f_1		2.63	1.22
	f_0	0.40	0.86	0.000	Q7	f_0	0.47	1.01	0.000	Q7	f_0	0.27	0.64	0.000
	f_2	5.10	2.50			f_2	5.70	2.23			f_2	4.97	1.97	
	f_0	0.40	0.86	0.000	f_0	0.47	1.01	0.000	f_0	0.27	0.64	0.000		
	f_3	5.30	2.04			f_3	6.30			2.39	f_3		6.20	2.04

TABLE 10: Analysis of female sleeping scale differences between f_0 and after stimulated in phases of f_1 , f_2 , and f_3 by t -test for sample 1, sample 2, and sample 3.

Sample 1	M	SD	P	Sample 2	M	SD	P	Sample 3	M	SD	P		
Q1-Q6	f_0	7.69	1.17	0.575	f_0	7.73	1.41	0.436	f_0	7.63	1.01	0.648	
	f_1	7.42	1.39		f_1	7.23	2.00		f_1	7.43	1.34		
	f_2	7.09	1.77		f_2	6.58	1.89		f_2	6.91	1.26		
	Q1-Q6	f_0	7.69	1.17	0.284	f_0	7.73	1.41	0.068	f_0	7.63	1.01	0.094
		f_1	7.69	1.17		f_1	7.73	1.41		f_1	7.63	1.01	
		f_3	8.32	1.28		f_3	8.18	1.49		f_3	8.09	1.43	
Q7	f_0	0.53	1.06	0.000	f_0	0.60	1.30	0.000	f_0	0.27	0.80	0.000	
	f_1	3.33	1.80		f_1	3.87	2.00		f_1	3.07	1.33		
	f_2	5.67	2.32		f_2	6.87	1.92		f_2	5.60	2.16		
	Q7	f_0	0.53	1.06	0.000	f_0	0.60	1.30	0.000	f_0	0.27	0.80	0.000
		f_1	0.53	1.06		f_1	0.60	1.30		f_1	0.27	0.80	
		f_3	5.87	2.00		f_3	7.47	2.00		f_3	7.13	2.03	

increasing. This result demonstrated that the biofeedback fabrics in conditions of different flashing frequencies are all effective for female. As to male, the result was the same with female. The biofeedback fabrics in conditions of 3 kinds of flashing frequencies are all effective to male. Comparing female with male, the effect in enhancing sleeping sense for female is more significant than it for male because the changes of Alpha wave decreasing and Theta/Delta wave increasing for female are more significant than it for male; that is, the female's brain wave is easier to be changed than it for male's brain wave.

(3) *Analysis of Brain Wave for Age 1, Age 2, and Age 3 at Different Stimulated Stage.* The analyses of brain waves strength for groups of Age 1, Age 2, and Age 3 at different flashing frequencies were listed in Tables 6, 7, and 8. For the Age 1 (18 to 29) group, the Alpha waves were decreased and the Theta/Delta waves were increased, but all of them were not significant. For the Age 2 (30 to 49) group, the Alpha waves were decreased, however they were not significant, but the Theta and Delta waves were significantly increased. For the Age 3 (50 to 65) group, the Alpha waves were decreased and the Theta waves were increased; however they were not significant, but the Delta waves were increased and reached a significant level. According to the aforementioned results, the effect in enhancing sleeping sense for Age 2 group is the best among all the groups of Age, and Age 1 group ranks behind Age 3 group. Maybe the stress of the Age 2 group is the strongest among all the groups of Age and the stress of the Age 3 group is stronger than Age 1 group. Therefore, we can infer from the results that the stronger the participant's stress is, the more obvious the effect in enhancing sleeping sense is.

(4) *Analysis of Sleeping Scale at Different Stimulated Stages for Different Samples.* The sleeping scale was applied to investigate the enhancement effect of sleeping sense for the participants at different flashing frequencies for 3 samples. The evaluating data, that is, the sleeping scale score, obtained were further analyzed based on different sample stimulation,

participant's age, and gender. The results were elaborated as below. The score differences of sleeping scale between f_0 after the resumed stage (RS) and after the stimulated stage (SS) in phases of f_1 , f_2 , and f_3 for sample 1, sample 2, and sample 3 were analyzed according to the t -test. The results were listed in Table 9. For all the samples in phases of f_1 , f_2 , and f_3 , the differences of Q7 standing for sleeping sense between (f_0) after RS and (f_1 , f_2 , f_3) after SS were extremely significantly increased. Their P values were all reaching 0.000. The differences of Q1-Q6 standing for relaxed feel for f_3 (10 Hz) were increased significantly. Their P values were less than 0.05. Adversely, the differences of Q1-Q6 for f_2 (5 Hz) were decreased significantly. Besides, the difference was not significant while comparing f_0 with f_1 (0 Hz). The results demonstrated that the sleeping sense of the participants can be enhanced when their visual system were stimulated by all samples in frequencies of f_1 , f_2 , and f_3 . However, the relaxed feel of the participants can be enhanced while stimulating only in frequency of f_3 for all samples.

(5) *Analysis of Sleeping Scale for Male And Female at Different Stimulated Stages for Different Samples.* The score differences of sleeping scale for male and female between f_0 after the resumed stage (RS) and after the stimulated stage (SS) in phases of f_1 , f_2 , and f_3 for sample 1, sample 2, and sample 3 were analyzed and the results were listed in Tables 10 and 11. For all the samples in phases of f_1 , f_2 , and f_3 , the differences for male and female of Q7 standing for sleeping sense between f_0 (after RS) and f_1 , f_2 , and f_3 (after SS) were extremely significantly increased. Their P values were all reaching 0.000. Adversely, the differences of Q1-Q6 for male and female were not significant while comparing f_0 with f_1 , f_2 , and f_3 . The results demonstrated that the sleeping sense of the participants for male and female can be enhanced extremely significantly when their visual system were stimulated for all samples in the frequencies of f_1 , f_2 , and f_3 . However, the relaxed feel of the participants cannot be enhanced significantly while stimulating in the frequencies of f_1 , f_2 , and f_3 for all samples. Besides, the higher the flashing

TABLE 11: Analysis of male sleeping scale differences between f_0 and after stimulated in phases of f_1 , f_2 , and f_3 by t -test for sample 1, sample 2, and sample 3.

Sample 1	M	SD	P	Sample 2	M	SD	P	Sample 3	M	SD	P	
Q1-Q6	f_0	6.94	1.88	0.487	f_0	6.77	1.68	0.779	f_0	7.06	1.35	0.514
	f_1	6.40	2.32		f_1	6.57	2.16		f_1	7.39	1.42	
	f_0	6.94	1.88	0.081	f_0	6.77	1.68	0.211	f_0	7.06	1.35	0.068
	f_2	5.43	2.22		f_2	5.82	2.31		f_2	5.79	2.42	
	f_0	6.94	1.88	0.482	f_0	6.77	1.68	0.138	f_0	7.06	1.35	0.472
	f_3	7.44	1.96		f_3	7.80	1.90		f_3	7.56	2.29	
Q7	f_0	0.27	0.59	0.000	f_0	0.33	0.62	0.000	f_0	0.27	0.46	0.000
	f_1	2.40	1.12		f_1	2.53	1.13		f_1	2.20	0.94	
	f_0	0.27	0.59	0.000	f_0	0.33	0.62	0.000	f_0	0.27	0.46	0.000
	f_2	4.53	2.61		f_2	4.53	1.92		f_2	4.33	1.59	
	f_0	0.27	0.59	0.000	f_0	0.33	0.62	0.000	f_0	0.27	0.46	0.000
	f_3	4.73	1.98		f_3	5.13	2.23		f_3	5.27	1.62	

TABLE 12: Analysis of sleeping scale differences between f_0 and after SS for sample 1 in phases of f_1 , f_2 , and f_3 by t -test for groups of Age 1, Age 2, and Age 3.

Age 1	M	SD	P	Age 2	M	SD	P	Age 3	M	SD	P	
Q1-Q6	f_0	7.51	1.12	0.628	f_0	6.89	1.28	0.678	f_0	7.51	1.84	0.490
	f_1	7.35	1.42		f_1	6.72	1.77		f_1	7.15	2.17	
	f_0	7.51	1.12	0.009	f_0	6.89	1.28	0.011	f_0	7.51	1.84	0.052
	f_2	6.60	1.46		f_2	5.62	2.29		f_2	6.45	2.29	
	f_0	7.51	1.12	0.299	f_0	6.89	1.28	0.136	f_0	7.51	1.84	0.045
	f_3	7.81	1.10		f_3	7.58	2.14		f_3	8.41	1.53	
Q7	f_0	0.30	0.47	0.000	f_0	0.70	1.29	0.000	f_0	0.13	0.35	0.000
	f_1	2.27	1.14		f_1	3.97	1.71		f_1	2.47	1.01	
	f_0	0.30	0.47	0.000	f_0	0.70	1.29	0.000	f_0	0.13	0.35	0.000
	f_2	5.03	1.97		f_2	6.07	2.56		f_2	4.67	1.97	
	f_0	0.30	0.47	0.000	f_0	0.70	1.29	0.000	f_0	0.13	0.35	0.000
	f_3	5.40	1.40		f_3	6.83	2.60		f_3	5.57	2.16	

frequency, the better the effect in enhancing sleeping sense for both genders of participants. The enhancement effect in sleeping sense for female is better than it for male.

(6) *Analysis of Sleeping Scale for Age Groups at Different Stimulated Stages.* The score differences of sleeping scale between f_0 (after RS) and f_1 , f_2 , and f_3 (after SS) for 3 groups of Age 1, Age 2, and Age 3 were analyzed and their results were listed in Table 12. For the sample 1 in phases of f_1 , f_2 , and f_3 , the differences of Q7 standing for sleeping sense between f_0 (after RS) and f_1 , f_2 , and f_3 (after SS) were extremely significantly increased. Their P values were all reaching 0.000. Adversely, the differences for all Age groups of Q1-Q6 were no significant differences while comparing f_0 with f_1 , f_2 , and f_3 . The results demonstrated that the sleeping sense of the participants for all Age groups can be enhanced extremely when their visual system were stimulated by sample 1 in frequencies of f_1 , f_2 , and f_3 . However, the relaxed feel of the participants of all Age groups cannot be enhanced significantly while stimulating in frequencies of f_1 , f_2 , and f_3 for sample 1. Besides, the higher the flashing frequency, the better the enhancing sleeping sense for 3 Age groups of

participants. The effect of enhancing sleeping sense for Age 2 group (30~49) is the best among 3 Age groups. Maybe the stress of Age 2 group is the strongest among all the groups of Age. Therefore, we can infer from the results that the stronger the participant's stress is, the more obvious the effect in enhancing sleeping sense is, and it is same with the results of above Table 6 to Table 8.

4. Conclusion

We designed a unique biofeedback fabric including background layer and pattern layer, 3 kinds of wavelengths of sine waves, and 3 kinds of flashing frequencies based on the biofeedback principle for enhancing sleeping sense and evaluated its performance according to the brain wave measured with EEG and the sleeping scale was developed by ourselves. The results can be summarized as follows.

- (1) For all the phases of f_1 , f_2 , and f_3 , Alpha waves (B_1) are decreased significantly and transferred into Theta wave (B_3) and Delta wave (B_4); that is, the biofeedback fabrics in conditions of 3 kinds of flashing frequencies

for all samples are all effective in enhancing sleeping sense.

- (2) The effect in enhancing sleeping sense for female is more significant than it for male.
- (3) The effect in enhancing sleeping sense for Age 2 group (30–49) is the best among all Age groups.
- (4) The stronger the participant's stress is, the more obvious the effect in enhancing sleeping sense is.

Conflict of Interests

The authors declare that there is no conflict of interests regarding the publication of this paper.

Acknowledgments

The authors would like to take this opportunity to thank to Industrial Development Bureau, Ministry of Economic Affairs (MOEA) for the financial support. They also would like to thank the authority of Shu-Te University for providing them with a good environment and facilities to complete this project. Finally, they would like to express their heartfelt thanks to all of the participants for their help in this study.

References

- [1] L. Engel and L. B. Andersen, "Effects of body-mind training and relaxation stretching on persons with chronic toxic encephalopathy," *Patient Education and Counseling*, vol. 39, no. 2-3, pp. 155–161, 2000.
- [2] G. D. Solomon, "Slow wave photic stimulation in the treatment of headache—a preliminary report," *Headache*, vol. 25, no. 8, pp. 444–446, 1985.
- [3] T. Mulholland, "Human EEG, behavioral stillness and biofeedback," *International Journal of Psychophysiology*, vol. 19, no. 3, pp. 263–279, 1995.
- [4] S. H. Spence, L. Sharpe, T. Newton-John, and D. Champion, "Effect of EMG biofeedback compared to applied relaxation training with chronic, upper extremity cumulative trauma disorders," *Pain*, vol. 63, no. 2, pp. 199–206, 1995.
- [5] P. Williams and M. West, "EEG responses to photic stimulation in persons experienced at meditation," *Electroencephalography and Clinical Neurophysiology*, vol. 39, no. 5, pp. 519–522, 1975.
- [6] J. S. Bell, "The use of EEG theta biofeedback in the treatment of a patient with sleep-onset insomnia," *Biofeedback and Self-Regulation*, vol. 4, no. 3, pp. 229–236, 1979.
- [7] C. H. Bastien, M. LeBlanc, J. Carrier, and C. M. Morin, "Sleep EEG power spectra, insomnia, and chronic use of benzodiazepines," *Sleep*, vol. 26, no. 3, pp. 313–317, 2003.

Research Article

Effects of Deep Cryogenic Treatment on Wear Mechanisms and Microthermal Expansion for the Material of Drive Elements

Yuh-Ping Chang,¹ Gino Wang,¹ Jeng-Haur Horng,² Li-Ming Chu,³ and Yih-Chyun Hwang⁴

¹ Department of Mechanical Engineering, Kun Shan University, Tainan 710, Taiwan

² Department of Power Mechanical Engineering, National Formosa University, Yunlin 632, Taiwan

³ Department of Mechanical and Automation Engineering, I-Shou University, Kaohsiung 840, Taiwan

⁴ Hiwin Technologies Corp., Taichung 40707, Taiwan

Correspondence should be addressed to Yuh-Ping Chang; ypc0318@mail.ksu.edu.tw

Received 15 September 2013; Accepted 2 November 2013

Academic Editor: Shoou-Jinn Chang

Copyright © 2013 Yuh-Ping Chang et al. This is an open access article distributed under the Creative Commons Attribution License, which permits unrestricted use, distribution, and reproduction in any medium, provided the original work is properly cited.

By the composite heat treatments, the strength and the surface hardness of the materials of drive elements can be improved. Moreover, the high accurate and capable machines can be obtained. For the numerous composite heat treatments, the deep cryogenic treatment has been used widely for the purpose of low thermal expansion in the industry. Therefore, this paper is further to investigate the low friction, wear resistance, and low thermal expansion for the carburizing steels of drive elements with deep cryogenic treatment. According to the experimental results, martensitic transformation occurred after the deep cryogenic treatment. The effects of deep cryogenic treatment on wear mechanisms are significant. The shape of wear particles changes from slip tongue to smooth stratification. Moreover, the surface magnetization is smaller for the case of Carburizing-Deep cryogenic treatment. Hence, the wear mechanism becomes simple. Besides, the thermal expansion is significantly smaller for the case of Carburizing-Deep cryogenic treatment.

1. Introduction

Three attractable problems have been respected over the past decades, such as the fast development of high accurate mechanical engineering, marketability, and energy crisis. Hence, the performance of high reliance and high environmental consciousness is very important for the developments of the tool machines. In order to achieve the above goal, the technology of composite heat treatment is the most important method to improve the surface properties [1, 2]. By the composite heat treatments, the strength and the surface hardness of the materials of drive elements can be improved. Therefore, both of low friction and wear resistance can be further completed [3, 4].

Many papers about the heat treatment technology had been proposed. Especially, the deep cryogenic treatment has been used widely for the purpose of wear resistance in the industry [5, 6]. Generally speaking, the drive elements by the deep cryogenic treatment are a wise method for improving

the performance of low friction, wear resistance, and low thermal expansion. This can be reasonably explained by that the austenite is one of the unfavorable factors for the microtechnique, such as measuring tool, bearing, and precision optical machinery. Hence, the deep cryogenic treatment [7] and the super cryogenic treatment [8] are always used to make martensitic transformation and improve the wear resistance and the low thermal expansion of the drive elements.

Moreover, since the authors had experimentally studied the wear mechanisms of the pair of iron with the carbon steels in-depth [9–12], the knowledge is applied and adapted to the study of using continuous variation of surface magnetization and friction coefficient for monitoring the tribological properties of the low carbon alloy steel in this paper. Therefore, the effects of the deep cryogenic treatment on wear resistance, and microthermal expansion of the drive elements are investigated in this study. According to the experimental results, the low friction, wear resistance, and low surface magnetization for the drive elements with

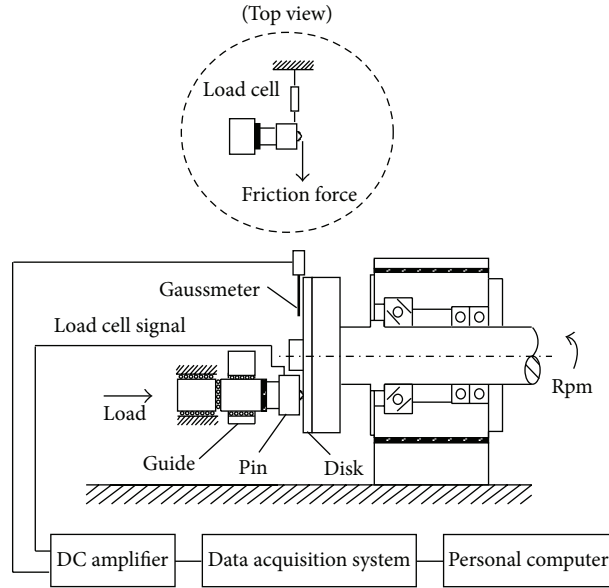


FIGURE 1: Schematic diagram of ball/disk friction tester with the measuring systems.

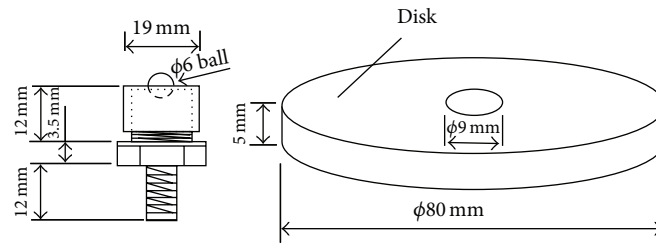


FIGURE 2: The size and shape of the specimen.

the deep cryogenic treatment can be clarified. Moreover, the microwear mechanisms can be investigated by the SEM of the wear particles. Besides, the decreasing of the microthermal expansion will be completed to further develop the tool machines.

2. Experimental Apparatus and Procedures

2.1. Experimental Apparatus. The experiments were conducted on a ball/disk friction tester with a measuring system as shown in Figure 1 to investigate the effects of the deep cryogenic treatment on wear resistance of the drive elements under dry severe wear condition. The disk surface was set vertical to the ground to simplify the wear mechanisms. The stationary ball specimen was placed on a rest, connected to a load cell and supported by a set of roller bearings. A load, vertical to the disk surface, was applied to the ball specimen by using the level rule. To avoid impact and to maintain constant contact between the specimens during the friction process, a soft spring ($k = 0.17 \text{ N/mm}$) with an oil damper ($c = 1.04 \text{ Ns/m}$) was installed in the loading system. This setup enabled accurate measurement of the friction coefficient between the ball and disk specimens.

In Figure 1, the generated tribomagnetization on the disk surface during the rotating friction process was in the order of 0.1 G. The response time of the measuring system was less than 10 ms. Briefly, the instantaneous friction coefficient between the contacting specimens was determined by the voltage signal from the load cell. The variations of surface magnetization were measured by a gauss meter. As the gauss meter probe was situated opposite to the pin specimen, the signal of the tribomagnetization therefore lagged the friction voltage signal by half a cycle. The above two voltages from the load cell and the gauss meter were simultaneously recorded by a data acquisition system and fed to a personal computer for data analysis.

2.2. Test Specimens. The ball specimens were made of SUJ2. Besides, the disk specimens were made of SCM415. Moreover, the disk specimens had been conducted with the different composite heat treatments before the friction tests. The specimens are shown in Figure 2 and their material properties are given in Table 1. Moreover, the surface hardness of the disk specimens with different composite heat treatments is shown in Table 2.

TABLE I: Compositions of SCM415.

SCM415 wt%								
C	Si	Mn	P	S	Cr	Cu	Mo	Ni
0.13~0.18	0.15~0.35	0.6~0.85	≤ 0.03	≤ 0.03	0.9~1.2	≤ 0.3	0.15~0.25	≤ 0.25

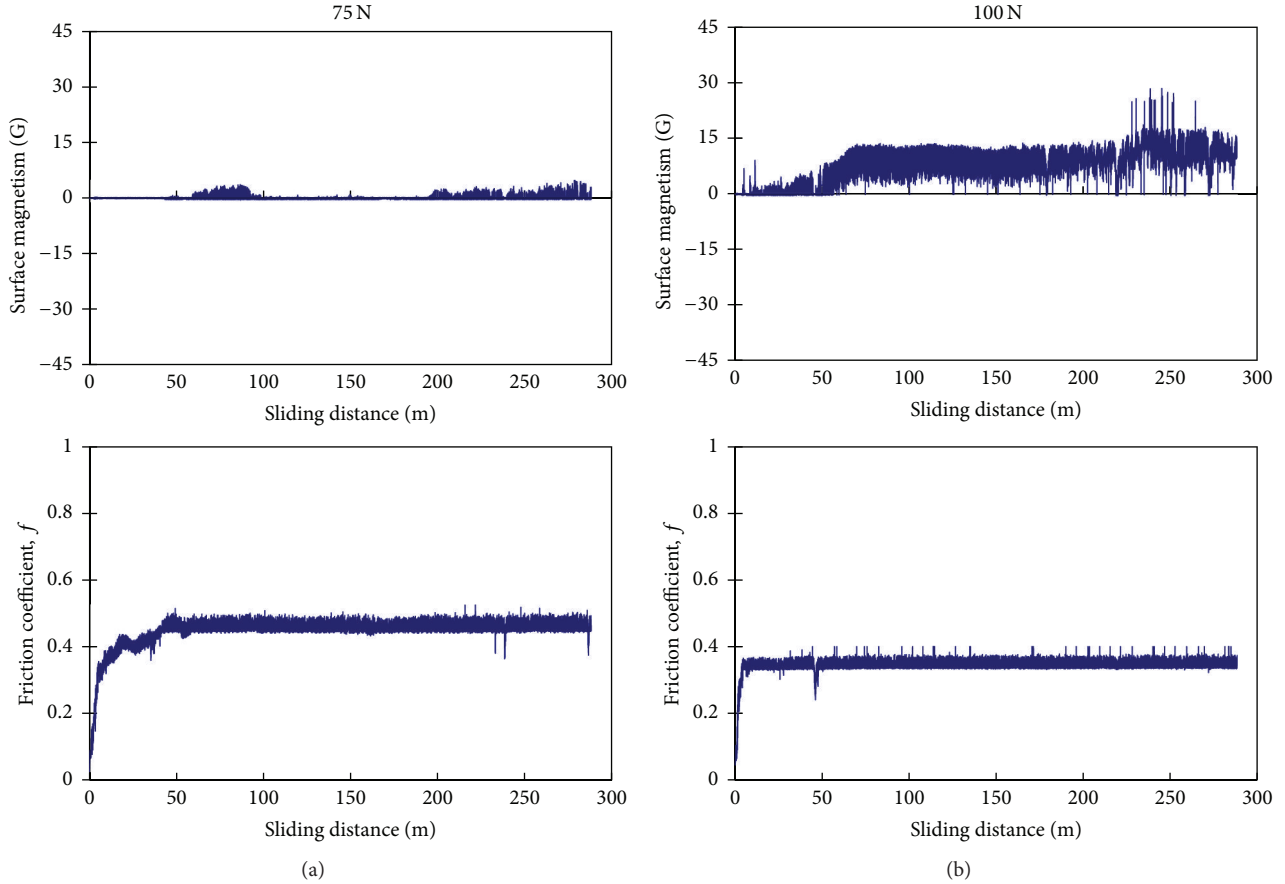


FIGURE 3: Surface magnetization and friction coefficient responses for SCM415 with Carburizing-Tempering: (a) 75 N and (b) 100 N.

TABLE 2: Surface hardness of SCM415 with different composite heat treatments.

Composite heat treatments	Surface hardness (HRC)
Carburizing-Tempering	65.7
Carburizing-Deep cryogenic treatment-Tempering	68.4

2.3. Experimental Procedures. Prior to each friction test the specimens were cleaned with acetone in an ultrasonic cleaner and securely locked in position in the tester. The location and tightness between the ball and the disk interface were of paramount importance to ensure experimental accuracy. As the disk rotated clockwise at a set speed, a normal load was applied to the interface of the specimens.

According to the results [9–12], the wear mechanisms of the pair of iron with the carbon steels transfer during the normal loads from 75 N to 100 N. Therefore, the sliding

speed was fixed at 267 mm/s and the normal loads were set as 75 N and 100 N in this study. The dynamic variations of friction coefficient and surface magnetization were measured simultaneously during each test. After each test, the wear particles were examined under a SEM. The depth of wear track is measured by means of a surface tester. As the output electric potential from the gauss meter during the rotating friction process was in the order of mV, a DC isolated amplifier was used at a low gain of 25. The microthermal expansions of the drive elements were measured by a high precision displacement tester. All tests were carried out under dry friction condition. The average room temperature for the test was $23 \pm 2^\circ\text{C}$, and the average relative humidity was $65 \pm 5\%$.

3. Results and Discussions

Figure 3 shows the typical variations of surface magnetization and friction coefficient with sliding distance produced by

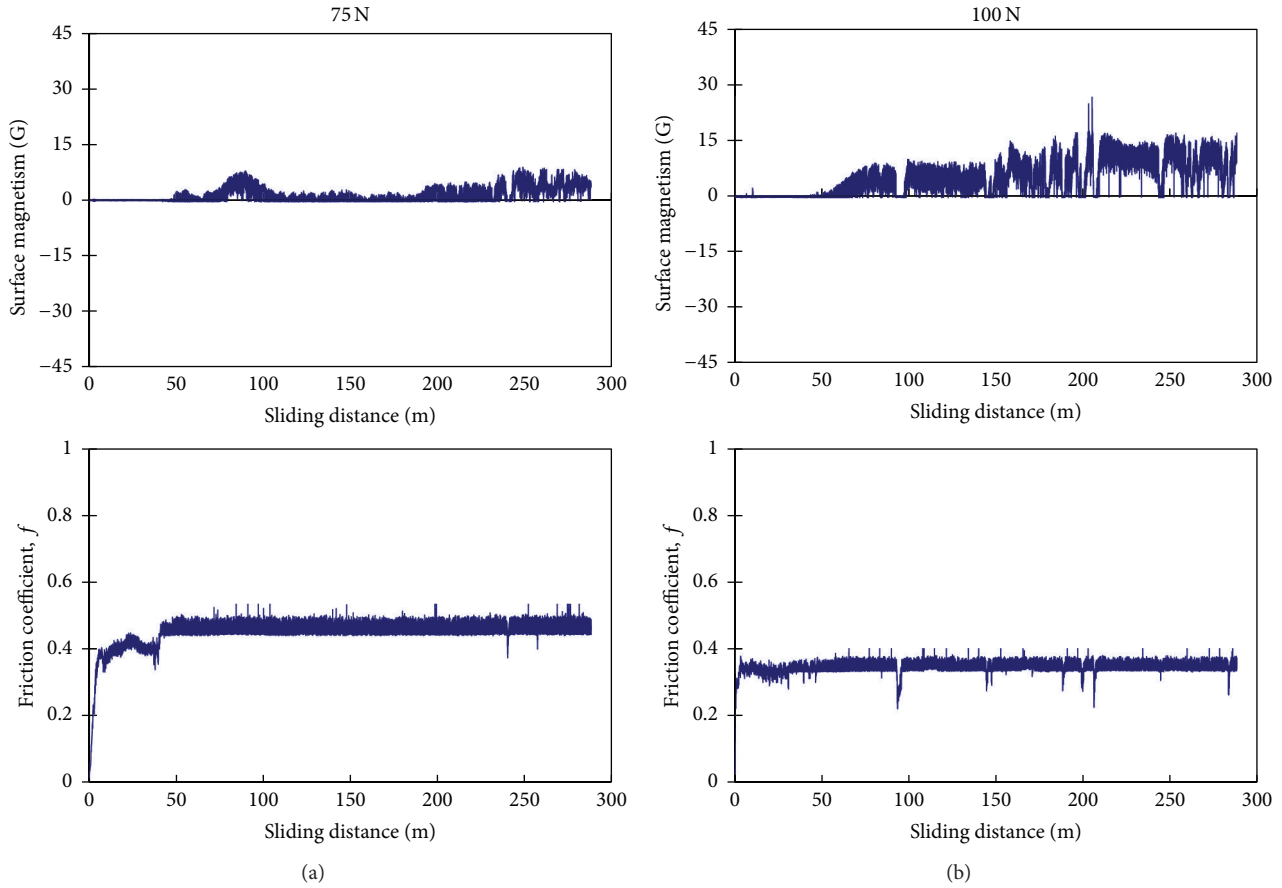


FIGURE 4: Surface magnetization and friction coefficient responses for SCM415 with Carburizing-Deep cryogenic treatment-Tempering: (a) 75 N and (b) 100 N.

the SUJ2 ball sliding on the SCM415 with Carburizing-Tempering. It is seen from this figure that the average friction coefficient is 0.44 and the maximum surface magnetization is about 4.77 G at 75 N. Moreover, the average friction coefficient is 0.34 and the maximum surface magnetization surges to approximately 28.42 G at 100 N.

The typical variations of surface magnetization and friction coefficient with sliding distance produced by the SUJ2 ball sliding on the SCM415 with Carburizing-Deep cryogenic treatment-Tempering are shown in Figure 4. The average friction coefficient is 0.44 and the maximum surface magnetization is about 8.83 G at 75 N. Moreover, the average friction coefficient is 0.34 and the maximum surface magnetization surges to approximately 26.64 G at 100 N.

Therefore, the effects of deep cryogenic treatment on friction coefficient and surface magnetization are insignificant.

Figure 5 shows the SEM micrographs of wear particle for SCM415 with Carburizing-Tempering. It is seen from this figure that the wear particles show the shape of slip tongue. This indicates that the wear mechanism is ploughing. The size of the larger wear particles reaches 100 μm order.

Representative SEM micrographs of wear particle for SCM415 with Carburizing-Deep cryogenic treatment-Tempering are shown in Figure 6. The wear particles are countless and highly concentrated. The size of the larger wear particles

reaches 100 μm order. Moreover, the larger wear surfaces show smooth and stratiform structures. This also indicates that the material had been hard and brittle after deep cryogenic treatment.

Therefore, the effects of deep cryogenic treatment on wear mechanisms are significant. The shape of wear particles changes from slip tongue to stratification.

Figure 7 shows the wear profile for the SCM415 disks. It is seen from this figure that the depth of the wear track is only 5 μm for SCM415 with Carburizing-Tempering. Moreover, the phenomenon of material transfer can be found. However, the depth of the wear track can reach to 5.5 ~ 9.5 μm for SCM415 with Carburizing-Deep cryogenic treatment-Tempering. This can be reasonable explained by that the martensitic transformation occurred after the deep cryogenic treatment.

Dynamic responses of microthermal expansion for the specimen under different composite heat treatments are shown in Figure 8. According to the results, Figure 9 shows the microthermal expansion for the specimen under the different heating temperatures. It is seen from this figure that the microthermal expansions are similar and smaller for the source SCM415 and the SCM415 with Carburizing-Deep cryogenic treatment-Tempering. On the other hand, it shows larger than the other two cases for the SCM415

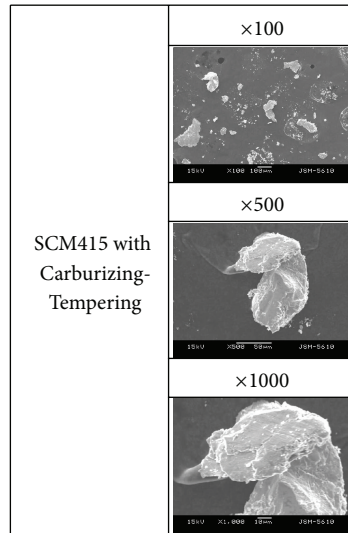


FIGURE 5: Representative SEM micrographs of wear particle for SCM415 with Carburizing-Tempering.

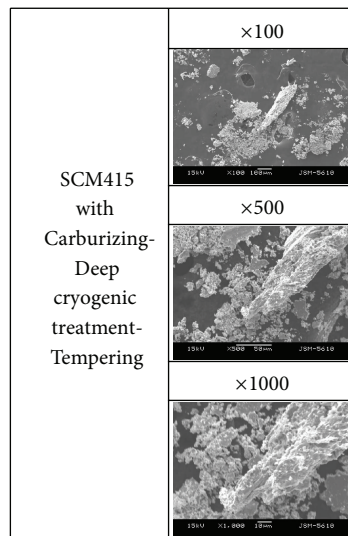


FIGURE 6: Representative SEM micrographs of wear particle for SCM415 with Carburizing-Deep cryogenic treatment-Tempering.

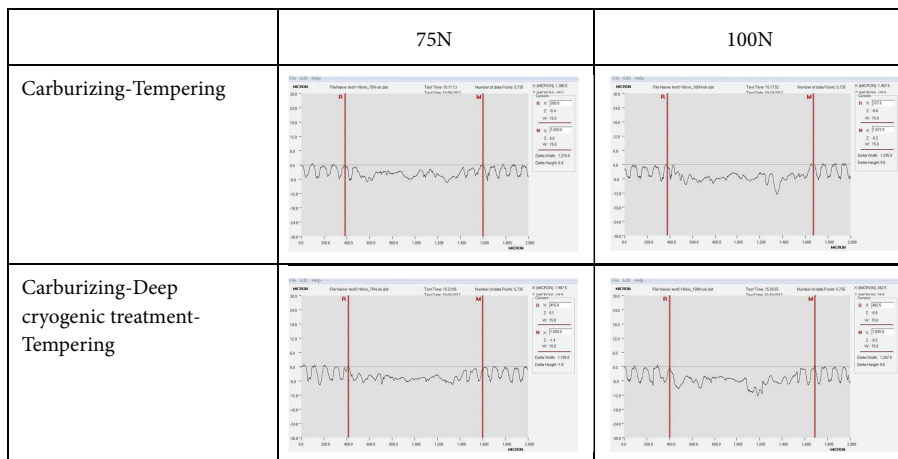


FIGURE 7: The wear profile for the SCM415 disks.

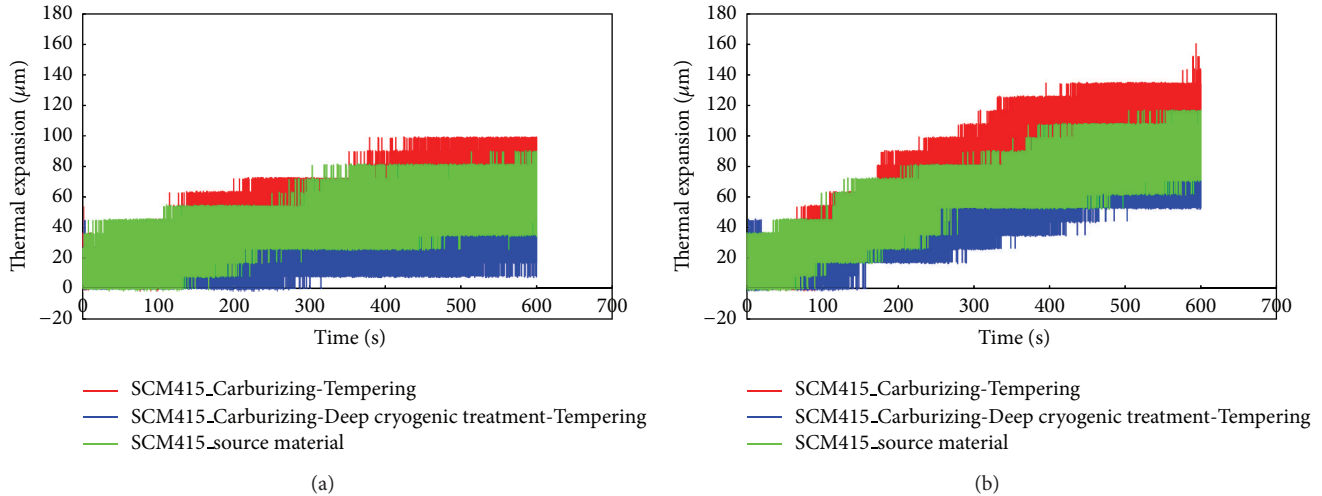


FIGURE 8: Dynamic responses of microthermal expansion for the specimen under different composite heat treatments: (a) the heating temperature of 100°C and (b) the heating temperature of 150°C.

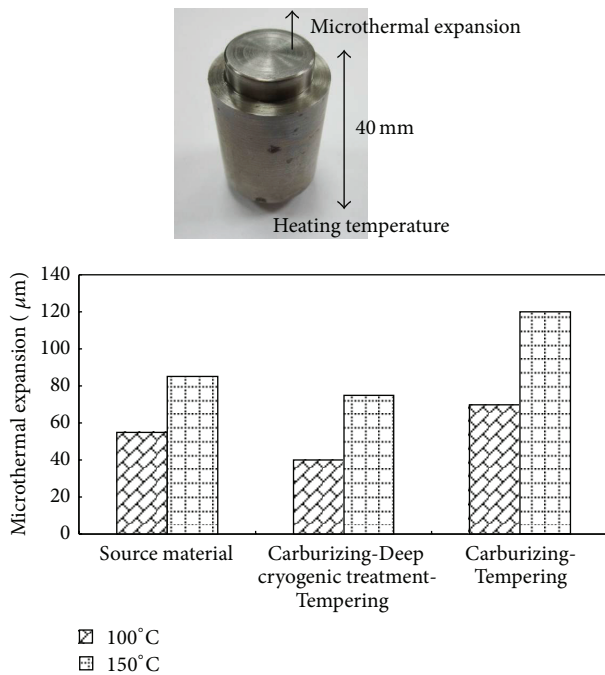


FIGURE 9: Microthermal expansion for the specimen under the different heating temperatures.

with Carburizing-Tempering. The differences between them are about 37~42%. Therefore, the effects of deep cryogenic treatment on microthermal expansion are significant. It can decrease about 40% microthermal expansion for the SCM415.

4. Conclusions

In this study, the effects of the deep cryogenic treatment on friction, wear mechanisms, and microthermal expansion of SCM415 have been investigated. From the experimental

results and the SEM observations of the wear particles, the following conclusions have been drawn.

- (1) The effects of deep cryogenic treatment on the values of friction coefficient and surface magnetization are insignificant.
- (2) The martensitic transformation occurred after the deep cryogenic treatment. The material had been hard and brittle. As a result, the depth of the wear track is larger and the phenomenon of material transfer is few.
- (3) Effects of deep cryogenic treatment on wear mechanisms are significant. The shape of wear particles changes from slip tongue to smooth stratification.
- (4) The effects of deep cryogenic treatment on microthermal expansion are obvious. It can decrease about 40% microthermal expansion under the heating temperature of 100°C.

Conflict of Interests

The authors declare that there is no conflict of interests regarding the publication of this paper.

Acknowledgment

The authors would like to express their appreciation to the National Science Council in Taiwan, for their financial support under Grant nos. NSC 101-2221-E-168-012 and NSC 102-2622-E-150-002-CC2.

References

- [1] M. F. Carlson, B. V. Narasimha Rao, and G. Thomas, "The effect of austenitizing temperature upon the microstructure and mechanical properties of experimental Fe/Cr/C steels," *Metallurgical Transactions A*, vol. 10, no. 9, pp. 1273–1284, 1979.

- [2] H.-F. Chai and C. Laird, "Mechanisms of cyclic softening and cyclic creep in low carbon steel," *Materials Science and Engineering*, vol. 93, pp. 159–174, 1987.
- [3] W. D. Callister, *Material Science and Engineering: An Introduction*, Wiley, New York, NY, USA, 3rd edition, 1994.
- [4] D.-H. Huang and G. Thomas, "Structure and mechanical properties of tempered martensite and lower bainite in Fe-Ni-Mn-C steels," *Metallurgical Transactions*, vol. 2, no. 6, pp. 1587–1598, 1971.
- [5] K. E. Thelning, *Steel and Its Heat Treatment*, Bofors Handbook, 1975.
- [6] A. M. Nasreldin, M. M. Ghoneim, F. H. Hammad, R. L. Klueh, and R. K. Nanstad, "Effect of tempering on the toughness of a Cr-Mo bainitic steel," *Journal of Materials Engineering and Performance*, vol. 2, no. 3, pp. 413–420, 1993.
- [7] T. P. Sweeney Jr., "Deep cryogenics: the great cold debate," *Heat Treating*, pp. 28–32, 1986.
- [8] D. N. Collins, "Deep cryogenic treatment of tool steels: a review," *Heat Treatment of Metals*, vol. 23, no. 2, pp. 40–42, 1996.
- [9] Y.-P. Chang, J.-P. Yur, H.-M. Chou, and H.-M. Chu, "Triboelectrification mechanisms for self-mated carbon steels in dry severe wear process," *Wear*, vol. 260, no. 11-12, pp. 1209–1216, 2006.
- [10] Y.-P. Chang, H.-M. Chu, and H.-M. Chou, "Effects of mechanical properties on the tribo-electrification mechanisms of iron rubbing with carbon steels," *Wear*, vol. 262, no. 1-2, pp. 112–120, 2007.
- [11] Y.-P. Chang, Y.-Y. Hung, L.-M. Chu, J.-P. Yur, and C.-H. Lin, "The surface magnetization approach on assessing tribological properties of steels with different TiN coatings," *Proceedings of the Institution of Mechanical Engineers J*, vol. 223, no. 4, pp. 715–722, 2009.
- [12] Y.-P. Chang, J.-H. Horng, J.-P. Yur, L.-M. Chu, and Y.-C. Hwang, "The surface magnetization approach on assessing the tribological properties of iron sliding against iron coated with pure tin and with a tin composite," *Proceedings of the Institution of Mechanical Engineers J*, vol. 225, no. 12, pp. 1199–1208, 2011.

Research Article

Effects of Nitride on the Tribological Properties of the Low Carbon Alloy Steel

Yuh-Ping Chang,¹ Jin-Chi Wang,¹ Jeng-Haur Horng,²
Li-Ming Chu,³ and Yih-Chyun Hwang⁴

¹ Department of Mechanical Engineering, Kun Shan University, Tainan 710, Taiwan

² Department of Power Mechanical Engineering, National Formosa University, Yunlin 632, Taiwan

³ Department of Mechanical and Automation Engineering, I-Shou University, Kaohsiung 840, Taiwan

⁴ Hiwin Technologies Corp., Taichung 40707, Taiwan

Correspondence should be addressed to Yuh-Ping Chang; ypc0318@mail.ksu.edu.tw

Received 15 September 2013; Accepted 2 November 2013

Academic Editor: Shoou-Jinn Chang

Copyright © 2013 Yuh-Ping Chang et al. This is an open access article distributed under the Creative Commons Attribution License, which permits unrestricted use, distribution, and reproduction in any medium, provided the original work is properly cited.

The technology of composite heat treatment is used popularly for low friction and wear resistance of drive elements. A large number of papers about the heat treatment technology had been proposed. Especially, the nitride treatment has been used widely for the purpose of wear resistance and low friction in the industry. Therefore, the self-developed vertical ball/disk friction tester with the measurement system was used to study the effects of nitride on the tribological properties of the low carbon alloy steel—SCM415—in this study. The experiments were conducted under dry and severe wear conditions. The variations of friction coefficient and surface magnetization were simultaneously recorded during dynamic friction process. After each test, the microstructures of the wear particles were observed and analyzed under a SEM, and the depth of wear track is measured by means of a surface tester. According to the experimental results, the wear resistance of the specimens with carburizing-nitride is significantly larger than the case of nitride-carburizing. Moreover, the surface magnetization was especially larger for the case of nitride-carburizing. As a result, the wear particles always stay in the interfaces and the wear mechanism becomes complex. Therefore, it is necessary to put nitride after carburizing for the composite heat treatments.

1. Introduction

The performance of high quality and high accuracy is very important for the high accurate mechanical engineering. Hence, the drive elements play an important role when it was used in the actuator of the machine. Moreover, the high performance of low friction and wear resistance for drive elements is very important for the actuator. In order to achieve the above goal, the technology of composite heat treatment is attracted recently for the industry [1, 2].

A large number of papers about the composite heat treatment technology had been proposed [3, 4]. Especially, the nitride treatment has been used widely for the purpose of wear-resistance and long fatigue life in the industry [5, 6]. The tool steels containing Al or Cr by the nitride treatment are considered as a wise method for improving the surface

hardness and the strength near the middle of the materials [7]. Therefore, the nitride treatment is always used to make surface hardening and improve wear resistance, fatigue life, and corrosion resistance for the tool steels [8, 9].

Since the authors had experimentally studied the tribological properties of the pair of iron with the carbon steels in depth [10–13], the knowledge is applied and adapted to the study of using continuous variation of friction coefficient for monitoring the tribological properties of the low carbon alloy steel in this paper. Therefore, the low friction and wear resistance for the carburizing steels of drive elements (such as SCM415) with nitride treatment are further investigated. Based on the results, the effects of different nitride treatments on the steels can be clarified. Besides, the purpose of better quality and faster product speed for the high accurate mechanical engineering can then be obtained.

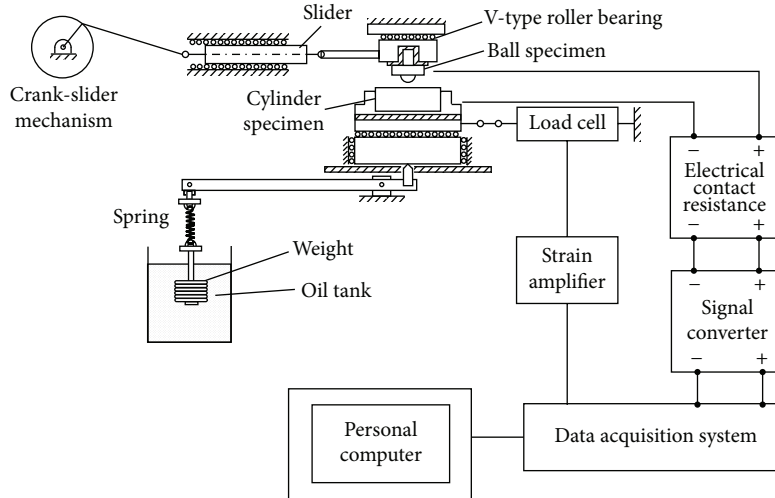


FIGURE 1: The reciprocating friction tester with the measuring systems.

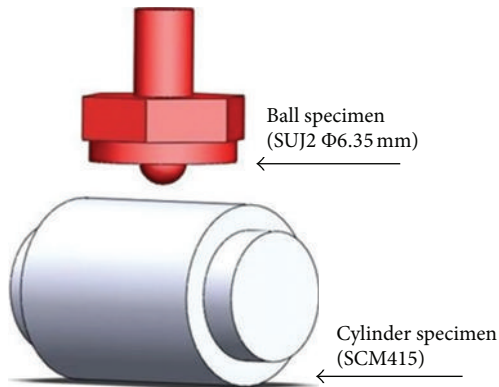


FIGURE 2: The size and shape of the ball and the cylinder.

TABLE 1: Compositions of SCM415.

SCM415 wt%				
C	Si	Mn	P	S
0.13~0.18	0.15~0.35	0.6~0.85	≤0.03	≤0.03
Cr	Cu	Mo	Ni	
0.9~1.2	≤0.3	0.15~0.25	≤0.25	

TABLE 2: Surface hardness of SCM415 with different composite heat treatments.

Composite heat treatments	Surface hardness (HRC)
Carburizing-tempering	66.1
Nitride-carburizing-tempering	65.8
Carburizing-nitride	42.8

2. Experimental Apparatus and Procedures

2.1. Experimental Apparatus. The experiments were conducted on a reciprocating friction tester with the measuring systems shown in Figure 1. A crank-slider mechanism was used in this reciprocating friction tester. The ball specimen was fixed to the carriage, which reciprocated along a V type roller bearing with an adjustable stroke via the length of the crank. In this study, the stroke of the crank-slider mechanism was set to 6 mm. The stationary cylinder specimen was placed on a rest, supported by the V type roller bearing. A load cell was attached to the rest for measuring the friction coefficient between the ball and cylinder specimens. Consequently, the friction coefficient between the pin and plate specimens can be measured easily. A normal load was applied to the ball specimen through the cylinder specimen and aligned using a level rule. Furthermore, in order to avoid the impact effect and to remain the complete contact between the specimens during the friction process, a softer spring ($k = 0.17 \text{ N/mm}$) with an oil damper ($c = 1.04 \text{ Ns/m}$) was installed as part of the loading system.

In Figure 1, the response time is less than 1 ms with the accuracy of 0.1% full scale. During the reciprocating friction process, the friction coefficient between the contacting specimens was derived from the voltage signal from the load cell and was recorded simultaneously by a data acquisition system. The signals were then fed to a personal computer for data analysis.

2.2. Test Specimens. In order to simulate the operating conditions of the drive elements (such as Ball Screws), the test specimens are arranged as ball/cylinder. The ball specimens were made of SUJ2. Besides, the cylinder specimens were made of SCM415. Moreover, the cylinder specimens had been conducted with the different composite heat treatments before the friction tests. The specimens are shown in Figure 2 and their material properties are given in Table 1. Moreover, the surface hardness of the cylinder specimens is shown in Table 2.

2.3. Experimental Procedures. Prior to each friction test the specimens were cleaned with acetone in an ultrasonic cleaner

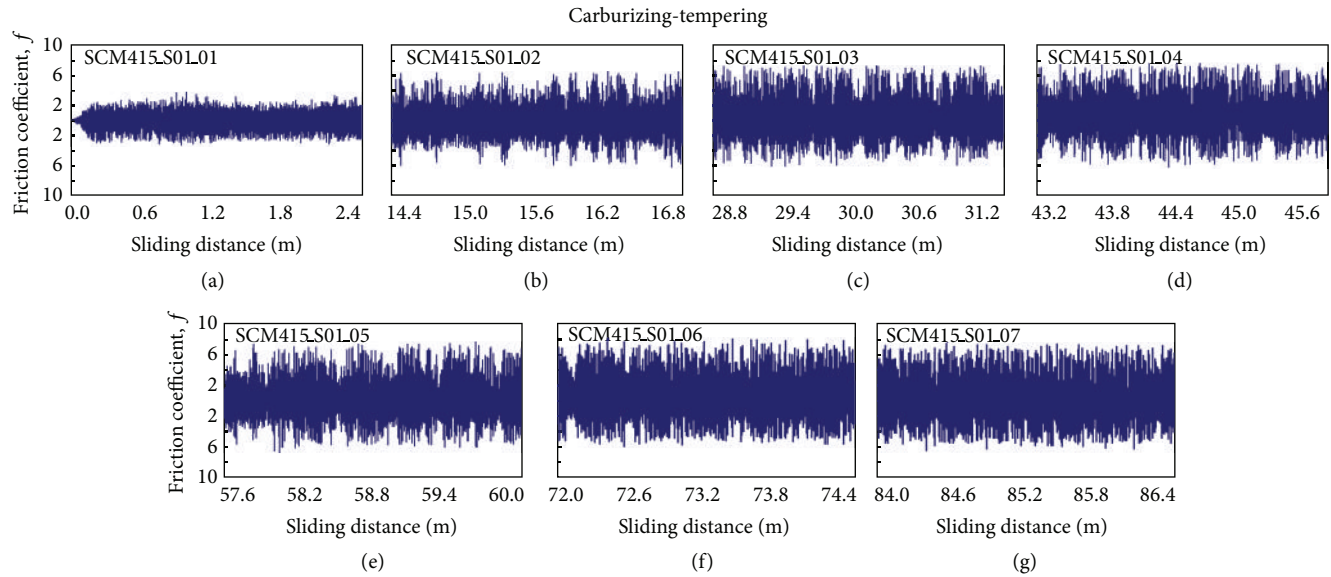


FIGURE 3: The typical variations of friction coefficient for SCM415 with carburizing-tempering.

before securely locked in position in the tester. The location and tightness between the ball and the cylinder interface were of paramount importance to ensure experimental accuracy. When the crank rotated clockwise at a set speed (cpm, cycles per minutes), the ball specimen reciprocated as a normal load was gradually applied to the interface of the specimens.

In this study, the reciprocating speed was fixed at 400 cpm (or the average speed of the ball specimen $V_a = 80$ mm/s) and the normal loads were set as 50 N. The dynamic variations of friction coefficient were measured during each test. After each test, the wear particles were examined under a SEM. The depth of wear track is measured by means of a surface tester. The response time of the measuring system was less than 1 ms and the accuracy was 0.1% full scale.

All tests were carried out under dry friction condition. The average room temperature for the test was $23 \pm 2^\circ\text{C}$, and the average relative humidity was $65 \pm 5\%$.

3. Results and Discussions

Figure 3 shows the typical variations of friction coefficient with sliding distance produced by the SUJ2 ball sliding on the SCM415 with carburizing-tempering. It is seen from this figure that the average friction coefficient is about 0.65 during the sliding distance of 0~2.4 m. It gradually increases after the sliding distance of 14.4 m. This indicates that the oxide film had been broken. Moreover, the friction coefficient significantly decreases after the sliding distance of 43.2 m. It can be reasonably explained by that the wear particles play the roller role.

The typical variations of friction coefficient with sliding distance produced by the SUJ2 ball sliding on the SCM415 with nitride-carburizing-tempering are shown in Figure 4. The average friction coefficient is about 0.65 during

the sliding distance of 0~2.4 m. It gradually increases after the sliding distance of 14.4 m. Moreover, the friction coefficient significantly increases after the sliding distance of 45 m. It can be reasonably explained by that the wear mechanism transfer to severe.

Figure 5 shows the typical variations of friction coefficient with sliding distance produced by the SUJ2 ball sliding on the SCM415 with carburizing-nitride. It is seen from this figure that the average friction coefficient is only 0.53 during the sliding distance of 0~2.4 m even when its surface hardness is the smallest. It gradually increases after the sliding distance of 14.4 m. Moreover, the friction coefficient significantly increases after the sliding distance of 45 m.

According to the above results, the friction coefficient of the specimen with carburizing-nitride is smaller than the other cases.

Representative metallograph and microstructures of surface for SCM415 with different composite heat treatments are shown in Figures 6–8. It is seen from Figure 6 that the film of the carburizing-tempering is about 0.09 mm. Figure 7 shows that the film of the nitride-carburizing is only about 0.006 mm. Moreover, the color is golden. On the other hand, the film of the carburizing-nitride is about 0.008 mm. The color is white as shown in Figure 8.

From the above results, the films of nitride-carburizing and carburizing-nitride are too thin to support the higher loads. Therefore, the wear resistance is not significant for them in this study.

Figure 9 shows the SEM micrographs of wear particle for SCM415 with carburizing-tempering. It is seen from this figure that 30~40% of the wear particles are larger than $5 \mu\text{m}$ order. The size of the larger wear particles reaches $100 \mu\text{m}$ order.

Figure 10 shows the SEM micrographs of wear particle for SCM415 with nitride-carburizing-tempering. The size of the

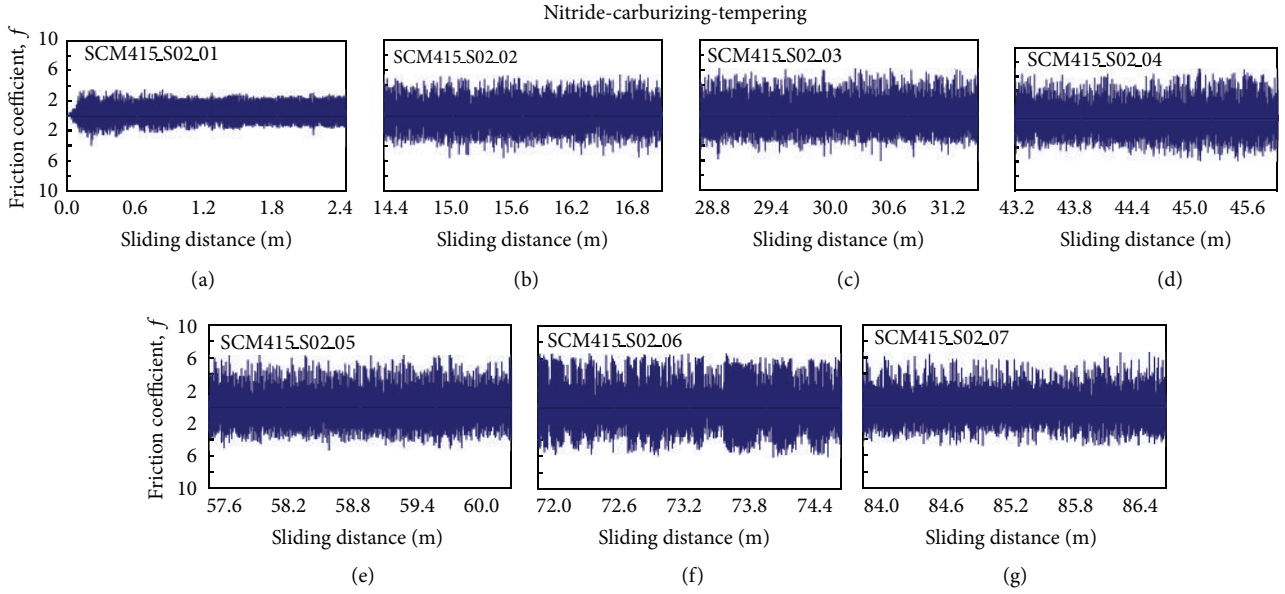


FIGURE 4: The typical variations of friction coefficient for SCM415 with nitride-carburizing-tempering.

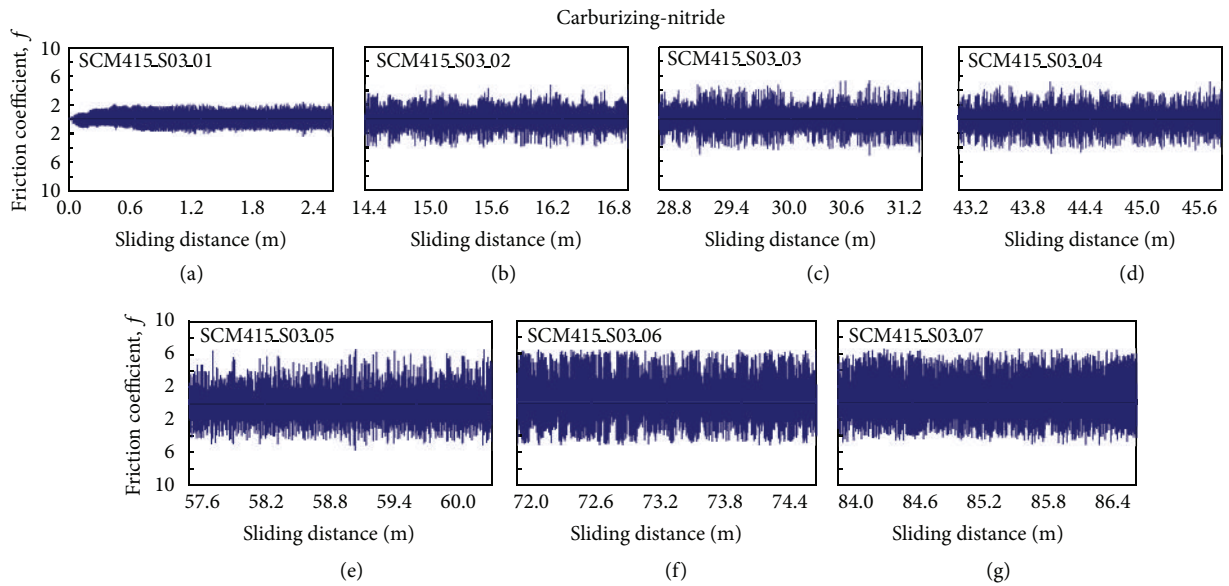


FIGURE 5: The typical variations of friction coefficient for SCM415 with carburizing-nitride.

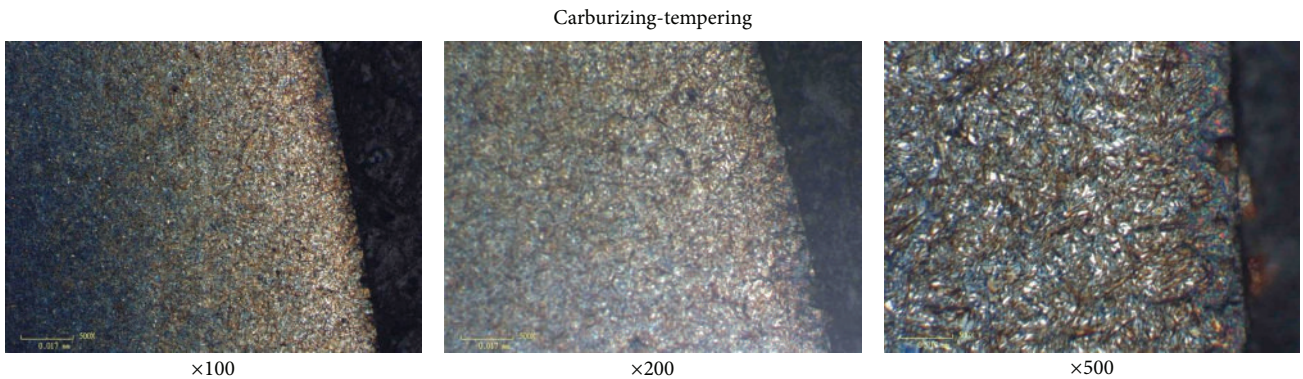


FIGURE 6: Representative metallograph and microstructures of surface for SCM415 with carburizing-tempering.

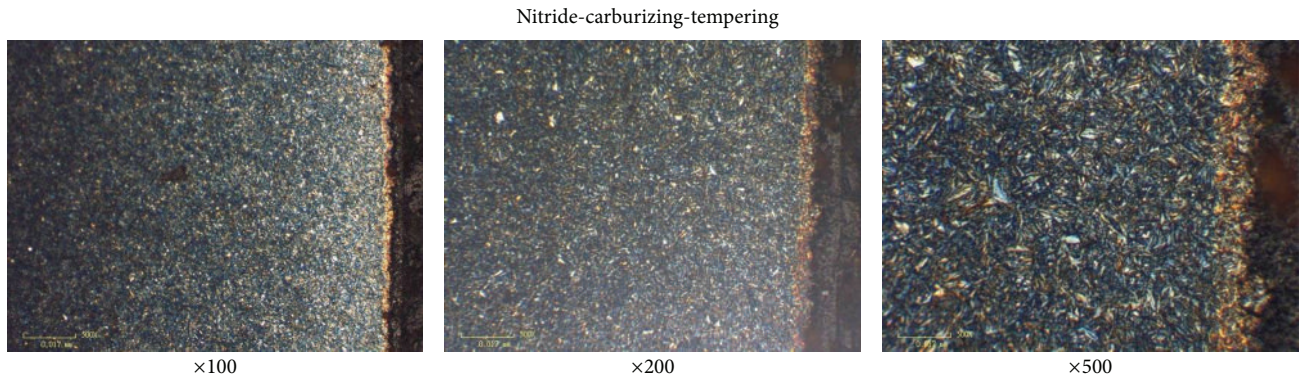


FIGURE 7: Representative metallograph and microstructures of surface for SCM415 with nitride-carburizing-tempering.

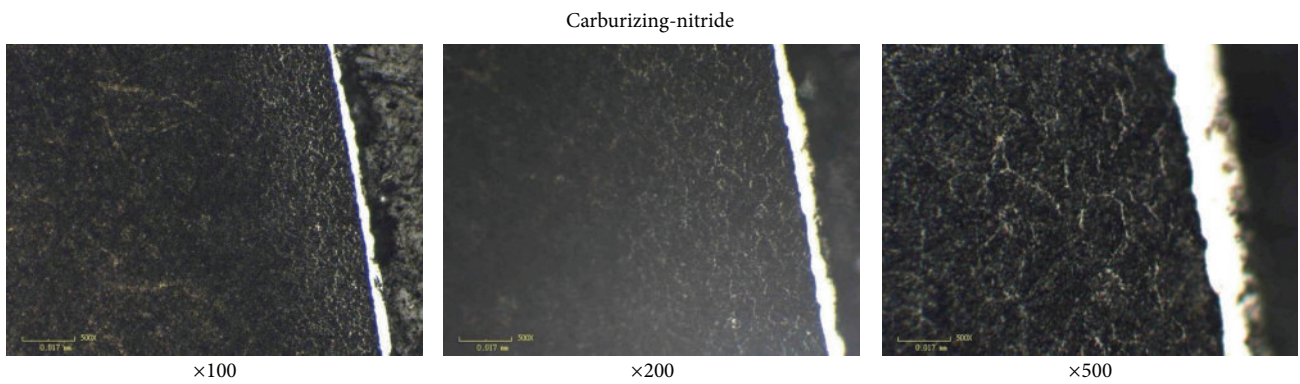


FIGURE 8: Representative metallograph and microstructures of surface for SCM415 with carburizing-nitride.

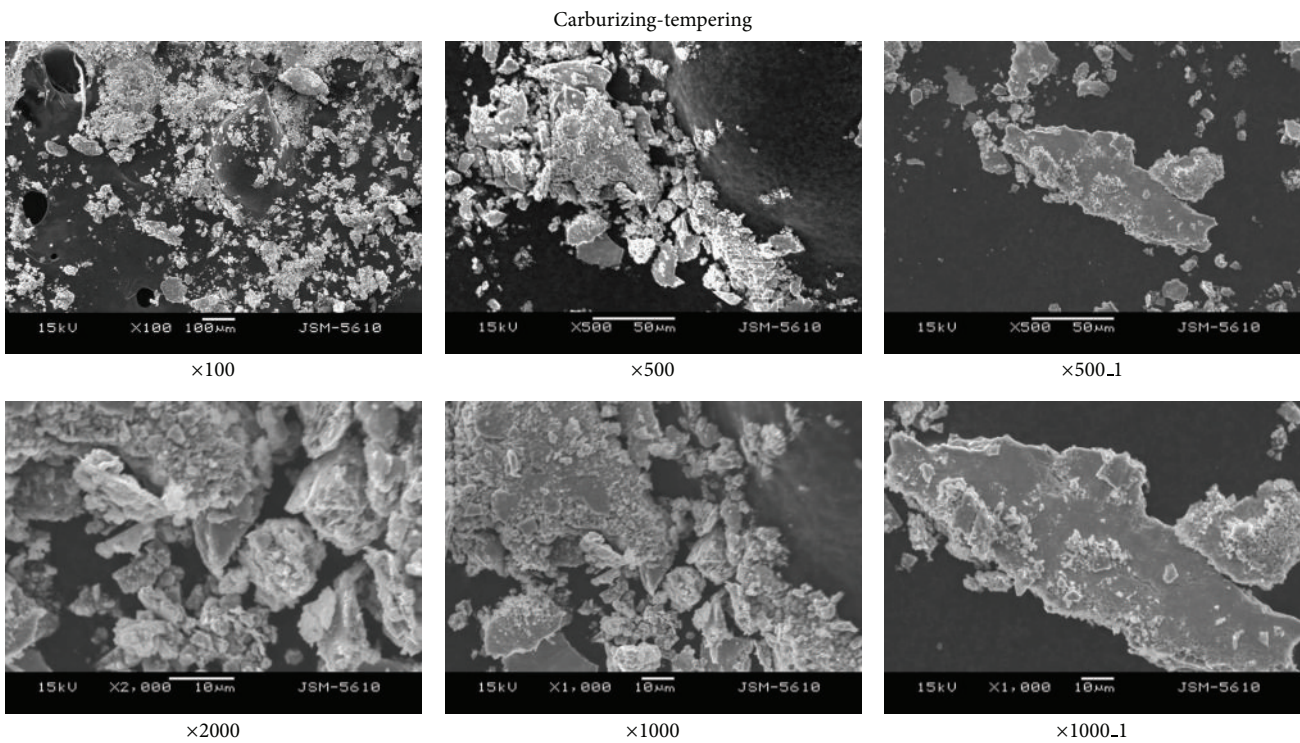


FIGURE 9: Representative SEM micrographs of wear particle for SCM415 with carburizing-tempering.

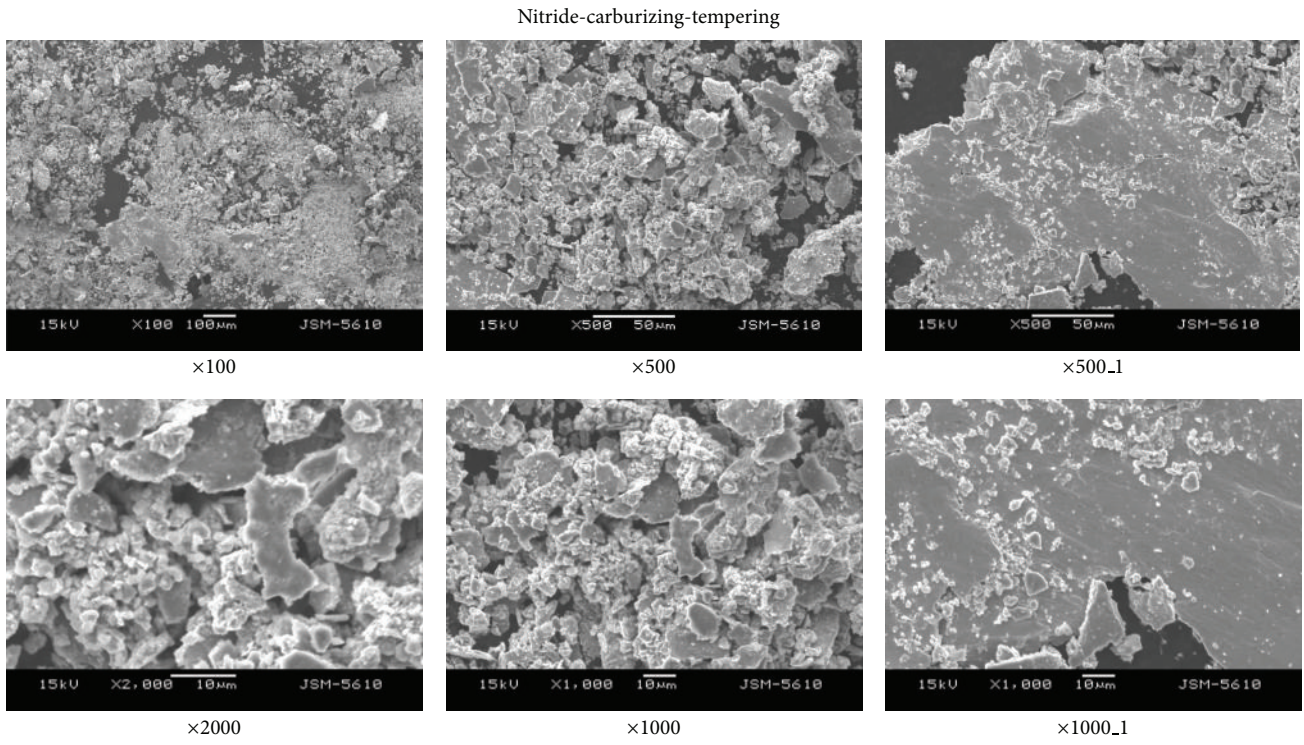


FIGURE 10: Representative SEM micrographs of wear particle for SCM415 with nitride-carburizing-tempering.

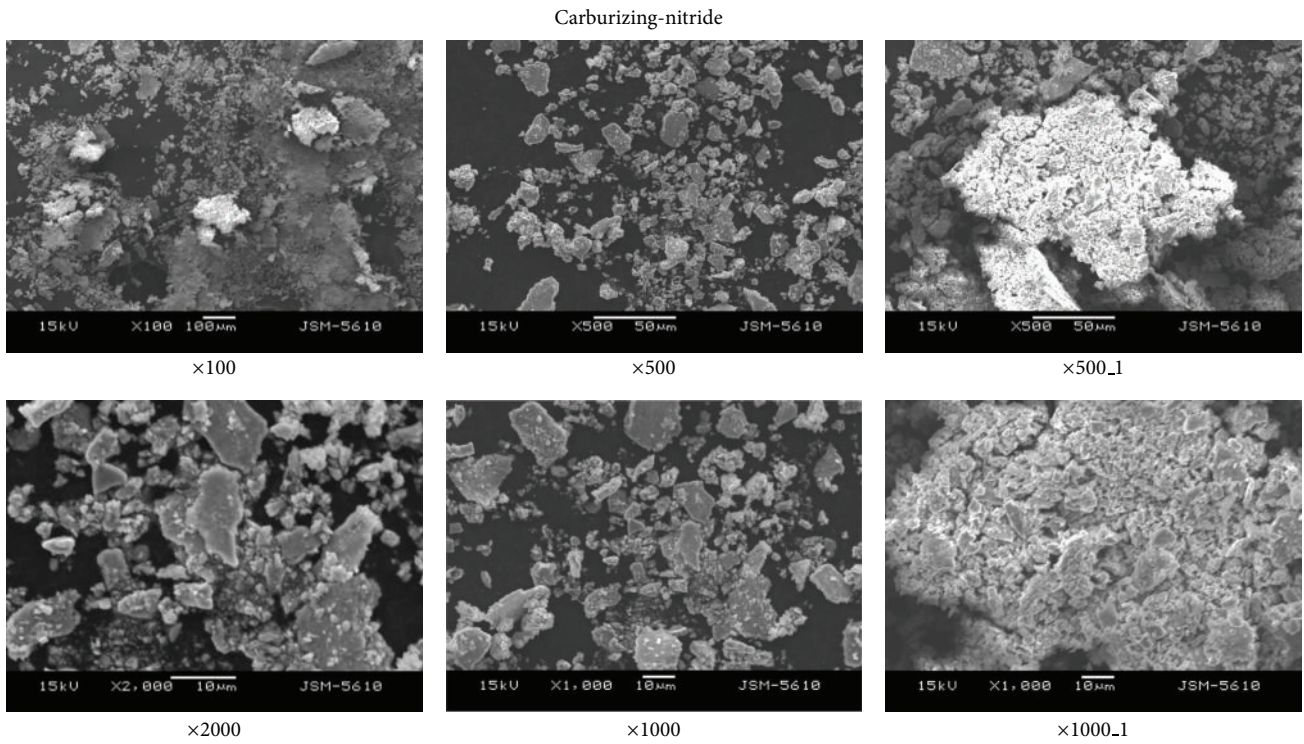


FIGURE 11: Representative SEM micrographs of wear particle for SCM415 with carburizing-nitride.

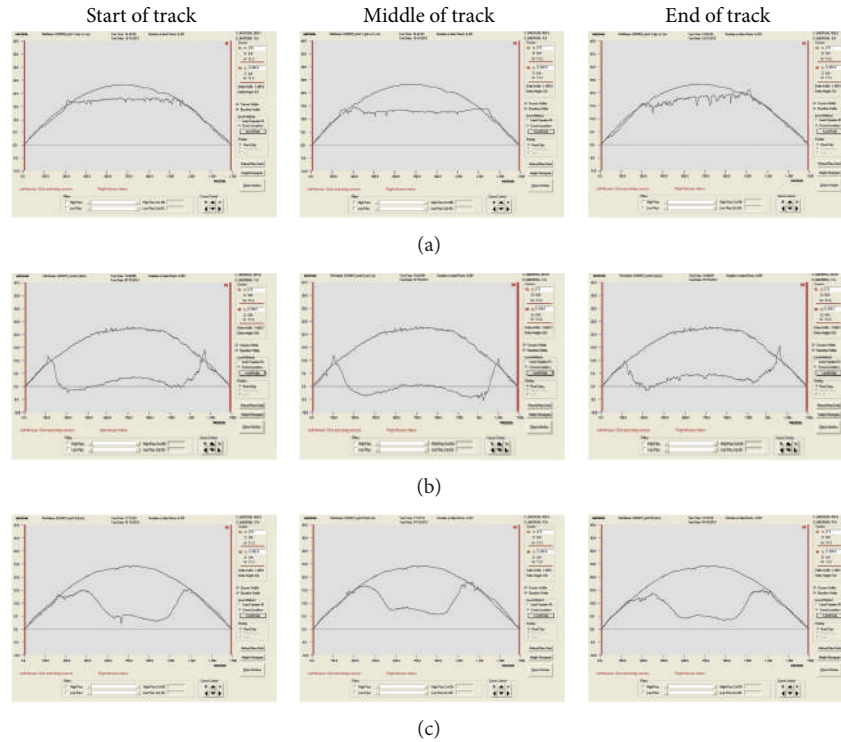


FIGURE 12: (a) Carburizing-tempering: the wear profile for the SCM415 cylinder. (b) Nitride-carburizing-tempering: the wear profile for the SCM415 cylinder. (c) Carburizing-nitride: the wear profile for the SCM415 cylinder.

larger wear particles is over $100\ \mu\text{m}$ order. Moreover, the wear particles are countless and highly concentrated. By a gauss meter, it showed that the surface magnetization was especially larger.

Representative SEM micrographs of wear particle for SCM415 with carburizing-nitride are shown in Figure 11. It is seen from this figure that 50~60% of the wear particles are only several μm order. The size of the larger wear particles is about $10\sim 20\ \mu\text{m}$.

Therefore, the surface magnetization was especially larger for the case of nitride-carburizing. As a result, the wear particles always stay in the interfaces and the wear mechanism becomes complex. Moreover, the amount of wear particle for SCM415 with nitride-carburizing-tempering or carburizing-nitride are significantly larger, that is, severe wear; this can be reasonably explained by the results shown in Figures 6–8. On the other hand, the wear particles are smaller and the wear mechanism is mild for SCM415 with carburizing-nitride. Therefore, it is necessary to put nitride after carburizing for the consideration of wear resistance and low surface magnetization.

Figures 12(a)–12(c) show the wear profile for the SCM415 specimens. It is seen from this figure that the depth of the wear track is only $10.3\ \mu\text{m}$ for SCM415 with carburizing-tempering. However, the depth of the wear track can reach $21.5\ \mu\text{m}$ for SCM415 with nitride-carburizing-tempering. Moreover, the depth of the wear track is about $18.2\ \mu\text{m}$ for SCM415 with carburizing-nitride. Therefore, the wear resistance of the specimens with carburizing-tempering is

significantly larger. Moreover, the wear-resistance of the specimens with carburizing-nitride is larger than the case of nitride-carburizing-tempering.

4. Conclusions

The effects of nitride on the tribological properties of the low carbon alloy steel—SCM415—have been investigated. From the experimental results and the SEM observations of the wear particles, the following conclusions have been drawn.

- (1) The friction coefficient of the specimen with carburizing-nitride is smaller than the other two cases.
- (2) The film of the carburizing-tempering is significantly larger. This is the reason that the wear-resistance of the specimens with carburizing-tempering is larger than the other cases. Moreover, the wear-resistance of the specimens with carburizing-nitride is larger than the case of nitride-carburizing.
- (3) The surface magnetization was especially larger for the case of nitride-carburizing. As a result, the wear particles always stay in the interfaces and the wear mechanism becomes severe and complex.
- (4) It is necessary to arrange nitride after carburizing for the consideration of low friction, wear resistance, and low surface magnetization.

Conflict of Interests

The authors declare that there is no conflict of interests regarding the publication of this paper.

Acknowledgment

The authors would like to express their appreciation to the National Science Council in Taiwan, R.O.C., for their financial support under Grant nos. NSC 101-2221-E-168-012 and NSC 102-2622-E-150-002-CC2.

References

- [1] W. D. Callister, *Material Science, Engineering: An Introduction*, Wiley, New York, NY, USA, 3rd edition, 1994.
- [2] K. E. Thelning, *Steel and Its Heat Treatment, Bofors Handbook*, 1975.
- [3] D. H. Huang and G. Thomas, "Structure and mechanical properties of tempered martensite and lower bainite in Fe–Ni–Mn–C steels," *Metallurgical Transactions*, vol. 2, no. 6, pp. 1587–1598, 1971.
- [4] A. M. Nasreldin, M. M. Ghoneim, F. H. Hammad, R. L. Klueh, and R. K. Nanstad, "Effect of tempering on the toughness of a Cr–Mo bainitic steel," *Journal of Materials Engineering and Performance*, vol. 2, no. 3, pp. 413–420, 1993.
- [5] J. Guodong and H. Maolin, "Research on overheat hardening technology for 5CrMnMo steel," *Material & Heat Treatment*, pp. 74–75, 2008.
- [6] P. Clayton and R. Devanathan, "Rolling/sliding wear behavior of a chromium-molybdenum rail steel in pearlitic and bainitic conditions," *Wear*, vol. 156, no. 1, pp. 121–131, 1992.
- [7] Z. Canxu, Z. Li, D. Yi, and M. Liqun, *Effect of Middle-Temperature Heat-Treatment on Microstructure and Tensile Strength of Ferritic Stainless Steel*, Nanjing University of Technology, Nanjing, China, 2009.
- [8] M. F. Carlson, B. V. Narasimha Rao, and G. Thomas, "The effect of austenitizing temperature upon the microstructure and mechanical properties of experimental Fe/Cr/C steels," *Metallurgical Transactions A*, vol. 10, no. 9, pp. 1273–1284, 1979.
- [9] H. Chai and C. Laird, "Mechanisms of cyclic softening and cyclic creep in low carbon steel," *Materials Science and Engineering*, vol. 93, no. C, pp. 159–174, 1987.
- [10] Y. P. Chang, J. P. Yur, H. M. Chou, and H. M. Chu, "Triboelectrification mechanisms for self-mated carbon steels in dry severe wear process," *Wear*, vol. 260, no. 11-12, pp. 1209–1216, 2006.
- [11] Y. P. Chang, H. M. Chu, and H. M. Chou, "Effects of mechanical properties on the tribo-electrification mechanisms of iron rubbing with carbon steels," *Wear*, vol. 262, no. 1-2, pp. 112–120, 2007.
- [12] Y. P. Chang, Y. Y. Hung, L. M. Chu, J. P. Yur, and C. H. Lin, "The surface magnetization approach on assessing tribological properties of steels with different TiN coatings," *Proceedings of the Institution of Mechanical Engineers J*, vol. 223, no. 4, pp. 715–722, 2009.
- [13] Y. P. Chang, J. H. Horng, J. P. Yur, L.-M. Chu, and Y.-C. Hwang, "The surface magnetization approach on assessing the tribological properties of iron sliding against iron coated with pure tin and with a tin composite," *Proceedings of the Institution of Mechanical Engineers J*, vol. 225, no. 12, pp. 1199–1208, 2011.

Research Article

Properties and Analysis of Transparency Conducting AZO Films by Using DC Power and RF Power Simultaneous Magnetron Sputtering

Neng-Fu Shih,¹ Jin-Zhou Chen,² and Yeu-Long Jiang³

¹ Department of Electronic Engineering, Hsiuping University of Science and Technology, Taichung 412-80, Taiwan

² Graduate Institute of Optoelectronic Engineering, National Chung Hsing University, Taichung 402-27, Taiwan

³ Graduate Institute of Optoelectronic Engineering and Department of Electrical Engineering, National Chung Hsing University, No. 250, Kuo Kuang Road, Taichung 402-27, Taiwan

Correspondence should be addressed to Neng-Fu Shih; nfshih@hust.edu.tw

Received 15 September 2013; Accepted 2 November 2013

Academic Editor: Shoou-Jinn Chang

Copyright © 2013 Neng-Fu Shih et al. This is an open access article distributed under the Creative Commons Attribution License, which permits unrestricted use, distribution, and reproduction in any medium, provided the original work is properly cited.

DC power and RF power were introduced into the magnetic controlled sputtering system simultaneously to deposit AZO films in order to get an acceptable deposition rate with high quality transparency conducting thin film. The resistivity decreases with the RF power for the as-deposited samples. The resistivity of $6 \times 10^{-4} \Omega\text{-cm}$ and $3.5\text{--}4.5 \times 10^{-4} \Omega\text{-cm}$ is obtained for the as-deposited sample, and for all annealed samples, respectively. The transmittance of the AZO films with higher substrate temperature is generally above 80% for the incident light wavelength within 400–800 nm. The transmittance of the as-deposited samples reveals a clear blue shift phenomenon. The AZO films present (002) oriented preference as can be seen from the X-ray diffraction curves. All AZO films reveal compressive stress. The annealing process improves the electrical property of AZO films. A significant blue shift phenomenon has been found, which may have a great application for electrode in solar cell.

1. Introduction

High transparent metal oxide semiconductor with band gap larger than the energy of visible light is usually a good insulator at room temperature [1]. Impurities doping is the easy way to increase conductivity. Tin doped indium oxide (ITO) [2], aluminum doped zinc oxide (AZO) [3, 4], and fluorine doped tin oxide $\text{SnO}_2 : \text{F}$ (FTO) [5] are quite popular materials as transparent semiconductors. ITO, the best transparent conducting film, is a solid solution of indium (III) oxide (In_2O_3) and tin (IV) oxide (SnO_2), typically 90% In_2O_3 , 10% SnO_2 by weight. However, with high cost and limited supplies of indium, alternatives are being sought. Another choice for transparency conducting film is FTO, which is widely used in dye-sensitized solar cell. However, it is very easy for hydrogen plasma to etch FTO, as well as tin oxide. The utilization of FTO and SnO_2 in the thin

film solar cell application is limited. AZO films are a good candidate as a transparent conductive material, because the materials (1) consist of cheap and abundant element, (2) are readily produced for large-scale coating, (3) allow tailoring of ultraviolet absorption, (4) have a high stability in hydrogen plasma, and (5) have low growth temperature [6]. Besides, it is nontoxic and easy to fabricate. The reasons for higher conductivity of Al doped ZnO films can be attributed to extrinsic donor and intrinsic donor [7, 8]. The Al replaces Zn ions to form extrinsic donors, as well as from oxygen vacancies and Zn interstitial atoms to form intrinsic donor [7, 8]. Production of the high conductivity and high transparency AZO films by controlling the intrinsic defects is highly desired for industrial application. Fang et al. deposited AZO film at 320°C by the DC sputtering with postdeposition annealing at 400°C for 2 hours under 10^{-3} Pa and got the resistivity as low as $1.5 \times 10^{-4} \Omega\text{-cm}$ [6]. Park et al. used

the RF sputtering method with 500°C high substrate temperature to get the lowest resistivity of $1.30 \times 10^{-4} \Omega\text{-cm}$ [9]. Kim et al. used a DC cosputtering method followed by rapid thermal annealing to achieve a low resistivity of $1 \times 10^{-3} \Omega\text{-cm}$ [10]. Ohta et al. investigated rapid thermal annealing of sputter-deposited ZnO and AZO films by using a radio-frequency (RF) argon thermal plasma jet at atmospheric pressure, and the lowest resistivity is around $3 \times 10^{-4} \Omega\text{-cm}$ [11]. Exarhos et al. used 30% O₂/Ar gas mixture and 150 W RF sputtering method, followed by 4% hydrogen in argon 725 K annealing [12]. Chen et al. used 1.5% AZO target and O₂/Ar gas mixture sputtering AZO film, followed by vacuum annealing, and analyzed its component with X-ray photoemission spectrum (XPS) and Auger electron spectrum (AES) [13]. Guillen et al. [14] used DC sputtering at room temperature, annealed it in vacuum at 350°C, and got the best resistivity of $8 \times 10^{-4} \Omega\text{-cm}$. Lee [15] uses RF sputtering in H₂ and Ar mixture which reaches a minimum value of $4.4 \times 10^{-4} \Omega\text{-cm}$ at the H₂/(H₂ + Ar) gas ratio of 2.5%. These AZO films are good choices for high conductivity and high transparency film. The AZO film made by RF sputtering seems to have better electrical property than that made by DC sputtering [16]. However, AZO film made by DC sputtering method has higher deposition rate than that made by RF sputtering method. Few factors will affect the quality, transparency, and conductivity of AZO films, such as grain size, crystallinity, and defects of different types [17]. In this work, we report the results of making AZO films using DC and RF sputtering simultaneous methods both as-deposited and annealed samples, to check their conductivity with acceptable deposition rate.

2. Materials and Methods

2.1. Specimen Preparation. Content of the target used in this work is 2 wt. % Al₂O₃ and 98 wt. % ZnO. A corning 1737 glass was used as a substrate. After cleaning, the target and the substrate were put into a magnetron sputtering system and evacuated to 6.7×10^{-3} Pa. Then Ar gas with 70 cm³/min flow rate was introduced into the reaction chamber. After turning on the DC power supplier and RF power supplier, the target was presputtering for 5 minutes to remove surface contamination. Then open the shutter and sputter for 30 min at the pressures of 2.7×10^{-1} Pa. We have tested 3 different DC power suppliers to check the film quality with 30, 50, and 80 W and found that 80 W was the best choice for the film's quality. Therefore, the DC power supplier was kept at 80 W, while the RF power was varied from 0 W to 120 W. Five substrate temperatures 225, 250, 275, 300, and 325°C were chosen for deposition. After deposition, one group of substrates was put into a high temperature furnace under a 550°C substrate temperature with 6% H₂/Ar annealing for an hour to investigate the improvement of film quality. The thickness of films was measured by a Tencor alphastep 500 surface profiler, and the resistivity of films was measure by an ECOPIA model HMS-200 Hall Effect measurement system.

2.2. Crystalline Size. Crystalline size of AZO film can be evaluated from the FWHM of XRD peak and diffraction angle of the peak by the formula [7, 8]

$$D_p = \frac{0.94\lambda}{\beta_{1/2} \cos \theta}, \quad (1)$$

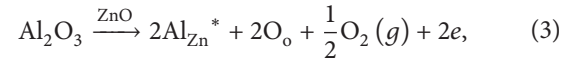
where D_p is the crystalline size, $\beta_{1/2}$ is the full width at half maximum of the diffraction peak, λ is the incident X-ray wavelength (= 0.154 nm), and θ is diffraction angle of the peak.

2.3. In-Plane Stress. For hexagonal crystals with a high c -axis preferred orientation, the in-plane stress can be calculated based on the biaxial strain model [18–20]:

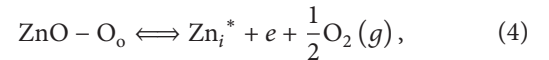
$$\sigma = \left[2C_{13} - \frac{C_{33}(C_{11} + C_{12})}{C_{13}} \right] \frac{(d - d_0)}{2d_0}, \quad (2)$$

where d is the interplaner spacing corresponding to (002) reflex in the XRD pattern, d_0 is that in bulk ZnO (0.2603 nm), and C_{ij} is elastic stiffness constants. The values of d were calculated using Bragg formula $2d \sin \theta = n\lambda$.

2.4. Electrical Considerations. The doping of Al₂O₃ into ZnO structure is given by the equation [6, 10, 21, 22]



where Al_{Zn}^{*} is the substitutional Al, O_o is the oxygen vacancy, and e is the free electron. For the AZO film annealing under a vacuum process, a considerable increase in conductivity was obtained due to the increase in oxygen defects, which acted as electron donors. In the meantime, the annealing process has the effect of increasing grain size and crystallinity of the film, which therefore results in less grain boundary scattering [9]. On the other hand, loss of oxygen from the crystal will also produce the interstitial zinc atoms according to the reaction [6, 10, 21, 22]:



where Zn_i^{*} is the interstitial zinc atoms. It means that the intrinsic donor can be increased by the hydrogen annealing process, thus, increasing the conductivity.

3. Results and Discussion

3.1. Structural Characteristics and Film Stress. Figure 1 illustrates the X-ray diffraction (XRD) patterns for the AZO film. The XRD patterns were measured by the use of a Rigaku XRD model PC-2000. The full width at half maximum of the diffraction peak $\beta_{1/2}$ and diffraction angle of the peak θ are determined from XRD patterns as illustrated in Figure 1. The diffraction peak intensity increases with the increasing substrate temperature, as can be seen from Figure 1. The increasing diffraction peak intensity of (002) between 225 and 325°C is primarily due to the crystallization of the AZO film.

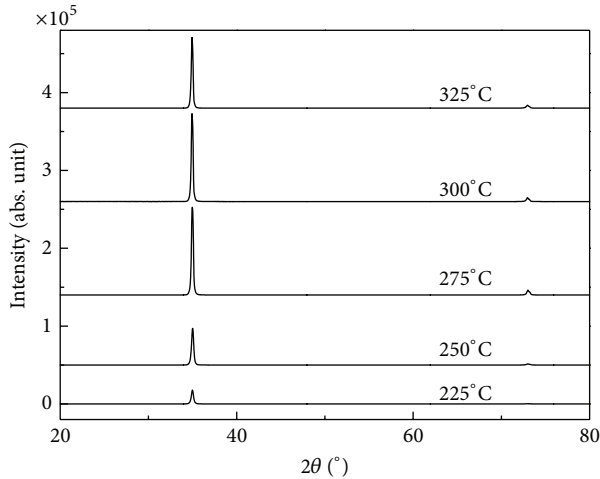


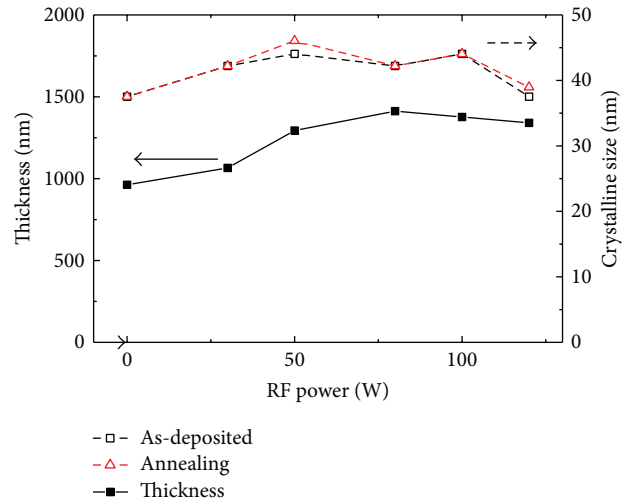
FIGURE 1: The XRD patterns for the AZO film deposited at a pressure of 2.7×10^{-1} Pa.

The solid squares in Figure 2(a) give the thickness for the sputtered AZO films versus incident RF power. The thicknesses of the sputtered films are around 963–1412 nm. Obviously, the thickness increases with incident RF power for RF power ≤ 80 W but decreases with the incident RF power when RF power > 80 W. The increase of the thickness for RF power ≤ 80 W is primarily due to the increasing total incident power. That increases the ionization rate of the introduced Ar gas. The decrease of the thickness with the incident RF power, when RF power > 80 W, could be because positive cycle of the incident RF power is larger than the negative biased DC power ($= 80$ W). That decreases the ionization rate of the introduced Ar gas. The deposition rates for RF power = 0, 30, 50, 80, 100, and 120 W are 0.54, 0.59, 0.72, 0.79, 0.77, and 0.75 nm/s, respectively. The crystalline sizes of AZO films are also given in Figure 2(a), where the open squares indicate as-deposited samples and open triangles annealing samples.

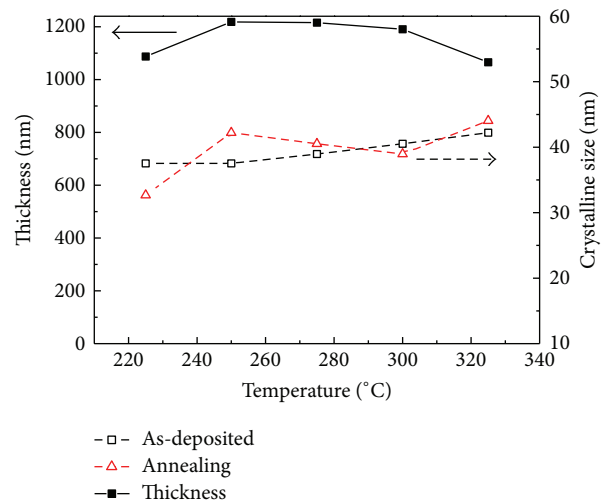
The crystalline sizes of AZO films are 37.5, 42.2, 44.0, 42.2, 44.0, and 37.5 nm for RF power is 0, 30, 50, 80, 100, and 120 W, respectively. The crystalline sizes of the films generally are kept around 43 nm, except when RF is 0 W or 120 W. The crystalline sizes of AZO films are 37.5, 37.5, 39.0, 40.5, and 42.2 nm for the substrate temperature varies from 225, 250, 275, 300, to 325°C, respectively. The crystalline sizes increase with the substrate temperature.

The solid squares in Figure 2(b) give the thickness versus substrate temperature. The deposition rate of AZO film is 0.60, 0.68, 0.68, 0.66, and 0.59 nm for substrate temperature of 225, 250, 275, and 300 and 325°C, respectively. The AZO film has the highest deposition at 250°C substrate temperature and then, decreases with the substrate temperature.

Figure 3(a) gives the in-plane stress for the AZO as deposited at 325°C with various RF power; the stress generally increases with the RF power. Figure 3(b) shows the in-plane stress for the AZO as deposited at 225, 250, 275, 300, and 325°C, respectively. The results of Figure 3 are calculated from (2), where $C_{11} = 208.8 \times 10^9$ N/m², $C_{33} = 213.8 \times 10^9$ N/m², $C_{12} = 119.7 \times 10^9$ N/m², and $C_{13} = 104.2 \times 10^9$ N/m² were



(a)



(b)

FIGURE 2: The thickness and the crystalline size for the sputtered AZO films versus (a) the incident RF power and (b) the substrate temperature.

used [17–19]. 80 W DC power and 30 W RF power were used during sputtering. The minus sign indicates the compressive stress. The stress generally increases with the RF power and increases to 1.41×10^9 N/m² from 225 to 250°C substrate temperature and then decreases to 0.40×10^9 N/m².

The total film stress contains thermal stress and intrinsic stress. The thermal stress comes from thermal mismatch between AZO thin films and glass substrate. The generation mechanism of the intrinsic stress was caused by the growth process itself. Since the thermal stress is very small, film stress is mainly caused by the growth process itself [18]. Comparing Figures 2 and 3, we conclude that higher deposition rate makes the film stress higher.

3.2. Electrical Characteristics. Figure 4 shows electrical property of the sputtered AZO film versus substrate temperature,

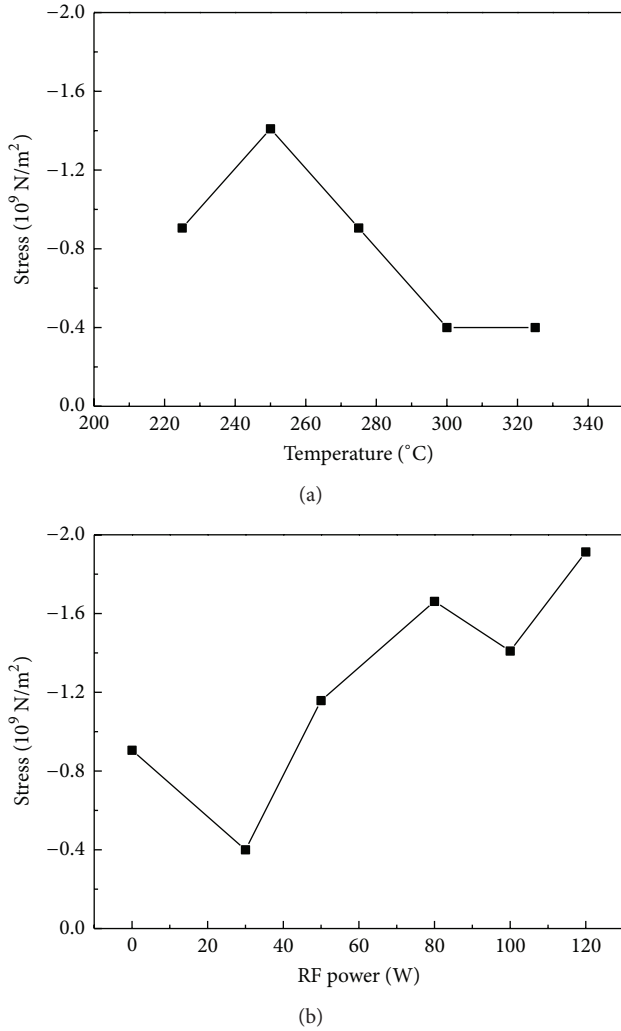


FIGURE 3: The in-plane stress for the AZO as deposited at 325°C with (a) various RF power and (b) various substrate temperatures.

where the dash lines indicate the resistivity, solid lines the electron concentration, and the dot lines the electron mobility, respectively. The squares indicate the as-deposited samples and the triangles the annealed samples, respectively.

The electron mobility for the annealed samples increases with the substrate temperature and is larger than that of the as-deposited samples, which could be due to the recrystallization of the annealed samples that increases the grain size which increase the electron mobility. The electron concentration of the annealed samples decreases with the increasing substrate temperature. For the as-deposited samples, both electron mobility and electron concentration increase with the increasing substrate temperature. Heating the AZO film, a considerable increase in conductivity was obtained due to the increase in oxygen defects, which increase the electron concentration in the film [9, 10]. In the meantime, the thermal process has the effect of increasing grain size and crystallinity of the film, which results in less grain boundary scattering [6, 9, 10]. These combined actions increase the conductivity. Therefore, the resistivity decreases with the

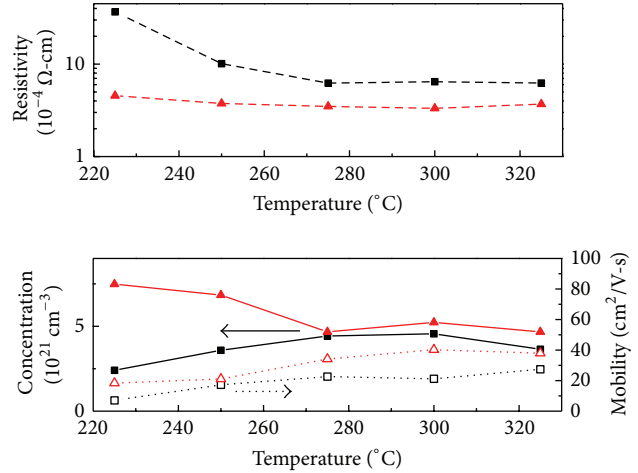


FIGURE 4: The electrical property of the sputtered AZO film versus the substrate temperature.

increasing substrate temperature except for the annealed samples, since the resistivity is reciprocal to the product of electron concentration and electron mobility. The resistivity of annealed samples, although decreasing with the increasing substrate temperature, was kept around $3.5\text{--}4.5 \times 10^{-4} \Omega\text{-cm}$. This could be due to the decrease of electron concentration at higher substrate temperature. Hydrogen annealing process introduces the hydrogen into the AZO film, resulting in a shallow donor in AZO film [11].

Figure 5 shows electrical property of the sputtered AZO film versus RF power with substrate temperature 325°C , where the dash lines indicate the resistivity, solid lines the electron concentration, and the dot lines the electron mobility, respectively. The squares indicate the as-deposited samples, and the triangles indicate the annealed samples, respectively. The resistivity of the as-deposited samples decreases with the RF power. The electron concentration increases slightly with the incident RF power for the as-deposited samples; however, the mobility of AZO film decreases slightly with the incident RF power.

3.3. Optical Properties. The transmittance was measured by the use of a Jasco model V-670 UV-VIS spectrophotometer. Figure 6 gives the transmittance of the as-deposited films for different substrate temperatures, where solid squares indicate 225°C , open circles 250°C , solid upper triangles 275°C , open down triangles 300°C , and solid diamonds 325°C . The transmittance for the AZO film with 325°C substrate temperature is above 80% within the visible light region, and transmittance with 275 and 300°C substrate temperatures is around 80% for the incident wavelength around 400 nm and is above 80% for the incident wavelength longer than 450 nm. The transmittance for substrate temperatures of 225 and 250°C is around 60% for the incident wavelength near 400 nm and is also above 80% for the incident wavelength longer than 450 nm. This wider transmittance spectrum for high substrate temperature samples implicated the more absorption efficiency for the solar cell application. Particularly,

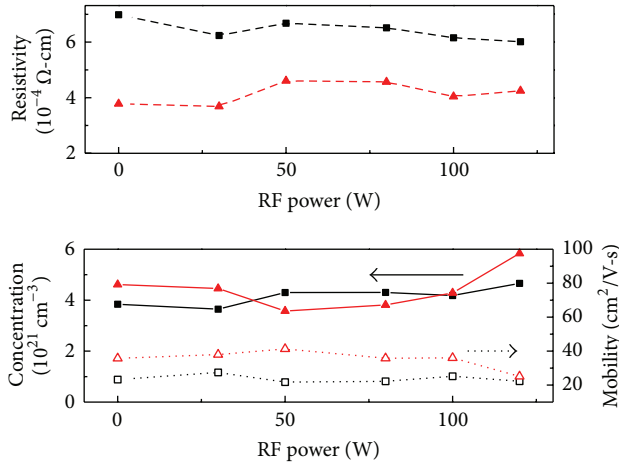


FIGURE 5: The electrical property of the sputtered AZO film versus the RF power.

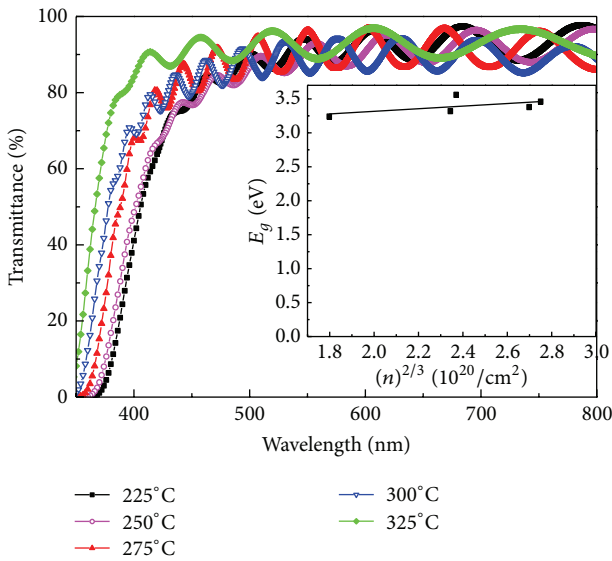


FIGURE 6: The transmittance of the as-deposited films for different substrate temperatures.

the transmittance of the as-deposited samples reveals a clear blue shift phenomenon. This is primarily due to the Burstein-Moss shift effect [12, 23]. Burstein-Moss shift is calculated by using the following equation:

$$E_F - E_{CB} = \left(\frac{\hbar^2}{2m_e^*} \right) (3\pi^2 n)^{2/3}, \quad (5)$$

where m_e^* is the electron effective mass, E_F the Fermi level, E_{CB} the conduction-band edge, and n the carrier concentration, respectively [12]. The insertion of Figure 5 gives optical band gap E_g versus carrier concentration $n^{2/3}$ and reveals a good linear relationship between optical band gap E_g and carrier concentration $n^{2/3}$. Therefore, we deduce that the blue shift of the transmission within 350–390 nm could be due to the Burstein-Moss shift effect.

4. Summary and Conclusions

AZO films were deposited by a magnetic control sputtering system using DC power and RF power simultaneously under different sputtering conditions. The AZO films present (002) oriented preference. The deposition rates for RF power = 0 W to 80 W increase from 0.54 nm/s to 0.79 nm/s which are good for mass production. In-plane stress for all AZO films reveals compressive stress. The stress increases with the RF power, increases to 1.41×10^9 N/m² from 225 to 250°C substrate temperature, and then decreases to 0.40×10^9 N/m². The transmittance for the film with higher substrate temperature is generally above 80% in the 400 nm~800 nm visible light region. The electron mobility for the annealed samples is larger than that of the as-deposited samples due to the recrystallization of the annealed samples that increase the grain size, resulting in the increasing electron mobility. The lowest resistivity for the annealed samples is 3.5×10^{-4} Ω-cm which is the best result ever reported by using DC and RF sputtering simultaneously. Furthermore, the sample with higher deposition temperature revealed a significant blue shift phenomenon which may have a great application for electrode in solar cell.

Conflict of Interests

The authors hereby declare that there is no conflict of interests with any financial organization regarding the material discussed in the paper.

Acknowledgment

This work was supported by the National Science Council Taiwan, under Grant NSC100-2221-E-164-004.

References

- [1] J. L. Vossen, "Transparent conducting films," *Physics of Thin Films*, vol. 9, pp. 1-64, 1977.
- [2] L. Davis, "Properties of transparent conducting oxides deposited at room temperature," *Thin Solid Films*, vol. 236, no. 1-2, pp. 1-5, 1993.
- [3] H. W. Lehmann and R. Widmer, "Preparation and properties of reactively co-sputtered transparent conducting films," *Thin Solid Films*, vol. 27, no. 2, pp. 359-368, 1975.
- [4] H. S. Randhawa, M. D. Matthews, and R. F. Bunshah, "SnO₂ films prepared by activated reactive evaporation," *Thin Solid Films*, vol. 83, no. 2, pp. 267-271, 1981.
- [5] E. Shanthi, A. Banerjee, V. Dutta, and K. L. Chopra, "Electrical and optical properties of tin oxide films doped with F and (Sb+F)," *Journal of Applied Physics*, vol. 53, no. 3, pp. 1615-1621, 1982.
- [6] G. Fang, D. Li, and B.-L. Yao, "Fabrication and vacuum annealing of transparent conductive AZO thin films prepared by DC magnetron sputtering," *Vacuum*, vol. 68, no. 4, pp. 363-372, 2002.
- [7] B. D. Cullity and S. R. Stock, *Elements of X-Ray Diffraction*, Prentice-Hall, 3rd edition, 2001.

- [8] A. L. Patterson, "The scherrer formula for X-ray particle size determination," *Physical Review*, vol. 56, no. 10, pp. 978–982, 1939.
- [9] J. H. Park, J. M. Shin, S.-Y. Cha et al., "Deposition-temperature effects on AZO thin films prepared by RF magnetron sputtering and their physical properties," *Journal of the Korean Physical Society*, vol. 49, no. 2, pp. S584–S588, 2006.
- [10] Y. Kim, W. Lee, D.-R. Jung et al., "Optical and electronic properties of post-annealed ZnO:Al thin films," *Applied Physics Letters*, vol. 96, no. 17, Article ID 171902, 2010.
- [11] N. Ohta, D. Ohba, S. Sato, Z. Tang, H. Shimizu, and H. Shirai, "Rapid thermal-plasma annealing of ZnO:Al films for silicon thin-film solar cells," *Thin Solid Films*, vol. 519, no. 20, pp. 6920–6927, 2011.
- [12] G. J. Exarhos, A. Rose, and C. F. Windisch Jr., "Spectroscopic characterization of processing-induced property changes in doped ZnO films," *Thin Solid Films*, vol. 308-309, no. 1–4, pp. 56–62, 1997.
- [13] M. Chen, X. Wang, Y. H. Yu et al., "X-ray photoelectron spectroscopy and auger electron spectroscopy studies of Al-doped ZnO films," *Applied Surface Science*, vol. 158, no. 1, pp. 134–140, 2000.
- [14] C. Guillén and J. Herrero, "Optical, electrical and structural characteristics of Al:ZnO thin films with various thicknesses deposited by DC sputtering at room temperature and annealed in air or vacuum," *Vacuum*, vol. 84, no. 7, pp. 924–929, 2010.
- [15] J.-H. Lee, "Effects of hydrogen incorporation and heat treatment on the properties of ZnO:Al films deposited on polymer substrate for flexible solar cell applications," *Current Applied Physics*, vol. 10, no. 3, pp. S515–S519, 2010.
- [16] W. Yang, Z. Wu, Z. Liu, A. Pang, Y.-L. Tu, and Z. C. Feng, "Room temperature deposition of Al-doped ZnO films on quartz substrates by radio-frequency magnetron sputtering and effects of thermal annealing," *Thin Solid Films*, vol. 519, no. 1, pp. 31–36, 2010.
- [17] K. H. Ri, Y. B. Wang, W. L. Zhou, J. X. Gao, X. J. Wang, and J. Yu, "The effect of SiO₂ buffer layer on the electrical and structural properties of Al-doped ZnO films deposited on soda lime glasses," *Applied Surface Science*, vol. 257, no. 13, pp. 5471–5475, 2011.
- [18] T. B. Bateman, "Elastic moduli of single-crystal zinc oxide," *Journal of Applied Physics*, vol. 33, no. 11, pp. 3309–3312, 1962.
- [19] Y.-Y. Chen, P. W. Wang, J.-C. Hsu, and C.-Y. Lee, "Post-annealing properties of aluminum-doped zinc oxide films fabricated by ion beam co-sputtering," *Vacuum*, vol. 87, pp. 227–231, 2013.
- [20] L. Li, L. Fang, X. M. Chen et al., "Influence of oxygen argon ratio on the structural, electrical, optical and thermoelectrical properties of Al-doped ZnO thin films," *Physica E*, vol. 41, no. 1, pp. 169–174, 2008.
- [21] J. F. Chang, W. C. Lin, and M. H. Hon, "Effects of post-annealing on the structure and properties of Al-doped zinc oxide films," *Applied Surface Science*, vol. 183, no. 1-2, pp. 18–25, 2001.
- [22] N. F. Shih, C. C. Lin, and C. Y. Kung, "Effect of oxygen contents on the properties of Al-Doped ZnO films prepared by low temperature magnetic controlled DC sputtering," *Japanese Journal of Applied Physics*, vol. 52, no. 1, Article ID 01AC07, 2013.
- [23] B. E. Sernelius, K.-F. Berggren, Z.-C. Jin, I. Hamberg, and C. G. Granqvist, "Band-gap tailoring of ZnO by means of heavy Al doping," *Physical Review B*, vol. 37, no. 17, pp. 10244–10248, 1988.

Research Article

Design and Fabrication of the Large Thrust Force Piezoelectric Actuator

Shyang-Jye Chang and Jing Chen

Department of Mechanical Engineering, National Yunlin University of Science and Technology, EM334B, 123 University Road, Section 3, Douliou, Yunlin 64002, Taiwan

Correspondence should be addressed to Shyang-Jye Chang; changjye@yuntech.edu.tw

Received 12 September 2013; Accepted 2 November 2013

Academic Editor: Shouu-Jinn Chang

Copyright © 2013 S.-J. Chang and J. Chen. This is an open access article distributed under the Creative Commons Attribution License, which permits unrestricted use, distribution, and reproduction in any medium, provided the original work is properly cited.

This paper presents a novel piezoelectric actuator containing double pushers. By using finite element analysis software, this study simulated the vibration mode and amplitude of piezoelectric actuators. The Taguchi method was used to design the parameters of piezoelectric actuators including length, width, height, and electrodes setting. This paper also presents a discussion regarding the influence that the design parameters had on the actuator amplitudes. Based on optimal design parameters, a novel piezoelectric actuator containing double pushers is produced and some thrust tests are also carried out. From the experiment results, the piezoelectric actuator containing double pushers can provide a greater thrust force than that of traditional actuators containing a single pusher as the preload is greater. Comparing with the traditional actuators, the thrust force of new actuator can be increased by 48% with the double preload.

1. Introduction

In 1982, the first piezoelectric actuator was produced by Shinsei. In 1987, piezoelectric actuators were installed in dot matrix printers and mass-produced; this was the first time piezoelectric actuators were used in commercial applications. Canon and Minolta successively applied piezoelectric actuators in the autofocus and shutter units of cameras. In the late 1990s, Toyota used piezoelectric actuators in the automobile industry, specifically in the suspension system and seat adjustment controls of vehicles. In 1995, Epson used piezoelectric actuators to develop print heads in ink-jet printers, thereby beginning the industrial trend of applying piezoelectric actuators in various microsystems [1].

Piezoelectric actuators are categorized into standing-wave and traveling-wave actuators according to the drive modes. The vibration mode of traveling-wave actuators is a ripple, which travels in an oval trajectory. The motion trajectories of standing-wave actuators are oval, linear, or of other shapes. The biggest difference between the two types is the wave node, which can be used as a reference

when designing fixed points. Traveling-wave actuators do not contain wave nodes, thereby limiting the mechanical design; standing-wave actuators possess wave nodes, which ensure relatively simple designs that are easily miniaturized.

According to the drive signals, piezoelectric actuators are categorized into single-phase [2–5], double-phase [6–9], and multiphase actuators [5, 10–12]. The motion trajectory of single-phase piezoelectric actuators is nearly linear. Because of a lack of phase differences, single-phase piezoelectric actuators possess a simple driver circuit design and high output efficiency. Double- and multiphase piezoelectric actuators travel in oval trajectories because they are driven by multiple modes. Consequently, the circuit design of these actuators is complex. When two vibration modes are simultaneously excited, differences in frequency tend to prevent effective resonance, thereby lowering efficiency. This setback in double- and multiphase piezoelectric actuators must be rectified. Based on single-phase standing-wave piezoelectric actuators, this study designed a novel piezoelectric actuator containing double pushers.

2. Materials and Methods

2.1. Concepts. When periodic electrical energy is excited in piezoelectric actuators, periodic deformation occurs. This periodic motion then causes linear or rotational motion in objects because of the friction that pushes or drives objects. Figure 1 presents the driving principles of the vibration mode in an actuator using a single pusher. In traditional designs, vibration modes use single points to produce friction (driving force). Theoretically, if two driving points are used, increased friction can be generated to drive objects, and actuators with greater thrust forces can be designed. The vibration mode of the proposed actuator containing double pushers is shown in Figure 2.

2.2. Parameters Design. Taguchi method is a kind of design of experiment (DOE) developed by Genichi Taguchi. It has been widely used to improve the quality of a product or a manufacturing process by means of statistical method. It usually obtains the optimal design factors by tools such as S/N ratio and orthogonal arrays [13].

In this study, “the average vibration amplitude of two different driving points on the piezoelectric plate” is chosen to be the quality characteristics. The quality characteristic is larger-the-better since the larger vibration amplitude is expected. All possible design factors that affect “the average vibration amplitude of two different driving points on the piezoelectric plate” were considered by a brainstorming in an early design stage. The width of the piezoelectric actuator, the length of the piezoelectric actuator, the thickness of the piezoelectric actuator, and the electrode setting are chosen to be the design factors. The four chosen control factors and their levels for the experiment are shown in Table 1. An L_{18} array is used to set the parameter optimization experiment levels.

3. Results and Discussion

3.1. Simulation Results. Table 2 and Figure 3 are the quality characteristic response table in X -direction and the factor effects response plot in X -direction, respectively. It is obvious that each factor on the quality characteristics is influential. The order of their contribution is $B > C > A > D$. The biggest vibration amplitude of these two driving points in the X direction will occur with the following combination of factors: A_2 , B_2 , C_1 , and D_3 .

Table 3 and Figure 4 are the quality characteristic response table in Y -direction and the factor effects response plot in Y -direction, respectively. It is also obvious that each factor on the quality characteristics is influential. The order of their contribution is $B > C > D > A$. The biggest vibration amplitude of these two driving points in the Y -direction will occur with the following combination of factors: A_2 , B_2 , C_1 , and D_1 .

Comparing the above results, it is found that the effects of factors A , B , and C have good consistency for the X -direction or Y -direction vibration amplitude. The maximum vibration amplitude of the two driving points on the piezoelectric actuator, both in the X -direction and Y -direction, occurs

TABLE 1: The control factors and levels table.

Factor\level	Level 1	Level 2	Level 3
Width (A)	6 mm	8 mm	
Length (B)	14 mm	16 mm	18 mm
Thickness (C)	1 mm	1.5 mm	2 mm
Electrode setting (D)	4 : 6	5 : 5	6 : 4

TABLE 2: The quality characteristic response table in X -direction (unit: m).

	A	B	C	D
Level 1	$3.99E-8$	$2.88E-8$	$6.97E-8$	$4.54E-8$
Level 2	$7.10E-8$	$8.83E-8$	$5.89E-8$	$5.53E-8$
Level 3		$4.92E-8$	$3.78E-8$	$6.56E-8$
Range	$3.11E-8$	$5.95E-8$	$3.19E-8$	$2.02E-8$
Rank	3	1	2	4

TABLE 3: The response table in Y -direction (unit: m).

	A	B	C	D
Level 1	$6.42E-8$	$4.96E-8$	$8.80E-8$	$7.77E-8$
Level 2	$7.32E-8$	$8.29E-8$	$5.93E-8$	$5.90E-8$
Level 3		$7.35E-8$	$5.88E-8$	$6.93E-8$
Range	$9.01E-9$	$3.34E-8$	$2.92E-8$	$1.87E-8$
Rank	4	1	2	3

as the factors A , B , and C are on level 2, level 2, and level 1, respectively. The maximum vibration amplitude in the X -direction of the two driving points on the piezoelectric actuator occurs as the factor D is on level 3. However, the maximum vibration amplitude in the Y -direction of the two driving points on the piezoelectric actuator occurs as the factor D is on level 1. Comparing the effects response of factor D in Figure 4, the factor effects response is quite close when the factor D is on level 1 or level 3. Therefore, the factors and settings of A_2 (width = 8 mm), B_2 (length = 16 mm), C_1 (thickness = 1 mm), and D_3 (electrode setting = 6 : 4) are chosen to be the optimal parameters combination.

3.2. Fabrication and Measurements. The pushers should be set at the positions with maximum amplitude on the piezoelectric actuator to produce the larger thrust force. The fixtures should be set at the positions with minimum amplitude on the piezoelectric actuator so as not to affect the operation of the actuator. Figure 5 is the vibrating amplitudes in the X -direction and the Y -direction along the length of piezoelectric actuator. Seeking these two curves in Figure 5, it can be found that the maximum amplitudes, both in the X -direction and the Y -direction, of the piezoelectric actuator occur at the positions of 6 mm and 10 mm. Therefore, the two pushers are set at these positions. The minimum amplitudes, both in the X -direction and the Y -direction, of the piezoelectric actuator occur at the positions of 3 mm and 13 mm. Therefore, the two fixtures are set at these positions. Figure 6 shows the detailed dimensions of the large thrust force piezoelectric actuator with double pushers.

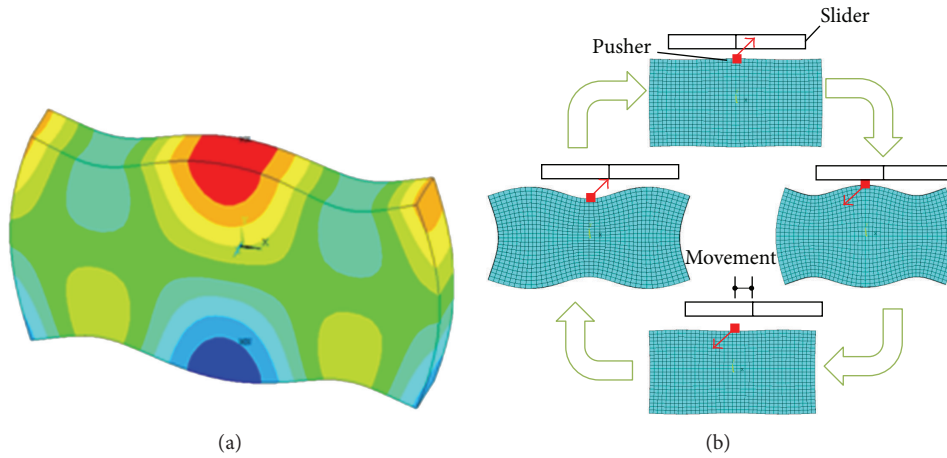


FIGURE 1: (a) Vibration mode of actuator using a single pusher. (b) Driving principles of the actuator.

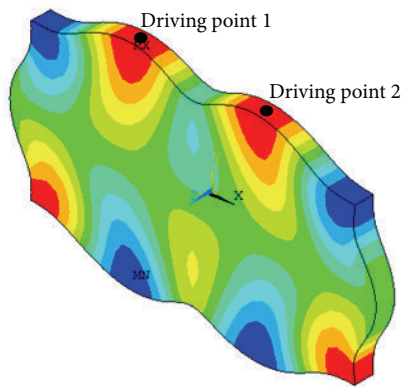


FIGURE 2: Vibration mode of actuator using double pushers.

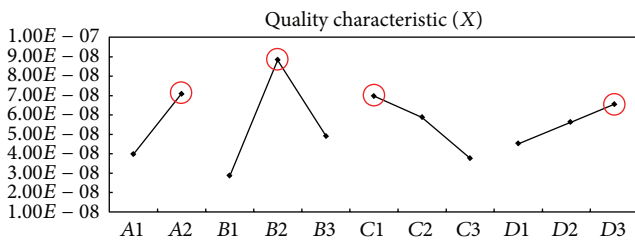


FIGURE 3: The factor effects response plot in X-direction.

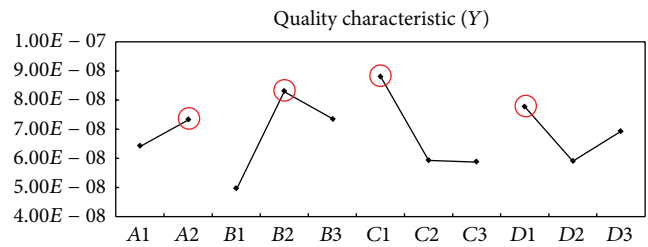


FIGURE 4: The factor effects response plot in Y-direction.

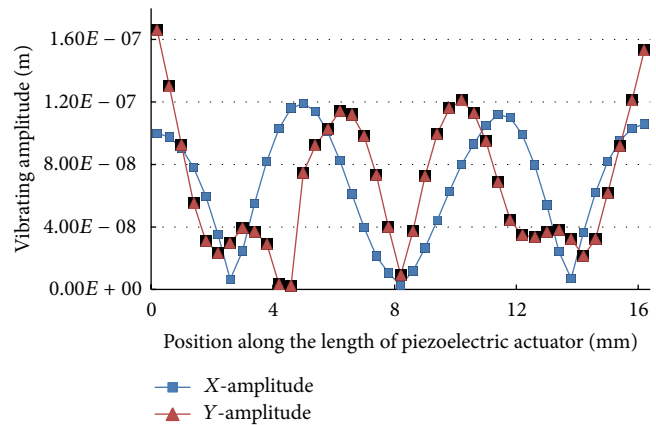


FIGURE 5: The vibrating amplitudes in the X-direction and the Y-direction along the length of piezoelectric plate.

In order to measure the output thrust force of the piezoelectric actuator containing double pushers, this actuator is used in the linear stage. Figure 7 is linear stage using the large thrust force piezoelectric actuator. The linear stage includes a large thrust force piezoelectric actuator, a miniature linear guide, a uniaxial load-cell, a set of preload mechanism, and an adjusting screw. The pushers contact with the carriage on the linear guide. The preload mechanism is set on the other side and contacts with the fixtures on the piezoelectric actuator. By adjusting the screw, the preload mechanism will push the piezoelectric actuator toward the direction of linear guide to produce a proper preload between the pushers and

the carriage on the linear guide. The preload can be measured by the load-cell.

In this study, the thrusts force of novel piezoelectric actuator containing double pushers and the conventional piezoelectric actuator containing a single pusher are measured. The setup of thrust force measurement experiment is shown in Figure 8. The drive signal generated by a function generator is supplied to the piezoelectric actuator through a power amplifier and an oscilloscope is used to monitor the drive signal. A force gauge is used to measure the thrust force

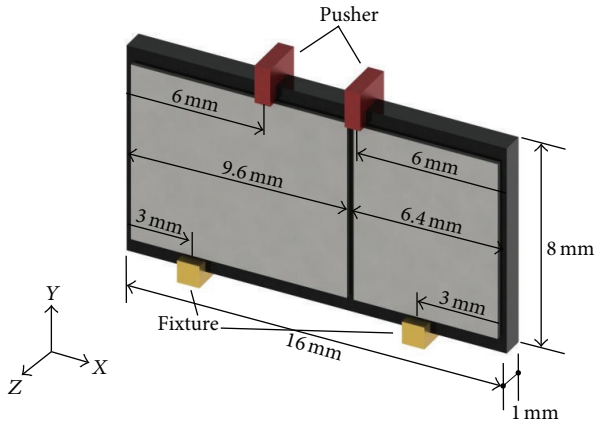


FIGURE 6: The detailed dimensions of the large thrust piezoelectric actuator.

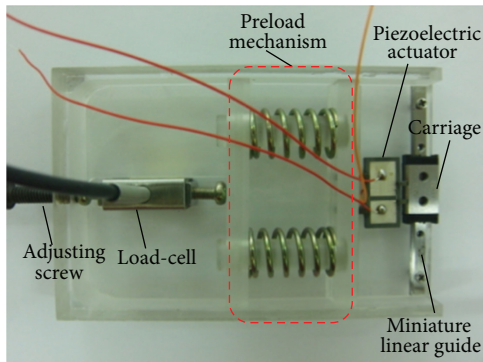


FIGURE 7: The linear stage using the large thrust piezoelectric actuator.

of the linear stage as the piezoelectric actuator is excited. Figure 9 shows the thrust measurement experiment.

The resonance frequency of piezoelectric actuator containing one single pusher obtained by simulation is about 222 kHz. The actual operating frequency is about 218 kHz after the actuator is assembled in the linear stage. After initial testing, the appropriate preload of 215 g is chosen. Too large or small preload will influence the normal operating of the actuator. The thrusts forces of the linear stage with the preload of 215 g and the drive voltage 30 Vpp are shown in Table 4. The average thrust force is about 70 g as the operating frequency is 218 Hz.

The resonance frequency of piezoelectric actuator containing double pushers obtained by simulation is about 261 kHz. The actual operating frequency is about 256 kHz after the actuator is assembled in the linear stage. The thrusts forces of the linear stage with the preload of 215 g and the drive voltage 30 Vpp are shown in Table 5. The average thrust force is about 60 g as the operating frequency is 256 Hz. The performance is worse than the thrust force of piezoelectric actuator containing one single pusher.

The thrust force will be affected because the preload varies since the linear stage is driven via a friction between the pushers and the carriage. Therefore, the measurement experiment

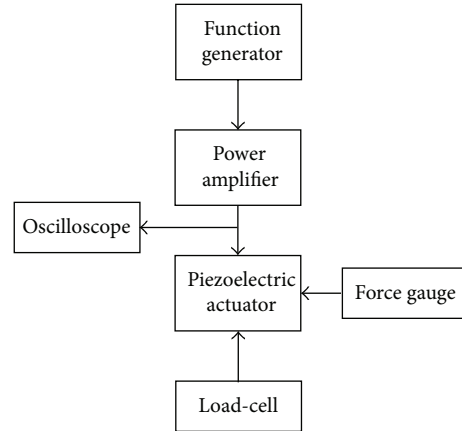


FIGURE 8: Setup of thrust measurement experiment.

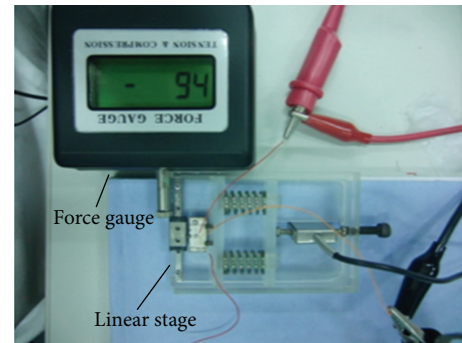


FIGURE 9: Thrust measurement experiment.

TABLE 4: Thrusts of piezoelectric actuator containing single pusher (preload of 215 g, drive voltage 30 Vpp).

Freq. (kHz)	Test 1 (g)	Test 2 (g)	Test 3 (g)	Test 4 (g)	Test 5 (g)	Ave. thrust (g)
217	60	62	69	63	57	62.2
218	64	68	72	73	70	69.4
219	54	57	60	52	55	55.6

TABLE 5: Thrusts of piezoelectric actuator containing double pushers (preload of 215 g, drive voltage 30 Vpp).

Freq. (kHz)	Test 1 (g)	Test 2 (g)	Test 3 (g)	Test 4 (g)	Test 5 (g)	Ave. thrust (g)
255	51	52	54	49	50	51.2
256	61	62	57	58	59	59.4
257	55	54	58	57	56	56.0

was carried out again with the preload of 430 g. The thrusts of the linear stage are shown in Table 6. The average thrust force is about 103 g as the operating frequency is 256 Hz which is better than the thrust force of piezoelectric actuator containing one single pusher. From the above experimental

TABLE 6: Thrusts of piezoelectric actuator containing double pushers (preload of 430 g, drive voltage 30 Vpp).

Freq. (kHz)	Test 1 (g)	Test 2 (g)	Test 3 (g)	Test 4 (g)	Test 5 (g)	Ave. thrust (g)
255	100	105	95	94	98	98.4
256	98	99	109	103	106	103.0
257	90	95	98	97	95	95.0

results, it is found that the piezoelectric actuator containing double pushers can provide a larger thrust as the preload is greater.

4. Conclusions

This study presents a novel piezoelectric actuator. The double pushers on the piezoelectric actuator are designed to enhance the thrust output. In the design process, Taguchi method is used to find the optimal combination of parameters including length, width, height, and electrodes setting. The contribution of each design factor of piezoelectric actuator is also discussed in this paper. Furthermore, a novel piezoelectric actuator containing double pushers according to the optimal design factors is produced and used in a linear stage. Some thrust tests are also carried out in this study. From the experiment results, the piezoelectric actuator containing double pushers can provide a greater thrust force than that of traditional actuators containing a single pusher as the preload is greater. Compared with the traditional actuators, the thrust force of new actuator can be increased by 48% with the double preload.

Conflict of Interests

The authors declare that there is no conflict of interests regarding the publication of this paper.

Acknowledgment

The authors would like to thank National Science Council (NSC) for their financial supports to the project (Grant no. NSC 101-2221-E-224-009).

References

- [1] K. Uchino, "Piezoelectric actuators 2006: expansion from IT/robotics to ecological/energy applications," *Journal of Electroceramics*, vol. 20, no. 3-4, pp. 301-311, 2008.
- [2] O. Vyshnevskyy, S. Kovalev, and W. Wischnewskiy, "A novel, single-mode piezoceramic plate actuator for ultrasonic linear motors," *IEEE Transactions on Ultrasonics, Ferroelectrics, and Frequency Control*, vol. 52, no. 11, pp. 2047-2053, 2005.
- [3] K. Otokawa, K. Takemura, and T. Maeno, "A multi-degree-of-freedom ultrasonic motor using single-phase-driven vibrators," in *Proceedings of the IEEE IRS/RSJ International Conference on Intelligent Robots and Systems (IROS '05)*, pp. 499-504, August 2005.
- [4] S.-B. Lee, T. S. Key, Z. Liang et al., "Microstructure design of lead-free piezoelectric ceramics," *Journal of the European Ceramic Society*, vol. 33, pp. 313-326, 2013.
- [5] S. C. Shen, P. C. Tsai, Y.-J. Wang, and H. J. Huang, "A new type of multi-degree-of-freedom miniaturization actuator using symmetric piezoelectric pusher element for a pocket sun-tracking system," *Sensors and Actuator A*, vol. 182, pp. 114-121, 2012.
- [6] T. Takano, Y. Tomikawa, M. Aoyagi, T. Ogasawara, and A. Yabuki, "Ultrasonic linear motors for application to driving a light pick-up element," in *Proceedings of the IEEE Ultrasonics Symposium*, pp. 445-448, November 1993.
- [7] W.-H. Lee, C.-Y. Kang, D.-S. Paik, B.-K. Ju, and S.-J. Yoon, "Butterfly-shaped ultra slim piezoelectric ultrasonic linear motor," *Sensors and Actuators A*, vol. 168, no. 1, pp. 127-130, 2011.
- [8] S. T. Ho, "Characteristics of the linear ultrasonic motor using an elliptical shape stator," *Japanese Journal of Applied Physics*, vol. 45, no. 7, pp. 6011-6013, 2006.
- [9] C. Lu, T. Xie, T. Zhou, and Y. Chen, "Study of a new type linear ultrasonic motor with double-driving feet," *Ultrasonics*, vol. 44, pp. e585-e589, 2006.
- [10] M. Aoyagi, Y. Tomikawa, and T. Takano, "Ultrasonic motors using longitudinal and bending multimode vibrators with mode coupling by externally additional asymmetry or internal nonlinearity," *Japanese Journal of Applied Physics*, vol. 31, no. 9, pp. 3077-3080, 1992.
- [11] J. Friend, A. Umeshima, T. Ishii, K. Naktaro, and S. Ueha, "A piezoelectric linear actuator formed from a multitude of bimorphs," *Sensors and Actuators A*, vol. 109, no. 3, pp. 242-251, 2004.
- [12] S.-W. Hsiao and M.-C. Tsai, "Design of a novel piezoelectric vibrator driven by asymmetrical electric fields for linear ultrasonic motors," *Journal of the Chinese Society of Mechanical Engineers*, vol. 32, no. 2, pp. 111-117, 2011.
- [13] H.-L. Lee, S.-J. Chang, S.-J. Hwang, F. Su, and S. K. Chen, "Computer-aided design of a TSOP II LOC package using Taguchi's parameter design method to optimize mold-flow balance," *ASME Journal of Electronic Packaging*, vol. 125, no. 2, pp. 268-275, 2003.

Research Article

The Creep Parameters of SAC305 Unleaded Solders

Chao-Ming Hsu,¹ Ah-Der Lin,² and Jao-Hwa Kuang³

¹ Department of Mechanical Engineering, National Kaohsiung University of Applied Sciences, Kaohsiung 80778, Taiwan

² Department of Mechanical Engineering, Cheng Shiu University, Kaohsiung 83347, Taiwan

³ Department of Mechanical and Electromechanical Engineering, National Sun Yat-sen University, Kaohsiung 80424, Taiwan

Correspondence should be addressed to Jao-Hwa Kuang; kuang@mail.nsysu.edu.tw

Received 14 September 2013; Accepted 16 October 2013

Academic Editor: Shoou-Jinn Chang

Copyright © 2013 Chao-Ming Hsu et al. This is an open access article distributed under the Creative Commons Attribution License, which permits unrestricted use, distribution, and reproduction in any medium, provided the original work is properly cited.

The tensile and shear loading creep parameters of unleaded Sn/3.0Ag/0.5Cu solders are extracted from the proposed tensile and shear creep tests in this work. Four creep loading temperatures, that is, 120°, 135°, 150°, and 165°C, are employed to extract the corresponding parameters. The creep parameters for tensile and shear loading models, that is, stress exponent, material constant, and activation energy, are curve-fitted by using the least square error and simplex optimization algorithms. The accuracy of the extracted parameters correlated with the measured strain rate versus temperature curves. Results indicate that the proposed measurement setup and extraction algorithm is feasible to extract the tensile and shear type creep parameters with good accuracy.

1. Introduction

The unleaded Sn/3.0Ag/0.5Cu solders have been used widely in electronic and photonic device packaging. The high operation temperature and on-off thermal cycling introduced in the electronic and photonic devices may introduce the serve thermal creep deformation. The creep deformation may lead to fiber alignment shifts in the transceiver module connectors and reduce the signal efficiency dramatically in the optical communication system. Damage to the encapsulation of electronic components may also be caused by thermal mechanical fatigue (TMF) at the welding point due to creep of the intermetallic compound. Various electronic component materials have different mechanical and thermal properties. Correspondingly, the creep deformation introduced from various temperature distributions may facilitate a redistribution of the stress status around a weld, which may eventually lead to a fatigue failure. A number of studies have investigated thermal stress to make predictions for the time-span of thermal fatigue at the welding areas of components under various thermal cycle loads.

Damage to electronic encapsulations occurs frequently near the solder joint due to thermal fatigue and creep. Creep only occurs when an object is subjected to high temperatures

for a prolonged period of time, and creep deformation is generally induced mainly by two factors: temperature and stress. Developing a creep model for electronic encapsulation materials is a very important issue. This study proposed two creep experiments, that is, the tensile and the shear loading creep tests, to derive the corresponding creep equations. Different loading temperatures are applied to initiate the creep for different Sn/3.0Ag/0.5Cu solder specimens.

From 1990 to 2002, Lau et al. [1–7] published a number of papers to consolidate the temperature change correlations associated with electronic packaging materials and explored the relationships between the materials and the stress/strain. Morris Jr. et al. [8] discussed the properties of melting point of two alloys, tin-beryllium (Sn-Bi) and tin-lead (60 Sn/40 Pb), used in electronic packaging engineering. Yang et al. [9–11] found that the eutectic microstructure of Sn/3.5Ag solder balls works better in laser reflow welding than in the infrared reflow process. Vianco [12–16] studied the stress-strain and creep effects in various tin-ball materials, including tin-lead (Sn63/Pb37), tin-silver-beryllium (Sn-Ag-Bi), and tin-silver-copper-antimony (Sn-Ag-Cu-Sb), used in encapsulation. Recently, the unleaded solder materials have been of interest for all electronic device manufacturers. The unleaded Sn/3.0Ag/0.5Cu solder is the most popular one.

2. Creep Experiments on Sn/3.0Ag/0.5Cu Solder Material

Creep deformation and its induced strain and strain rate are tested with a constant loading temperature. The loading temperature is higher than one half of the melting temperature of the specimen material. As noted in many textbooks, the creep deformation can be divided in three stages. In the first stage, that is, the primary creep stage, the more active dislocation sources in the material continue their activities, but they will gradually be blocked thus gradually reducing the strain rate. In the second stage, that is, the secondary creep stage, the strain hardening and recovery achieve equilibrium, so that the strain rate is maintained at a constant value; the minimum creep rate is reached at this stage. In the third stage, that is, the so-called tertiary creep stage [17], necking, voids, or cracks appear and the material is weakened by overaging and high temperature oxidation, thus increasing the strain rate. The creep rate increases with temperature and stress.

In this study two specimens of Sn/3.0Ag/0.5Cu solder material are used to test the creep phenomena in tensile and shear loading conditions. Four loading temperatures have been applied to measure the elongation variation with a constant load. The corresponding strain and strain rate variations have also been derived.

2.1. Creep Model. As noted [17], the creep strain (ε) in the material is dominated by the loading stress (σ), stress time (t), and temperature (T); that is,

$$\varepsilon = \varepsilon(\sigma, T, t). \quad (1)$$

For simplicity, the interaction between these parameters is ignored.

The Norton power law has been used widely to describe the secondary stage creep deformation. In this study, the Norton model has also been employed to describe the secondary stage creep phenomena as the specimen subjected to a tensile or shear type loading. The tensile and shear type creep models are

$$\dot{\varepsilon} = A\sigma^n e^{-Q/RT}, \quad (2)$$

$$\dot{\gamma} = B\tau^m e^{-Q/RT}, \quad (3)$$

where A and B are the material constant, σ is the average normal stress (MPa), τ is the average shear stress (MPa), Q is the activation energy (J/mol), R is the gas constant ($8.3 \text{ mol}^{-1} \text{ K}^{-1}$), T is the absolute temperature (K), and n and m are the stress exponent under tensile and shear loads, respectively.

Taking the logarithm on both sides of (2), it leads to a linear relation between the $\ln \dot{\varepsilon}$ and $\ln \sigma$ for a constant loading temperature:

$$\ln \dot{\varepsilon} = \left(\ln A - \frac{Q}{RT} \right) + n \ln \sigma. \quad (4)$$

Similarly, the shear strain rate can be derived as

$$\ln \dot{\gamma} = \left(\ln B - \frac{Q}{RT} \right) + m \ln \tau. \quad (5)$$

In the equations, A and B are temperature functions:

$$\begin{aligned} A &= \alpha + \beta e^{\omega T}, \\ B &= \kappa + \zeta e^{\delta T}, \end{aligned} \quad (6)$$

where $(\alpha, \beta, \omega, \text{ and } n)$ and $(\kappa, \zeta, \delta, \text{ and } m)$ are creep parameter sets of the tensile and shear models, respectively. Q and R are the activation energy and gas constant of the solder. From (4) and (5), it is observed that the logarithm $\ln \dot{\varepsilon}$ (or $\ln \dot{\gamma}$) of strain rate assumes a linear relationship with the logarithm value of average stress $\ln \sigma$ (or $\ln \tau$). The constant slopes of $\ln \dot{\varepsilon}$ versus $\ln \sigma$ and $\ln \dot{\gamma}$ versus $\ln \tau$ are the respective stress exponents n , and m . The natural logarithm of strain rate ($\ln \dot{\varepsilon}, \ln \dot{\gamma}$) is proportional to the reciprocal of loading temperature ($1/T$) [18]. Therefore, the activation energy parameter Q can then be derived from the relationship between the natural logarithm of the strain rate and the reciprocal of the temperature.

Based on the extraction algorithm mentioned in the previous section, the values of creep parameters $\alpha, \beta, \omega, \kappa, \zeta, \delta, n, m$, and Q can be extracted from the measured strain rate and loading stress by employing the simplex optimization method in this work.

2.2. Creep Experiment Setup and Specimens. The tensile and shear creep specimens are illustrated in Figures 1(a) and 1(b). Two round copper solid bars are welded with the Sn/3.0Ag/0.5Cu solder between the orthogonal or parallel connecting surfaces. Figures 2(a) and 2(b) show the preparation and geometries of the specimens used in the tensile and shear creep tests. An appropriate amount of the Sn/3.0Ag/0.5Cu solder paste was placed at the middle section of two 5 mm in diameter copper rods. About 3-4 mm gap is designed for the Sn/3.0Ag/0.5Cu solder layer. These two copper rods were then, respectively, placed on a vertical clamp or a "V" shape bed, as shown in Figure 1(a) or Figure 1(b), respectively. A torch was then used to heat the area around the Sn/3.0Ag/0.5Cu solder paste until it was completely molten. Extra care was taken not to directly expose the solder paste to the flame. The dimensions of eight Sn/3.0Ag/0.5Cu solder specimens are listed in Table 1. The size parameters A, B, C , and D of eight solder specimens (specimens numbers 1a~8a) indicate the diameters of top, bottom, waist, and the height of the solder layer in the tensile specimens. Due to the surface tension introduced in the melting process, the waist diameter C in the tensile specimens always has the smallest value. The corresponding size parameters E, F , and G for the eight shear specimens (specimens numbers 1b~8b) values, respectively, indicate the length, width, and height of the solidified solder paste. Two constant loads, that is, 7.35 and 29.4 N, are applied for the tensile and shear creep tests, and four loading temperatures, that is, 120, 135, 150, and 165°C (393, 408, 423, and 438 K), are measured in this study. Since the melting temperature of the copper is much higher than that of the Sn/3.0Ag/0.5Cu solder, the creep deformation of the copper bar can be ignored in these measurements. In other words, the measured end

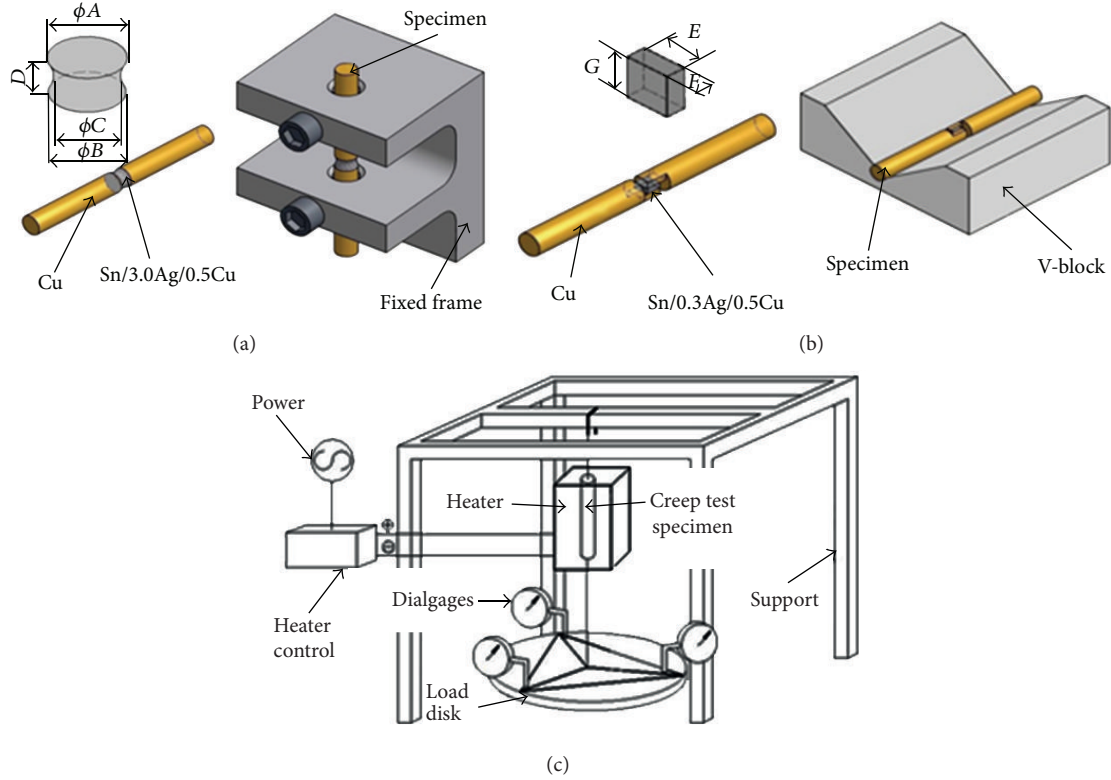


FIGURE 1: Creep experiment setup and specimens arrangement: (a) tensile creep specimen, (b) shear creep specimen, and (c) creep experiment setup.

TABLE 1: Creep specimen parameters.

Specimens no.	Load (N)	Temp. (K)	Dimensions of Specimens (mm)						
			A	B	C	D	E	F	G
1a, 1b	7.35	393	4.4	4.2	3.7	4.0	1.6	0.7	4.7
2a, 2b		405	3.9	4.0	2.9	4.0	2.2	0.6	4.7
3a, 3b		423	4.0	3.8	3.0	3.6	1.8	0.6	4.0
4a, 4b		438	4.8	4.5	2.7	3.8	1.4	0.6	4.4
5a, 5b	29.4	393	3.8	3.8	3.2	3.4	1.8	0.8	2.2
6a, 6b		405	4.4	3.9	3.5	3.2	1.8	0.7	2.6
7a, 7b		423	4.8	4.6	3.6	3.2	2.2	0.8	2.2
8a, 8b		438	4.8	4.4	3.6	3.4	2.1	0.8	2.4

displacements are considered to be introduced from the creep deformation of the solder layer.

Figure 2(c) is the scheme of the creep test setup. The specimens are arranged in a temperature controlled box and loaded vertically with a constant disc weight. Three displacement sensors are located at three measured points. The measured elongation variation in the loading direction is recorded periodically. The corresponding true stress, strain, and strain rate are calculated simultaneously.

3. Experimental Results and Creep Parameters Extraction

Two sets of creep specimens, that is, eight specimens for the tensile creep test and the other eight specimens for the shear creep test, are measured with two constant loads (7.53

and 29.4 N) and four loading temperatures (393, 408, 423, and 438 K). Since the specimens' sizes are not identical, each specimen has a different sectional dimension. The corresponding loading stress should also be different; therefore, the experiment was expected to record a set of primary data with different values for stress, temperature, and time-shift. To compensate the possible displacement measurement error, the vertical displacements d_A , d_B , and d_C measured at disk rim as shown in Figure 3 are averaged. The vertical displacement of the specimens is averaged as

$$d = \frac{(d_A + d_B + d_C)}{3}. \quad (7)$$

3.1. Tensile Creep Experiment. Figure 4 shows the variation of displacement of tensile specimens subjected to the loads

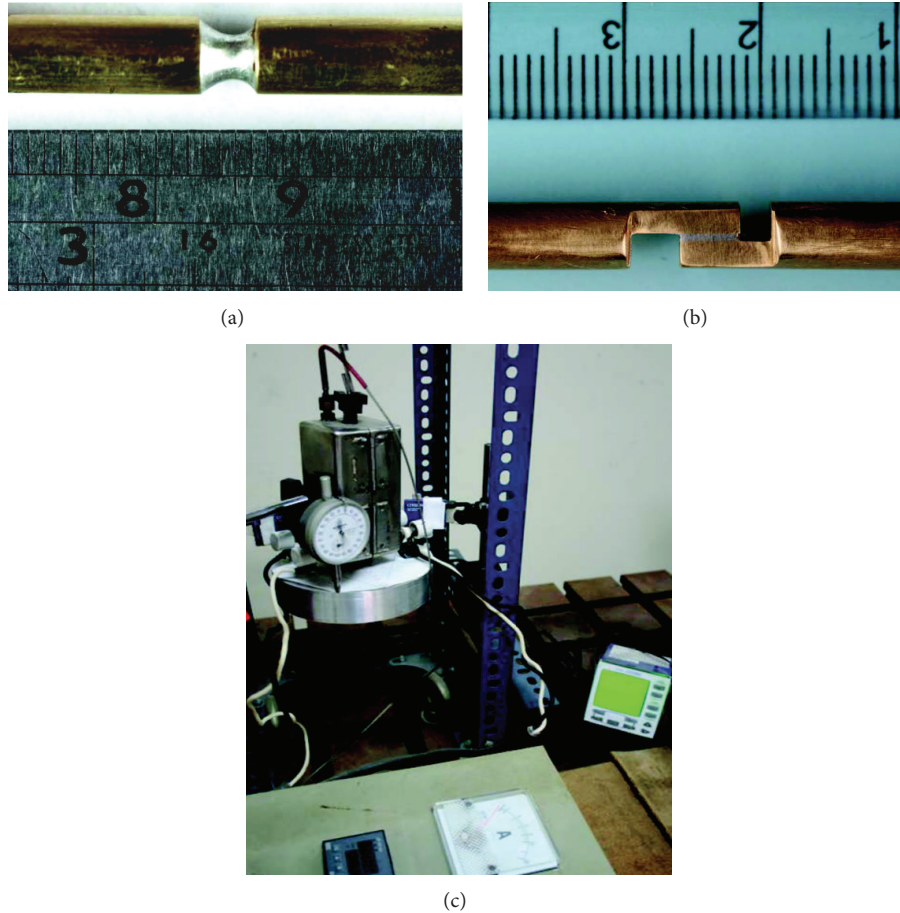


FIGURE 2: Creep experiment specimen and equipment: (a) tensile creep experiment specimen, (b) shear creep experiment specimen, and (c) creep experiment equipment.

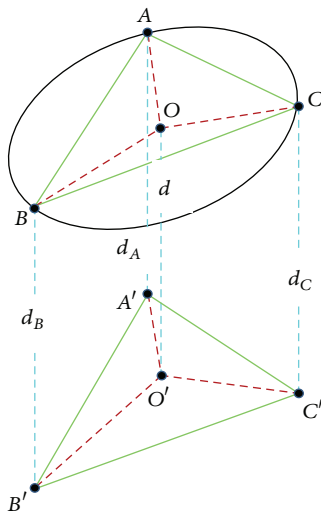


FIGURE 3: Measuring displacement.

of 7.35 and 29.4 N. For the case of specimens subjected to a load of 7.35 N with a loading temperature 438 K as shown in Figure 4, the specimens took about 0.45 hour to go through

the primary creep stage. The two levels of loadings are chosen to make sure that the tested specimens can reach the state of secondary creep. For example, the normal stress induced in the specimens with a 29.4 N loading is 26.8 MPa, which is about 60% of the yielding strength of the tested solder. The end of tested specimens was measured to have a displacement of 0.02 mm in this period. The measured results for the same specimens reveal a secondary creep stage from loading time 0.45 to 20.83 hours. The extension displacement increases from 0.2 mm to 0.024 mm with an almost constant speed. The third stage creep occurred after 20.83 hours. The measured results indicate that the creep deformation of the Sn/3.0Ag/0.5Cu solder is quite sensitive to the loading temperature. Figure 5 shows the corresponding variation curves of strain and strain rate of the tensile specimens with a loading condition of 7.35 N and 438 K during the creep test. An average strain rate of 7.95×10^{-7} 1/sec was measured for the specimens in the secondary creep stage. Table 2 lists the measured average strain rates $\dot{\epsilon}$ of these eight measured tensile specimens, that is, tensile specimens numbers 1(a) to 8(a), in this work.

Equation (4) reveals that the creep parameter of activation energy Q can be derived from the slope of algorithm value $(\ln \dot{\epsilon})$ and $(1/T)$ diagram. Results in Figure 6 show the

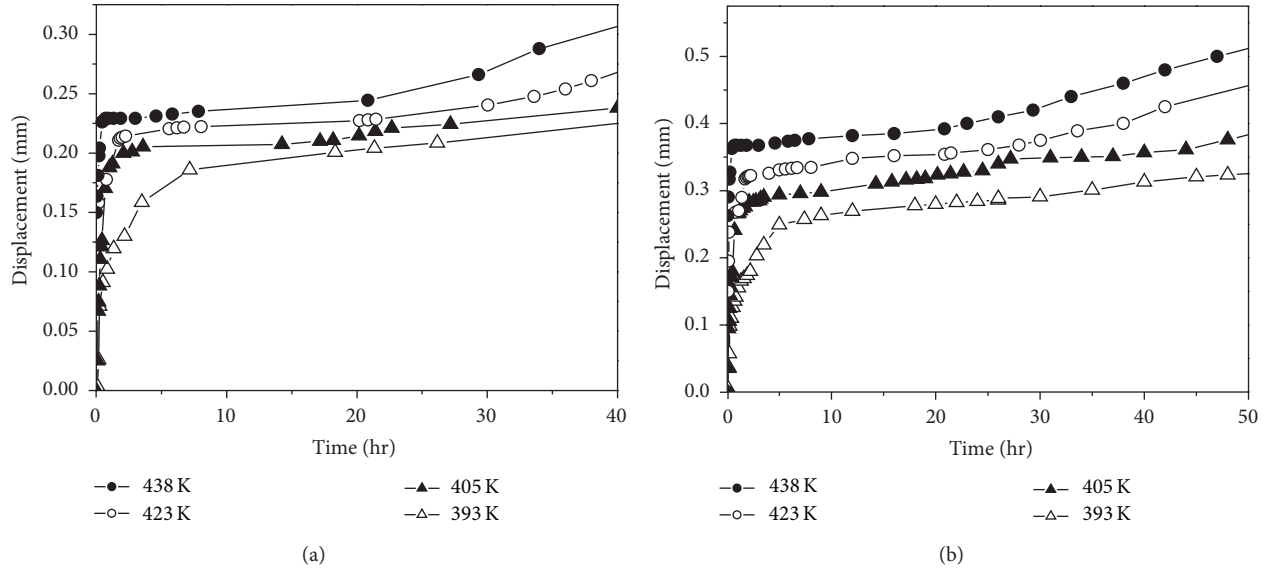


FIGURE 4: Correlation of displacement-time in the tensile creep experiment under different loads: (a) 7.35 N load disc and (b) 29.4 N load disc.

TABLE 2: Results of tensile creep specimen experiment.

No.	Load (N)	Temp. (K)	Average stress (MPa)	Strain rate ($\times 10^{-6}$ 1/sec)
1	7.35	393	0.669	0.0854
2		405	1.145	0.336
3		423	1.076	0.506
4		438	1.266	0.795
5	29.4	393	3.657	1.28
6		405	3.057	2.10
7		423	2.890	3.87
8		438	3.057	6.12

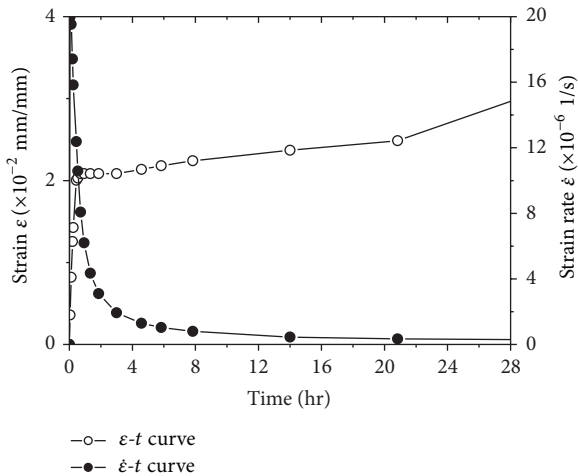


FIGURE 5: Correlation of strain-time and strain rate in the tensile creep experiment under a temperature of 438 K and a load of 7.34 N.

correlation between $\ln \dot{\epsilon}$ and $1/T$ of tested specimens under the loads of 7.35 N and 29.4 N. Based on Norton power law, that is, (4), the slope value is equal to $-Q/R$. By applying

the least square error method, the linear slope values of measured specimens under loads of 7.35 N and 29.4 N can be derived as -8318.02 and -7257.00 , respectively. The average value -7737.51 of these two slopes and an activation energy value 64221.32 (J/mol) can be derived with the gas constant ($8.3 \text{ mol}^{-1} \text{ K}^{-1}$).

Figure 7 shows the correlation between the logarithm strain rate ($\ln \dot{\epsilon}$) and the logarithm stress ($\ln \sigma$) in the tensile creep experiment. The four left points and the four right points in this figure are related to the measured data for the load of 7.35 N and 29.4 N, respectively. Therefore, four linear equations can be derived for these tensile specimens to describe the power law relation between the strain rate and average stress with different loading temperatures. They are

$$\ln \dot{\epsilon} = 1.59 (\ln \sigma) - 14.94 \quad \text{when } T = 393 \text{ K,}$$

$$\ln \dot{\epsilon} = 1.87 (\ln \sigma) - 14.46 \quad \text{when } T = 408 \text{ K,}$$

$$\ln \dot{\epsilon} = 2.06 (\ln \sigma) - 13.95 \quad \text{when } T = 423 \text{ K,}$$

$$\ln \dot{\epsilon} = 2.30 (\ln \sigma) - 13.59 \quad \text{when } T = 438 \text{ K.}$$

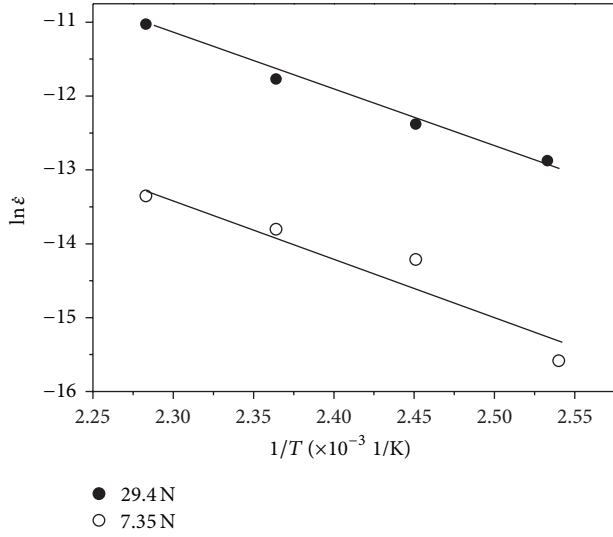


FIGURE 6: Natural logarithm of the tensile creep experiment strain rate and reciprocal to temperature.

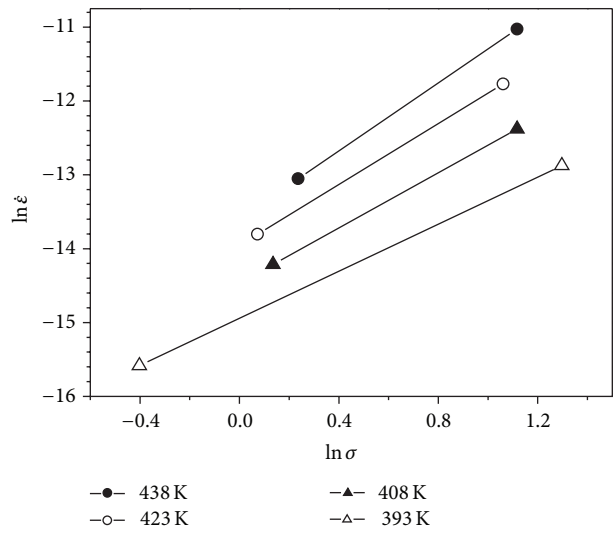


FIGURE 7: The correlation between logarithm strain rate and logarithm stress.

Initially, an average slope value of n (1.954) is approximated from these four equations by ignoring its loading temperature effect. Similarly, a constant value of -14.22 is approximated by averaging the four constant values in (8). Then an approximated initial trial power relation for these tensile specimens is proposed; that is,

$$\ln \dot{\epsilon} = 1.954 \ln \sigma - 14.22. \quad (9)$$

From (4) and (9) and the approximated activation energy value 64221.32 (J/mol) mentioned previously, the relationship between the material constant A and temperature can be derived in Figure 8. By using the least square error method and the definition of material constant A in (6), the set of parameters in the tensile creep equation can be derived as $\alpha = 15.40$, $\beta = 6.39 \times 10^{11}$, and $\omega = (-1/18.04)$.

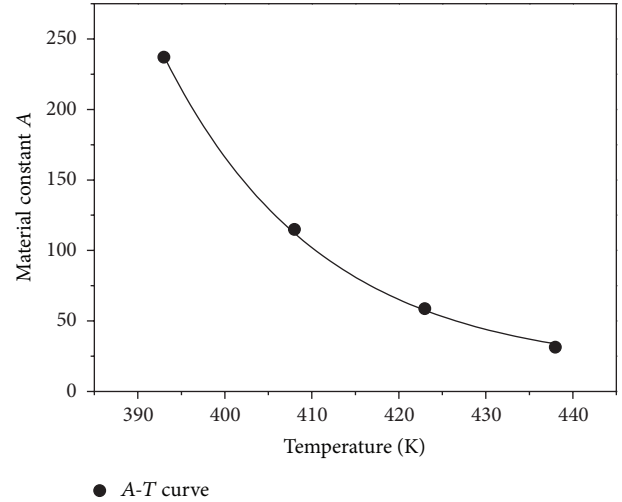


FIGURE 8: Correlation between tensile creep material constant and temperature.

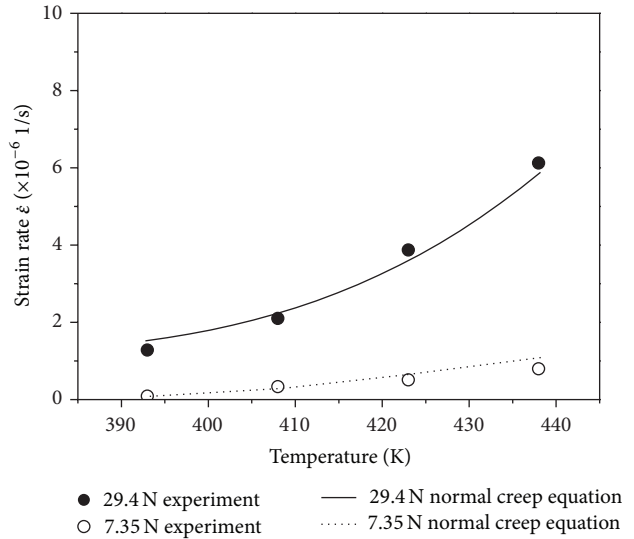


FIGURE 9: Correlation between strain rate and temperature in the tensile creep equation.

To improve the accuracy of these extracted parameters, the simplex optimization algorithm has been employed in this study to minimize the difference between measured strain rate and the strain rate data estimated from the initial trial parameters. All the extracted creep parameters mentioned previously are considered as the initial trial parameters in the optimization process. In the optimization procedure the following is assumed:

$$\text{strain rate: } \dot{\epsilon} = (Q, n, \alpha, \beta, \omega),$$

$$\text{least square error: } \Delta^2 = \sum_{i=1}^8 (\hat{\epsilon}_i - \hat{\epsilon}_{ie})^2, \quad (10)$$

$$\text{object function: } \min. (\Delta^2),$$

Δ : deviation between the estimated and experimental values,

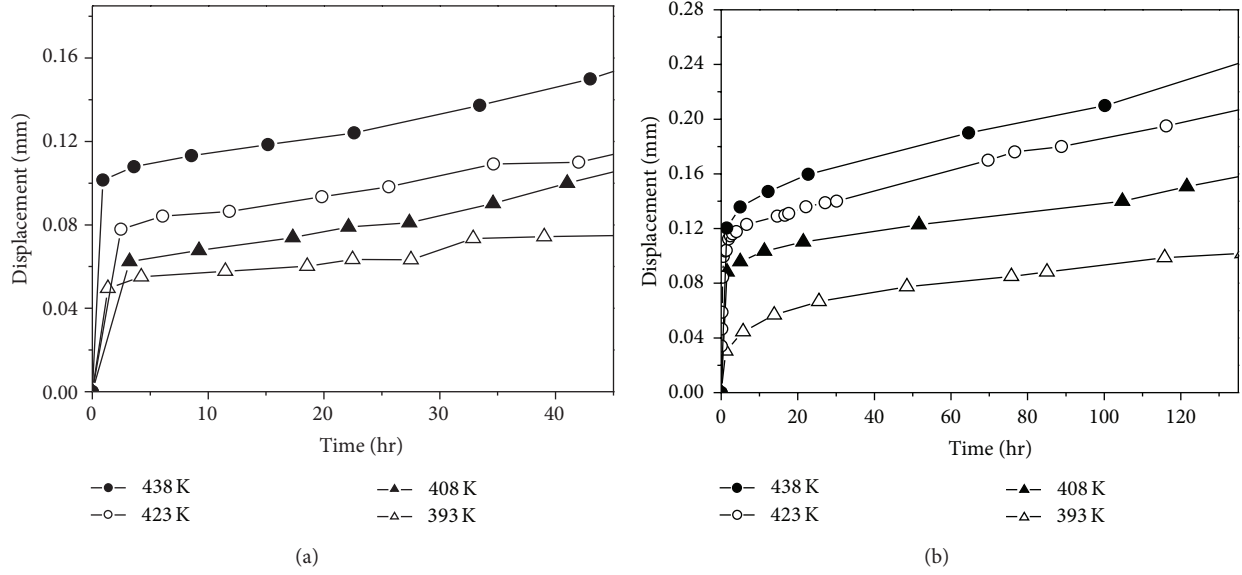


FIGURE 10: Correlation of displacement-time in the shear creep experiment under different loads: (a) 7.35 N load disc and (b) 29.4 N load disc.

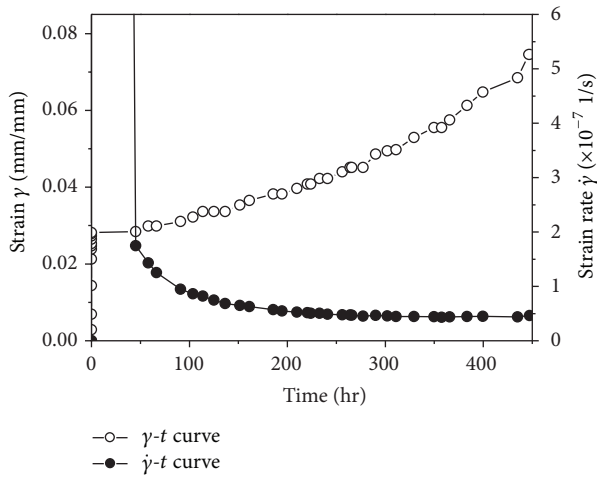


FIGURE 11: Correlation between strain-time and strain rate under a temperature of 408 K and a load of 7.35 N in the shear creep experiment.

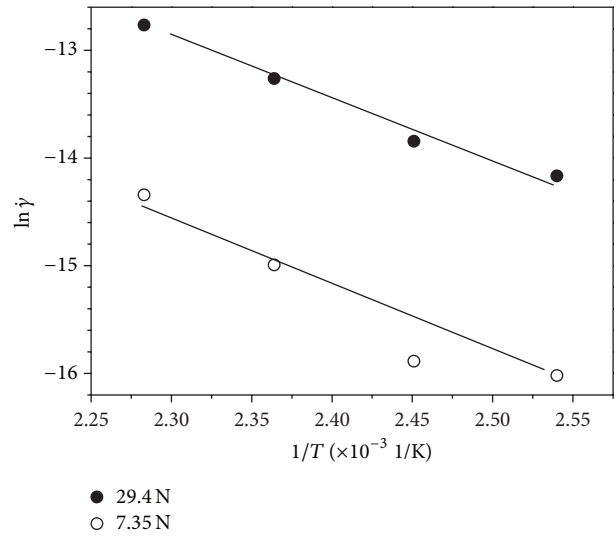


FIGURE 12: Correlation between the natural logarithm of the strain rate and the reciprocal of temperature in the shear creep experiment.

$\dot{\epsilon}_i$: estimated tensile strain rate,
 $\dot{\epsilon}_{ie}$: measured tensile strain rate,
 initial trial point:

$$\begin{aligned} Q &= 64221.32, & n &= 1.954, \\ \alpha &= 15.40, & \beta &= 6.39 \times 10^{11}, \\ \omega &= \left(-\frac{1}{18.04}\right). \end{aligned} \quad (11)$$

The tensile creep parameters, that is, n, Q, α, β , and ω , for the Sn/3.0Ag/0.5Cu solder specimens converged from the simplex optimization method are $n = 1.8640$, $Q = 52154.52$, $\alpha = 1.2507$, $\beta = 6.3131 \times 10^{11}$, and $\omega = (-1/8.19)$. Based

on the proposed algorithm and the measured creep data, the tensile creep equation for the Sn/3.0Ag/0.5Cu solder can be derived as

$$\begin{aligned} \dot{\epsilon} &= \left[1.25074 + 6.3131 \times 10^{11} \times e^{-T/8.19}\right] \\ &\times \sigma^{1.864} e^{-52154.52/RT}. \end{aligned} \quad (12)$$

A comparison between the temperature and estimated strain rate results for the specimens 1(a) to 8(a) reveals a difference between 0.19% and 43.6% for the specimens with a loading of 7.35 N and a difference between 2.1% and 17.3% for the specimens with a loading of 29.4 N as shown in Figure 9.

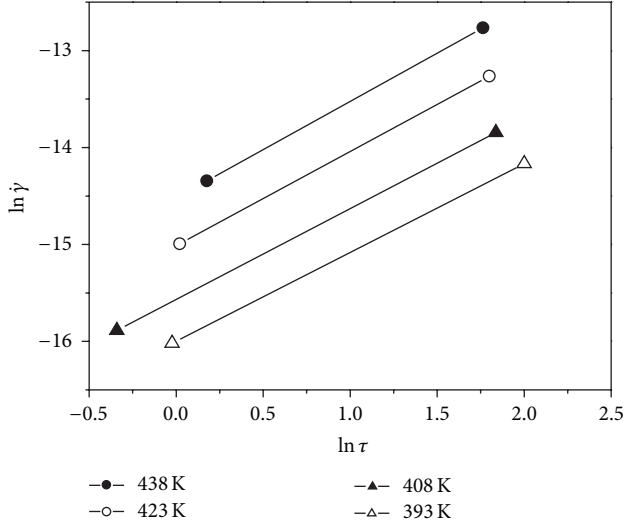


FIGURE 13: The correlation between the logarithm of strain rate and average stress for the shear creep test.

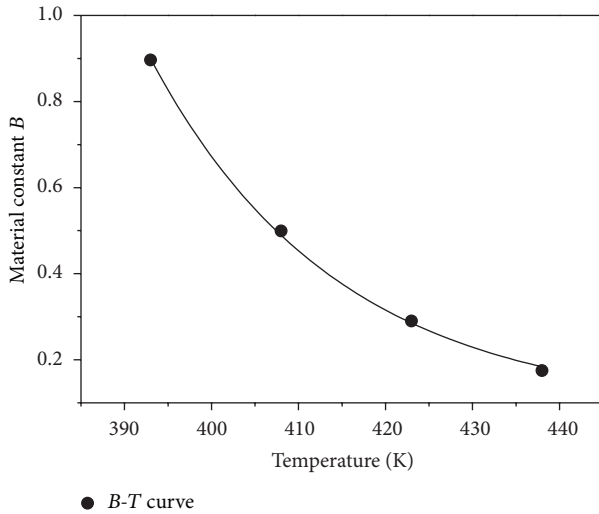


FIGURE 14: Correlation between shear creep material constant and temperature.

3.2. Shear Creep Experiment. Figure 10 shows the measured results of the shear creep specimens under the same creep loading condition as mentioned in the previous tensile test. For the specimens subjected to a load of 29.4 N with a loading temperature of 438 K, the secondary creep stage occurs between 4.95 and 194 hours, and the creep extension of the shear specimens increases from 0.136 mm to 0.285 mm. Figure 11 shows the variation of corresponding strain and strain rate with respect to loading time. The final secondary creep strain rate at the second stage is approximately 6.29×10^{-8} 1/sec. The recorded results of specimens 1(b) to 8(b) in the shear creep tests are listed in Table 3. Similarly, the correlation between $\ln \dot{\gamma}$ and $1/T$ under loads of 7.35 N and 29.4 N is shown in Figure 12. From the slope values the $-Q/R$ values can be derived as -6879.823 and -5569.58 .

TABLE 3: Results of the shear creep specimen experiment.

No.	Load (N)	Temp. (K)	Average stress (MPa)	Strain rate ($\times 10^{-6}$ 1/sec)
1		393	0.977	0.0550
2	7.35	405	0.711	0.0629
3		423	1.021	0.154
4		438	1.193	0.295
5		393	7.424	0.352
6	29.4	405	6.282	0.485
7		423	6.074	0.869
8		438	5.833	1.43

And the average value is -6224.68 . Just by following the calculation used in the tensile test, an activation energy value of 51664.84 (J/mol) is derived.

Figure 13 shows the correlation between the strain rate in the shear creep tests and the average shear stress. Four linear equations can be derived for the shear creep test results. They are

$$\begin{aligned}
 \ln \dot{\gamma} &= 0.92 \ln \tau - 16.00 & \text{when } T &= 393 \text{ K,} \\
 \ln \dot{\gamma} &= 0.94 \ln \tau - 15.57 & \text{when } T &= 408 \text{ K,} \\
 \ln \dot{\gamma} &= 0.97 \ln \tau - 15.01 & \text{when } T &= 423 \text{ K,} \\
 \ln \dot{\gamma} &= 0.99 \ln \tau - 14.52 & \text{when } T &= 438 \text{ K.}
 \end{aligned} \tag{13}$$

Figure 14 shows the correlation between shear creep material constant and temperature. Following the process mentioned in the tensile creep test, the creep parameters in the shear creep equation can be approximated as $K = 0.084$, $\zeta = 7.27$, and $\delta = (-1/21.47)$. All these approximated parameter values are considered as the initial trial values in the simplex optimization process to minimize the difference between the measured and estimated shear strain rates. The following is assumed:

$$\begin{aligned}
 \dot{\gamma} &= \dot{\gamma}(Q, m, K, \zeta, \delta), \\
 \Delta^2 &= \sum_{i=1}^8 (\dot{\gamma}_i - \dot{\gamma}_{ic})^2,
 \end{aligned} \tag{14}$$

object function: $\min. (\Delta^2)$,

$\dot{\gamma}_i$: estimated shear strain rate,

$\dot{\gamma}_{ic}$: shear strain rate from the experimental results.

A set of parameters is generated from the simplex optimization method; they are $m = 0.9515$, $Q = 58494.91$, $K = 2.3705$, $\zeta = 2.4639 \times 10^9$, and $\delta = (-1/17.99)$. Therefore, the following shear creep equation for the Sn/3.0Ag/0.5Cu solder can be derived:

$$\begin{aligned}
 \dot{\gamma} &= \left[2.3705 + 2.4639 \times 10^9 \times e^{-T/17.99} \right] \\
 &\times \tau^{0.9515} e^{-58494.91/RT}.
 \end{aligned} \tag{15}$$

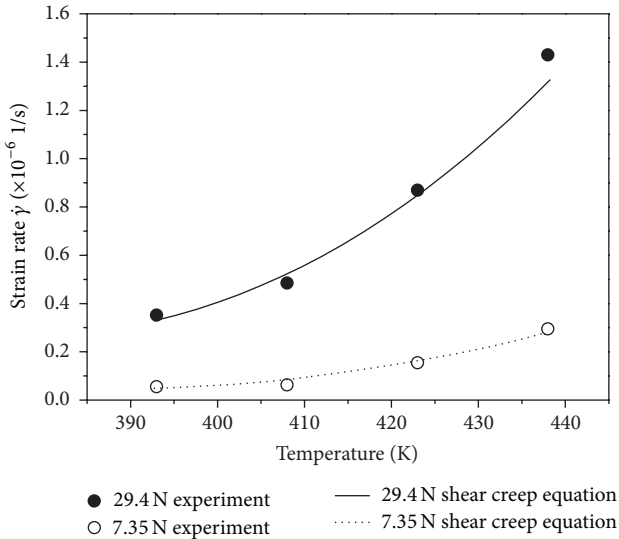


FIGURE 15: Correlation between shear creep equations strain rate and temperature.

From a comparison between the experimental and the estimated strain rates for the shear creep specimens, that is, 1(b) to 8(b), a difference between 0.43 and 8.1% is found for the specimens with a load of 7.35 N as shown in Figure 15. A difference between 1 and 6% has been found for the specimens with a load of 29.4 N.

4. Conclusions

The solder joint reliability is strongly affected by creep. This was validated by both simulation and experimental results, which show significantly higher occurrence of thermal failures of solder joints in high temperature aging tests. The high operation temperature induced creep phenomenon is the major cause of solder joint failure. Therefore, the reliability of solder packages under high operation temperature is highly dependent on solder joint creep property. The tensile and shear creep models of lead-free Sn/3.0Ag/0.5Cu solder material have been proposed in this study. Simplified tensile and shear tests can be used as a quick way of modeling the lead-free solder. Due to the diversity of the measured data, an optimization algorithm is proposed to extract the creep parameters in these creep equations. Experimental measurements and estimated strain rate results reveal that the proposed creep equations can provide reasonable accuracy.

The processes of extracting the creep parameters are specifically presented for illustrating the versatility of creep equation formulation. This result is useful for packaging reliable lead-free solder jointed assembly of high power laser or LED module packages. A wide variety of other applications of this proposed lead-free Sn/3.0Ag/0.5Cu solder creep model are expected.

Conflict of Interests

The authors declare that there is no conflict of interests regarding the publication of this paper.

References

- [1] J. H. Lau and C. G. Harkins, "Stiffness of 'gull-wing' leads and solder joints for a plastic quad flat pack," *IEEE Transactions on Components, Hybrids, and Manufacturing Technology*, vol. 13, no. 1, pp. 124–130, 1990.
- [2] J. H. Lau, *Thermal Stress and Strain in Microelectronics Packaging*, Van Nostrand Reinhold, New York, NY, USA, 1993.
- [3] J. H. Lau, S. H. Pan, and C. Chang, "Creep analysis of solder bumped direct chip attach (DCA) on microvia build-up printed circuit board with underfill," in *Proceedings of the International Symposium on Electronic Materials and Packaging (EMAP '00)*, pp. 127–135, 2000.
- [4] J. H. L. Pang and D. Y. R. Chong, "Flip chip on board solder joint reliability analysis using 2-D and 3-D FEA models," *IEEE Transactions on Advanced Packaging*, vol. 24, no. 4, pp. 499–506, 2001.
- [5] J. Lau, Z. Mei, S. Pang, C. Amsden, J. Rayner, and S. Pan, "Creep analysis and thermal-fatigue life prediction of the lead-free solder sealing ring of a photonic switch," *Journal of Electronic Packaging*, vol. 124, no. 4, pp. 403–410, 2002.
- [6] J. H. Lau, S. W. R. Lee, S. H. Pan, and C. Chang, "Nonlinear-time-dependent analysis of micro via-in-pad substrates for solder bumped flip chip applications," *Journal of Electronic Packaging*, vol. 124, no. 3, pp. 205–211, 2002.
- [7] J. H. Lau and S.-W. R. Lee, "Modeling and analysis of 96.5Sn-3.5Ag lead-free solder joints of wafer level chip scale package on buildup microvia printed circuit board," *IEEE Transactions on Electronics Packaging Manufacturing*, vol. 25, no. 1, pp. 51–58, 2002.
- [8] J. W. Morris Jr., J. L. F. Goldstein, and Z. Mei, "Microstructure and mechanical properties of Sn-In and Sn-Bi solders," *JOM*, vol. 45, no. 7, pp. 25–27, 1993.
- [9] W. Yang, R. W. Messler Jr., and L. E. Felton, "Microstructure evolution of eutectic Sn-Ag solder joints," *Journal of Electronic Materials*, vol. 23, no. 8, pp. 765–772, 1994.
- [10] W. Yang, L. E. Felton, and R. W. Messler Jr., "The effect of soldering process variables on the microstructure and mechanical properties of eutectic Sn-Ag/Cu solder joints," *Journal of Electronic Materials*, vol. 24, no. 10, pp. 1465–1472, 1995.
- [11] H. Yang, P. Deane, P. Magill, and K. L. Murty, "Creep deformation of 96.5Sn-3.5Ag solder joints in a flip chip package," in *Proceedings of the 46th IEEE Electronic Components & Technology Conference (ECTC '96)*, pp. 1136–1142, Orlando, Fla, USA, May 1996.
- [12] A. M. Jackson, I. Artaki, and P. T. Vianco, "Manufacturing feasibility of several lead-free solders for electronic assembly," in *Proceedings of the 7th International SAMPE Electronics Conference*, pp. 381–393, Parsippany, NJ, USA, June 1994.
- [13] P. T. Vianco, J. A. Rejent, and J. J. Martin, "The compression stress-strain behavior of Sn-Ag-Cu solder," *JOM*, vol. 55, no. 6, pp. 50–55, 2003.
- [14] P. T. Vianco, J. A. Rejent, and P. F. Hlava, "Solid-state intermetallic compound layer growth between copper and 95.5Sn-3.9Ag-0.6Cu solder," *Journal of Electronic Materials*, vol. 33, no. 9, pp. 991–1004, 2004.
- [15] P. T. Vianco, J. A. Rejent, and A. C. Kilgo, "Creep behavior of the ternary 95.5Sn-3.9Ag-0.6Cu solder—part I: as-cast condition," *Journal of Electronic Materials*, vol. 33, no. 11, pp. 1389–1400, 2004.
- [16] E. P. Lopez, P. T. Vianco, and J. A. Rejent, "Solderability testing of Sn-Ag-XCu Pb-free solders on copper and Au-Ni-Plated Kovar

substrates,” *Journal of Electronic Materials*, vol. 34, no. 3, pp. 299–310, 2005.

- [17] M. T. Shen and T. Mao, *Laser diode module residual stress and creep effect [Ph.D. dissertation]*, Graduate Institute of Mechanical Engineering, National Sun Yat-Sen University, 2000.
- [18] F. Gao, H. Nishikawa, T. Takemoto, and J. Qu, “Temperature dependence of mechanical properties of individual phases in Sn-3.0Ag-0.5Cu lead-free solder alloy,” in *Proceedings of the 58th Electronic Components and Technology Conference (ECTC '08)*, pp. 466–471, Miami, Fla, USA, May 2008.

Research Article

An Experimental Study on Heat Conduction and Thermal Contact Resistance for the AlN Flake

Huann-Ming Chou, Jin-Chi Wang, and Yuh-Ping Chang

Department of Mechanical Engineering, Kun Shan University, Tainan 710, Taiwan

Correspondence should be addressed to Jin-Chi Wang; markfish@mail.ksu.edu.tw

Received 24 August 2013; Accepted 17 October 2013

Academic Editor: Teen-Hang Meen

Copyright © 2013 Huann-Ming Chou et al. This is an open access article distributed under the Creative Commons Attribution License, which permits unrestricted use, distribution, and reproduction in any medium, provided the original work is properly cited.

The electrical technology has been a fast development over the past decades. Moreover, the tendency of microelements and dense division multiplex is significantly for the electrical industries. Therefore, the high thermal conductible and electrical insulating device will be popular and important. It is well known that AlN still maintains stability in the high temperature. This is quite attractive for the research and development department. Moreover, the thermal conduct coefficient of AlN is several times larger than the others. Therefore, it has been thought to play an important role for the radiator of heat source in the future. Therefore, this paper is focused on the studies of heat conduction and thermal contact resistance between the AlN flake and the copper specimens. The heating temperatures and the contact pressures were selected as the experimental parameters. According to the experimental results, the materials are soft and the real contact areas between the interfaces significantly increase under higher temperatures. As a result, the thermal contact resistance significantly decreases and the heat transfer rate increases with increasing the heating temperature or the contact pressures.

1. Introduction

The electrical technology has been a fast development during the first decade of the 21st century. Moreover, the tendency of microelements and dense division multiplex is significantly attractive for the research and development department. To achieve the above goals, the high heat dissipative and electrical insulating device will be popular and important in the future.

It is well known that AlN still maintains stability under the high temperature conditions. Moreover, the thermal conduct coefficient of AlN material is several times larger than the other nonmetallic solids [1–3]. Hence, it is widely used for the heat dissipation. Besides, AlN film has good electrical insulating properties to avoid the risk of a short circuit of electronic components [4–7]. These advantages are quite attractive for the research and development department of the electrical corporations [8].

The method of using continuous variations of triboelectrification and friction coefficient to monitor the dynamic tribological properties between the metal films has been

applied successfully by the authors [9–12]. The related results also showed that the thermal contact resistance of the metal films is significantly influenced by the real contact areas between the interfaces. Moreover, the major factors for the real contact areas are the normal loads and the surface hardness of the materials. On the other hand, the defects of the material crystal always play an important role for the heat transfer of AlN [1–7]. Therefore, the relationships between the microstructures of AlN film and the efficiency of the heat transfer are the key points. Based on the above statements, this paper is focused on the studies of heat conduction and thermal contact resistance between the AlN flake and the copper specimen by referring the previous studies of thermal contact resistance between the metal films.

2. Experimental Apparatus and Procedures

2.1. Experimental Apparatus. The schematic diagram of thermal contact resistance tester with measuring system is shown in Figure 1. The voltage signals from each measurement point of the thermocouples were transferred to the temperature

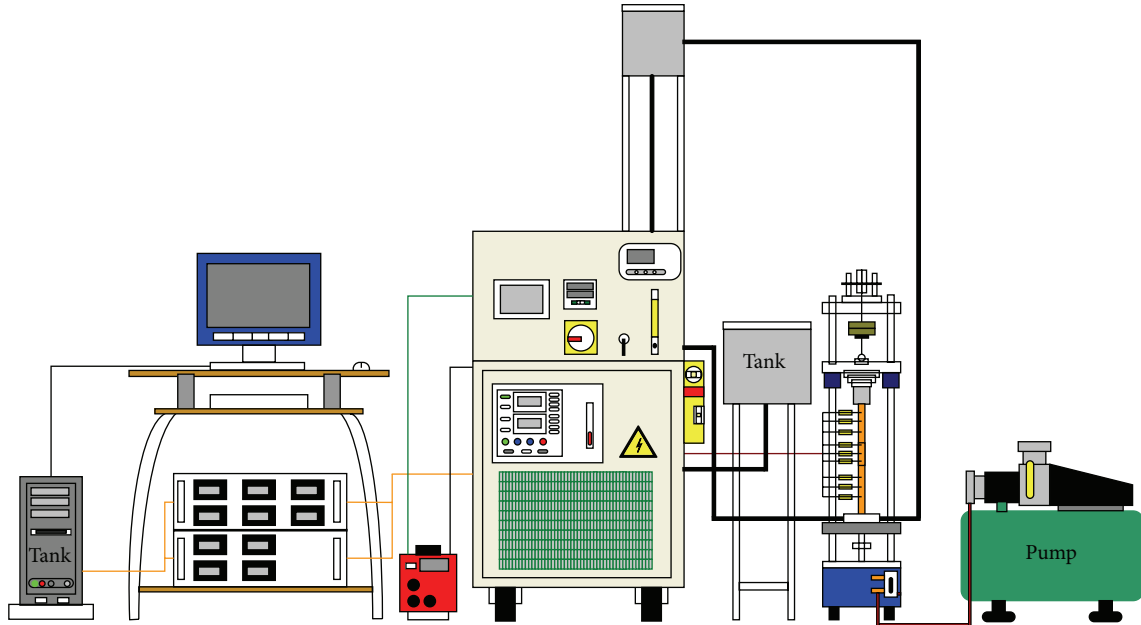


FIGURE 1: The schematic diagram of thermal contact resistance tester with measuring system.

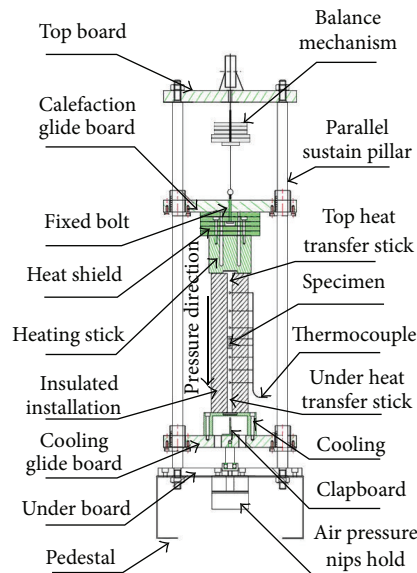


FIGURE 2: The main parts of the experimental apparatus.

extractor. There are ten thermocouples in the systems. The temperatures at the measuring point can be obtained by the calibration. Then, the thermal contact resistance and the heat transfer rate can be obtained by the three mathematical formulas as shown in Section 2.3.

Figure 2 shows the main parts of the experimental apparatus. The loading systems contain the following: one-way pneumatic valve manual control, with a model DJA25N75 pneumatic cylinder, and IHP air compressor.

The main heat transfer gateway is made of copper: heat transfer stick ($\Phi 20 \text{ mm} \times 110 \text{ mm}$, drilling $\Phi 1.4 \text{ mm} \times \text{deep } 10 \text{ mm}$) $\times 2$; copper substrate ($\Phi 20 \text{ mm} \times 20 \text{ mm}$, drilling $\Phi 1.4 \text{ mm} \times \text{deep } 10 \text{ mm}$) $\times 1$.

The insulation equipment is made of ceramic glass fiber cotton ($k = 0.036 \text{ W/m}^\circ\text{C}$). The heating equipment includes the three heating rods (CIR-2034/240 V). Several counterweights (1 kgw $\times 3$, 5 kgw $\times 2$, and 10 kgw $\times 1$) are used for maintaining the equilibrium of the contact pressure. Moreover, the water circulating pump and the ice water maker are disposed for the temperature control.

2.2. Test Specimens. AlN thin flakes were used as the main experimental specimens. Material properties are shown in Table 1. The thickness of AlN slices is only 0.7 mm. The size and shape of the specimens are shown in Figure 3(a). AlN

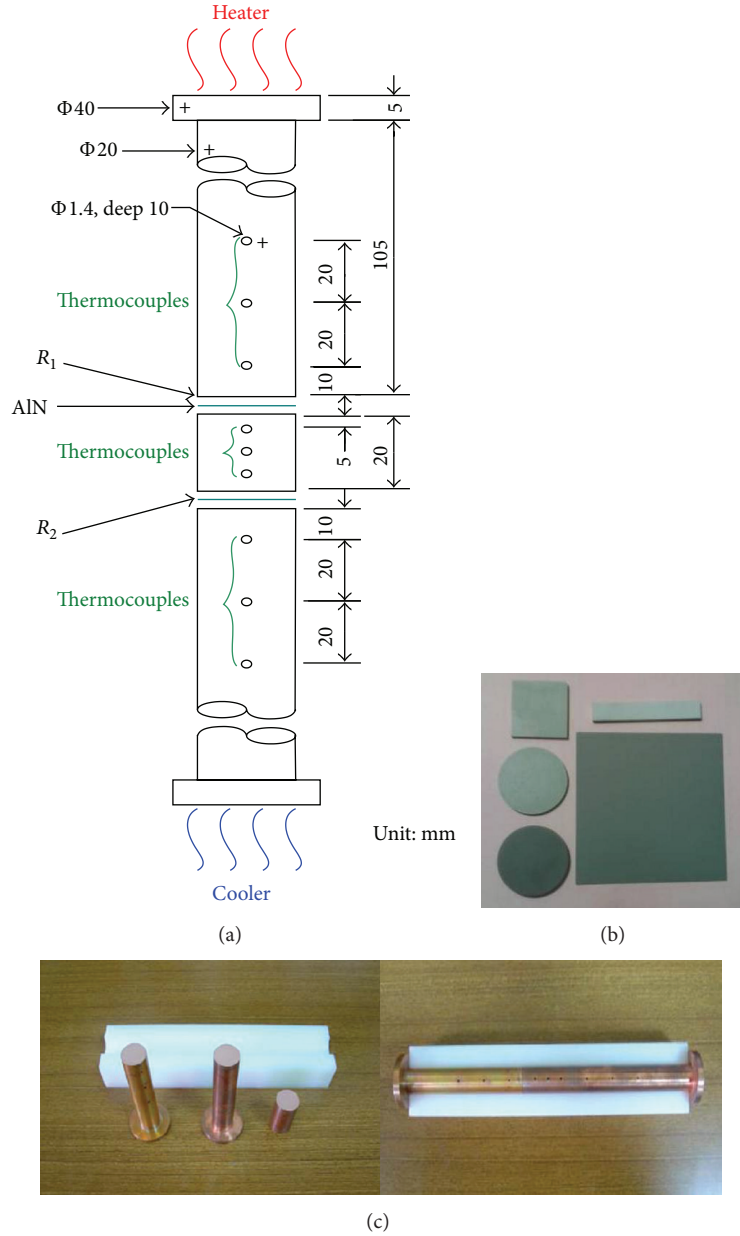


FIGURE 3: (a) The size and shape of the specimens, (b) AlN flake, and (c) copper specimen and heat transfer rod.

TABLE 1: Material properties of AlN.

	AlN
Melting point ($^{\circ}\text{C}$)	2200
Crystal structure	hcp
Density (g/cm^3)	3.26
Specific heat (25°C , J/kgK)	730
Thermal expansion coefficient ($25\text{--}400^{\circ}\text{C}$, 10^{-6}K^{-1})	4.4
Thermal conductivity ($\text{W}/\text{m}^{\circ}\text{C}$)	140–180

slices, and copper specimen, and the heat transfer rod are shown in Figures 3(b) and 3(c).

2.3. *Experimental Procedures.* There are two types of thermal contact resistance in this study. The upper measuring point of the heat transfer rod is R_1 and the lower is R_2 . Several parameters influence R_1 and R_2 , such as temperature, pressure, material, and surface roughness. Therefore, it is necessary to clarify and calculate them step by step.

The formula of the heat transfer (q) is

$$q = -kA \frac{dT}{dx} = \frac{T_a - T_b}{R_c}. \quad (1)$$

The formula of the thermal contact resistance (R) is

$$R_1 = \frac{T_{a1} - T_{a2}}{q}, \quad R_2 = \frac{T_{b1} - T_{b2}}{q}. \quad (2)$$

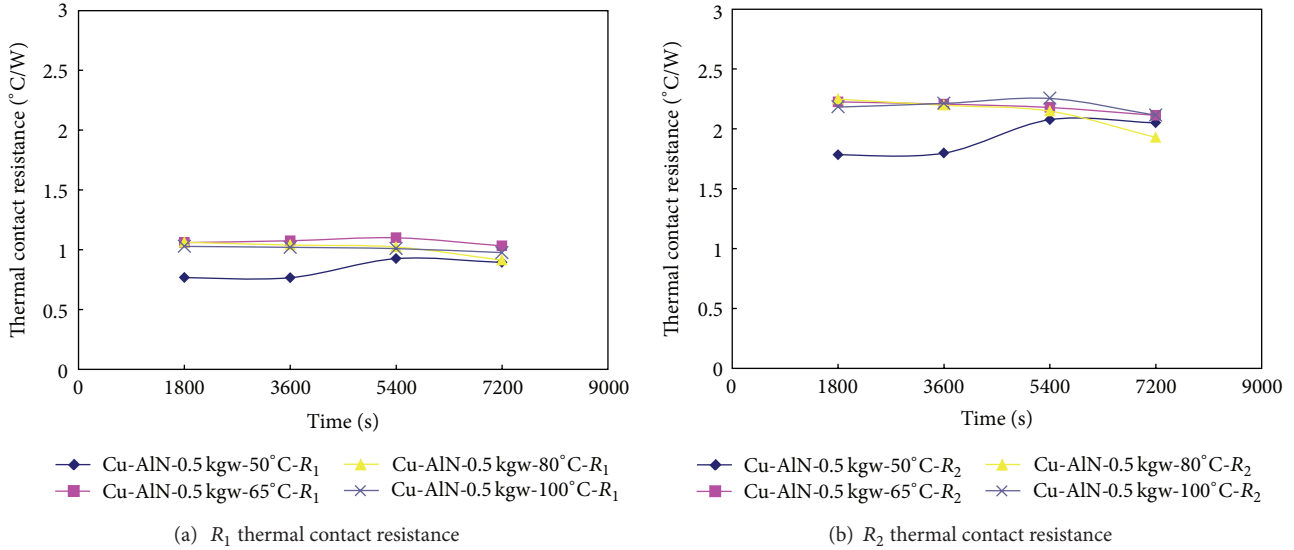


FIGURE 4: Effects of the heating temperature on the thermal contact resistance for Cu/AlN/Cu under 0.5 kgw (16 kPa). (a) R_1 and (b) R_2 .

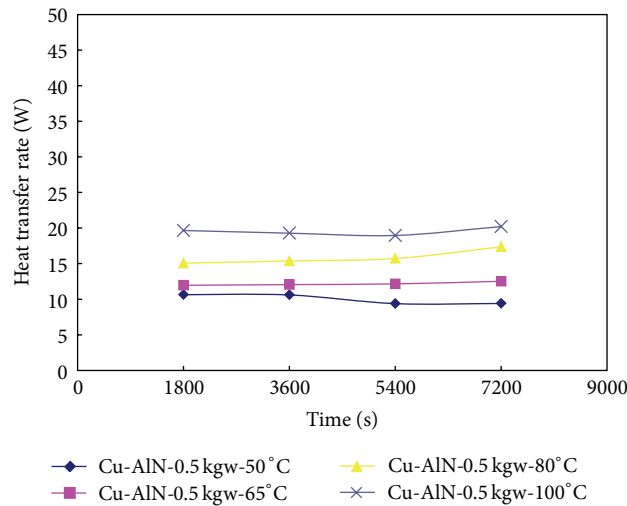


FIGURE 5: Effects of the heating temperature on the heat transfer rate for Cu/AlN/Cu under 0.5 kgw (16 kPa).

Moreover, the related temperatures are obtained by the following:

$$\frac{T_1 - T_2}{X_1 - X_2} = \frac{T_3 - T_4}{X_3 - X_4}. \quad (3)$$

The heating temperatures were set at 50°C, 65°C, 80°C, and 100°C. The temperature of the ice water circulating system was fixed at 10°C. Before each test, the preparatory time was set at 4 hours. The normal loads were set at 0.5 kgw and 1.5 kgw, and the corresponding contact pressures were 16 kPa and 48 kPa. The average room temperature for the test was $25 \pm 2^\circ\text{C}$, and the average relative humidity was $65 \pm 5\%$.

3. Results and Discussions

Figure 4 shows the effects of the heating temperature on the thermal contact resistance for Cu/AlN/Cu under 16 kPa. It

is seen from this figure that R_1 and R_2 are independent of the heating temperatures and the experimental time for the temperatures is larger than 50°C. R_1 maintains about 1°C/W and R_2 maintains about 2.2°C/W for the higher temperatures. Moreover, R_1 increases from 0.7°C/W to 0.91°C/W and R_2 increases from 1.8°C/W to 2.2°C/W with the experimental time for the heating temperature of 50°C.

The effects of the heating temperature on the heat transfer rate for Cu/AlN/Cu under 16 kPa are shown in Figure 5. It is seen from this figure that the heat transfer rate increases from 10 W to 19 W with increasing the heating temperature from 50°C to 100°C.

Figure 6 shows the effects of the heating temperature on the thermal contact resistance for Cu/AlN/Cu under 48 kPa. It is seen from Figure 6(a) that the increasing trends are similar to the cases of 16 kPa except 100°C. The thermal contact resistance especially decreases with the experimental

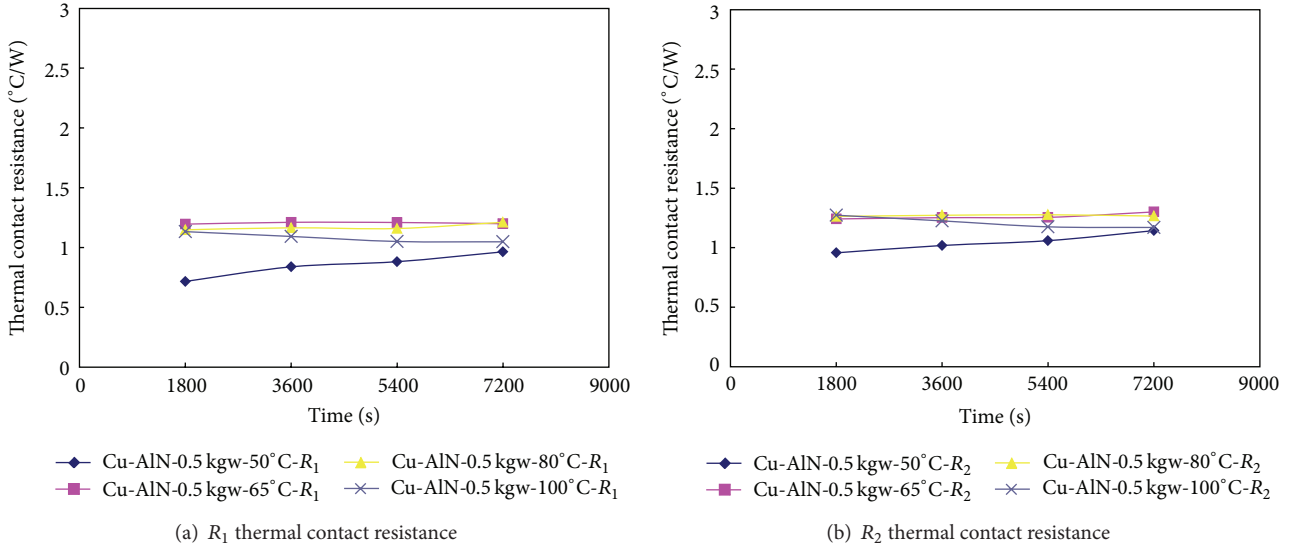


FIGURE 6: Effects of the heating temperature on the thermal contact resistance for Cu/AlN/Cu under 1.5 kgw (48 kPa). (a) R_1 and (b) R_2 .

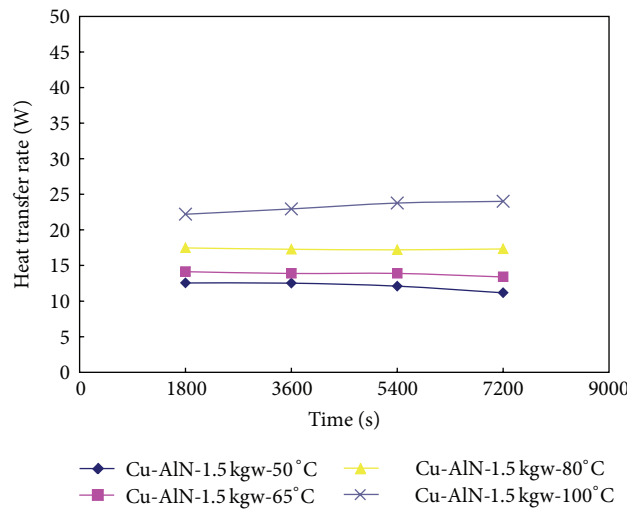


FIGURE 7: Effects of the heating temperature on the heat transfer rate for Cu/AlN/Cu under 1.5 kgw (48 kPa).

time under 100°C and 48 kPa. This indicates that the materials are soft under the higher temperatures. As a result, the real contact areas between the interfaces significantly increase. Hence, the thermal contact resistance significantly decreases.

The effects of the heating temperature on the heat transfer rate for Cu/AlN/Cu under 48 kPa are shown in Figure 7. It is seen from this figure that the heat transfer rate increases from 10 W to 17 W with increasing the heating temperature from 50°C to 80°C. Moreover, the heat transfer rate especially increases to 22~25 W under 100°C and 48 kPa.

Comparing to the cases of Cu/Cu, the thermal contact resistance doubles and the heat transfer rate increases 33% with AlN flake under 50°C and 16 kPa. When the heating temperature increases to 100°C, the thermal contact resistance decreases slightly and the heat transfer rate decreases about 40% with AlN flake.

According to the SEM of AlN-flake surface shown in Figure 8, they are rough and uneven. Moreover, the aspects are in the range of 1~10 μm . Hence, many gaps exist between the interfaces. That is, when the copper is soft under the higher temperatures and contact pressures, it will get into the gaps and the real contact areas between the interfaces significantly increase. Therefore, the thermal contact resistance especially decreases under the higher temperatures and contact pressures. The corresponding results can be observed in Figures 4 and 6.

4. Conclusions

The thermal contact resistance and the heat transfer rate between Cu/AlN/Cu were experimentally investigated in

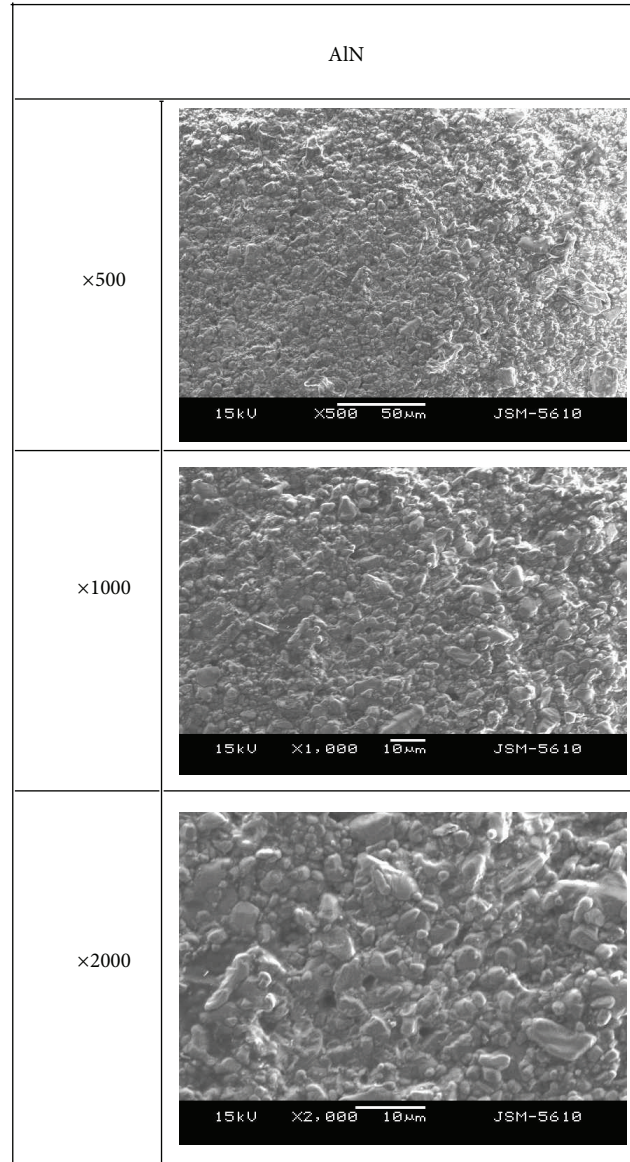


FIGURE 8: The SEM of the AlN-flake surface.

this study. From the experimental results, the following conclusions were drawn.

- (1) The materials are soft and the real contact areas between the interfaces significantly increase under the higher temperatures. As a result, the thermal contact resistance significantly decreases and the heat transfer rate increases with increasing the heating temperature.
- (2) The thermal contact resistance doubles and the heat transfer rate increases 33% with AlN flake under 50°C and 16 kPa. When the heating temperature increases to 100°C, the thermal contact resistance decreases slightly and the heat transfer rate decreases about 40%.

- (3) The thermal contact resistance significantly decreases and the heat transfer rate increases 4% with AlN flake under 100°C and 48 kPa.

Conflict of Interests

The authors declare that there is no conflict of interests regarding the publication of this paper.

Acknowledgment

The authors would like to express their appreciation to the National Science Council in Taiwan for their financial support under Grant nos. NSC 101-2221-E-168-014 and NSC 102-2622-E-150-002-CC2.

References

- [1] M. I. Nieto, R. Martínez, L. Mazerolles, and C. Baudín, "Improvement in the thermal shock resistance of alumina through the addition of submicron-sized aluminium nitride particles," *Journal of the European Ceramic Society*, vol. 24, no. 8, pp. 2293–2301, 2004.
- [2] J. H. Edgar and W. J. Meng, *Properties of Group III Nitrides*, 1993.
- [3] Y. Kurokawa, K. Utsumi, and H. Takamizawa, "Development and microstructural characterization of high-thermal-conductivity aluminum nitride ceramics," *Journal of the American Ceramic Society*, vol. 71, no. 7, pp. 588–594, 1988.
- [4] X. Xu, H. Wu, and Z. Jin, "Studies of the structure and surface roughness of AlN thin films," *Rare Metal Materials and Engineering*, vol. 29, no. 6, pp. 394–397, 2000.
- [5] B. Qiao, Z. Liu, and Y. Li, "Effect of technical parameters on deposition rate of AlN films prepared by magnetron reactive sputtering," *Journal of Northwestern Polytechnical University*, vol. 22, no. 22, pp. 260–263, 2004.
- [6] J. Zhang, W. Wang, X. H. Zeng, Y. Z. Shi, and H. Q. Fan, "Fabrication and dielectric property of polymer-matrix composites containing AlN particles for electronic substrates," *Journal of Aeronautical Materials*, vol. 26, no. 3, pp. 341–342, 2006.
- [7] Y. D. Wang, H. P. Zhou, L. Qiao, H. Chen, and H. B. Jin, "Thermal conductivity of AlN/PE composite substrate," *Journal of Inorganic Materials*, vol. 15, no. 6, pp. 1030–1036, 2000.
- [8] Y. C. Lin, *Processing parameters on the performance of aluminum nitride [M.S. thesis]*, Department of Mechanical Engineering, National Taiwan University of Science and Technology, 2005.
- [9] Y. P. Chang, "A novel method of using continuous tribo-electrification variations for monitoring the tribological properties between pure metal films," *Wear*, vol. 262, no. 3-4, pp. 411–423, 2007.
- [10] Y. P. Chang, H. M. Chou, R. F. Horng, and H. M. Chu, "Another method of using dynamic tribo-electrification mechanisms for measuring gas flowrate," *Proceedings of the Institution of Mechanical Engineers J*, vol. 221, no. 4, pp. 479–487, 2007.
- [11] Y. P. Chang, Y. C. Chiou, and R. T. Lee, "Tribo-electrification mechanisms for dissimilar metal pairs in dry severe wear process. Part I: effect of speed," *Wear*, vol. 264, no. 11-12, pp. 1085–1094, 2008.
- [12] Y. P. Chang, Y. C. Chiou, and R. T. Lee, "Tribo-electrification mechanisms for dissimilar metal pairs in dry severe wear process. Part II: effect of load," *Wear*, vol. 264, no. 11-12, pp. 1095–1104, 2008.

Research Article

Optical and Structural Properties of Titanium Dioxide Films from TiO_2 and Ti_3O_5 Starting Materials Annealed at Various Temperatures

Shih-Chang Shei

Department of Electrical Engineering, National University of Tainan, No. 33, Section 2, Shu-Lin Street, Tainan 70005, Taiwan

Correspondence should be addressed to Shih-Chang Shei; scshei@mail.nutn.edu.tw

Received 29 August 2013; Accepted 8 October 2013

Academic Editor: Shoou-Jinn Chang

Copyright © 2013 Shih-Chang Shei. This is an open access article distributed under the Creative Commons Attribution License, which permits unrestricted use, distribution, and reproduction in any medium, provided the original work is properly cited.

We investigated the optical and structural properties of titanium dioxide films deposited from Ti_3O_5 and TiO_2 starting materials by electron beam evaporation at annealing temperatures from 400°C to 800°C. We find that the refractive index of as-deposited films from Ti_3O_5 starting material is higher than that of as-deposited films from TiO_2 starting material. In addition, during thermal annealing, the refractive index fluctuates slightly as compared with TiO_2 films from TiO_2 starting material. This should be attributed to the fact that the deposited molecules had a higher packing density, such that the film was denser. The transmittance spectra of TiO_2 films from Ti_3O_5 starting material indicate that transmittance edge slightly shifts to longer wavelength with the annealing temperature increasing when compared with TiO_2 starting material, in which the transmittance spectra indicate that the transmittance edge strongly shifts to longer wavelength with the same annealing temperature increasing. These findings should be attributed to the absence of oxygen and scattering of rough surface.

1. Introduction

Titanium dioxide (TiO_2) film is extensively used as a high refractive index film material in optical coating. It is a perfect couple with SiO_2 which is commonly used as a low refractive index film material to make thin film multilayer dielectric coatings consisting of alternating layers of high and low refractive index materials [1–3]. Titanium dioxide films can be prepared by most reactive coating techniques such as evaporation, sol-gel, sputtering, and plasma-enhanced chemical vapor deposition. In the case of evaporation, preferably electron beam evaporation, which is one of the most traditional methods because of high efficiency and low cost, is extensively used in scientific researches as well as in practical production. When TiO_2 films are prepared from TiO_2 starting material with the electronic beam evaporation method, the film is loose with a refractive index 1.9, which is obviously lower than the refractive index of the bulk [4–6]. According to the literature, Duyar et al. reported that it is quite difficult to obtain films with reproducible and stable optical properties, in particular, for materials that exist in a

number of different stoichiometric forms of the system Ti-O. Whenever TiO , Ti_2O_3 , or TiO_2 is evaporated, the vapor may consist of various Ti-O combinations, which change as the evaporation continues. The refractive index of the deposited film, thus, is not constant because most Ti-O materials evaporate noncongruently. If, however, Ti_3O_5 is evaporated as starting composition, the only titanium species in the vapour is TiO , and the oxygen content in the vapour remains constant [7, 8]. Furthermore, the refractive index is higher than TiO_2 starting material due to the higher packing density [9]. Many researchers have reported the deposition of TiO_2 films from Ti_3O_5 starting material by electron beam evaporation. However, TiO_2 films are loosely packed which is caused by low molecular mobility. It indicates that the refractive index is lower than the bulk [9, 10]. Therefore, it is necessary for annealing to increase molecular mobility and make them more bulk-like. During annealing, thermal energy provides the mobility of the molecules, so the loose film becomes slimmer and increases the refractive index as the temperature increases. Many papers have reported that TiO_2 films from Ti_3O_5 starting material were annealed at rather low

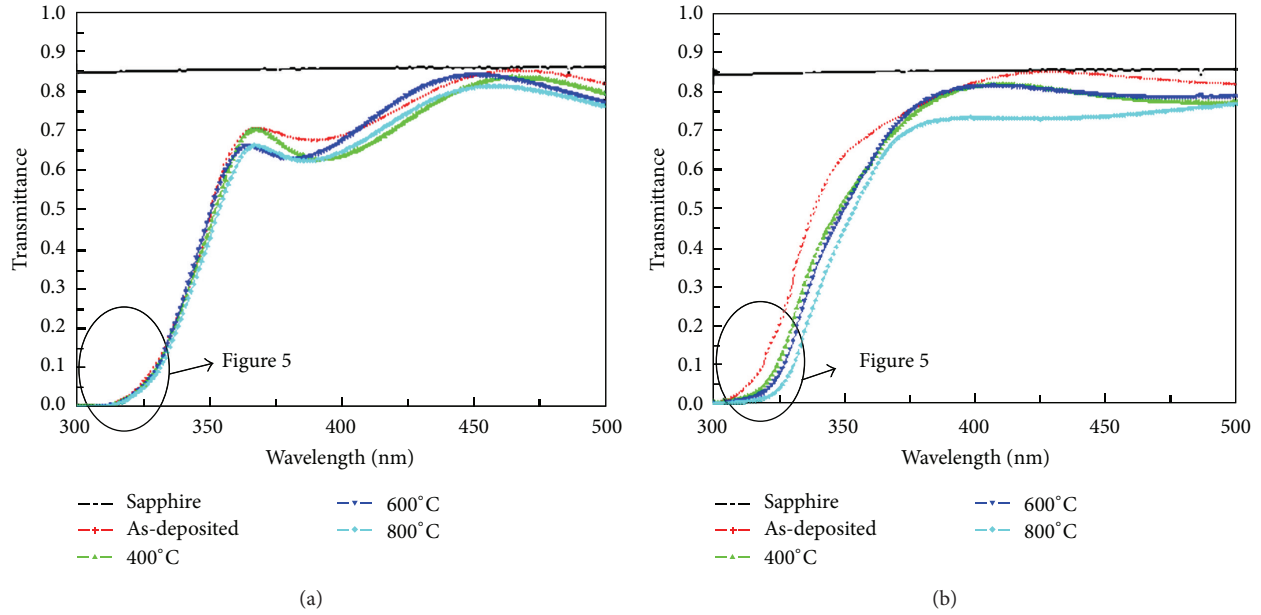


FIGURE 1: Transmittance spectra obtained from (a) Ti_3O_5 and (b) TiO_2 starting materials at various thermal annealing temperatures.

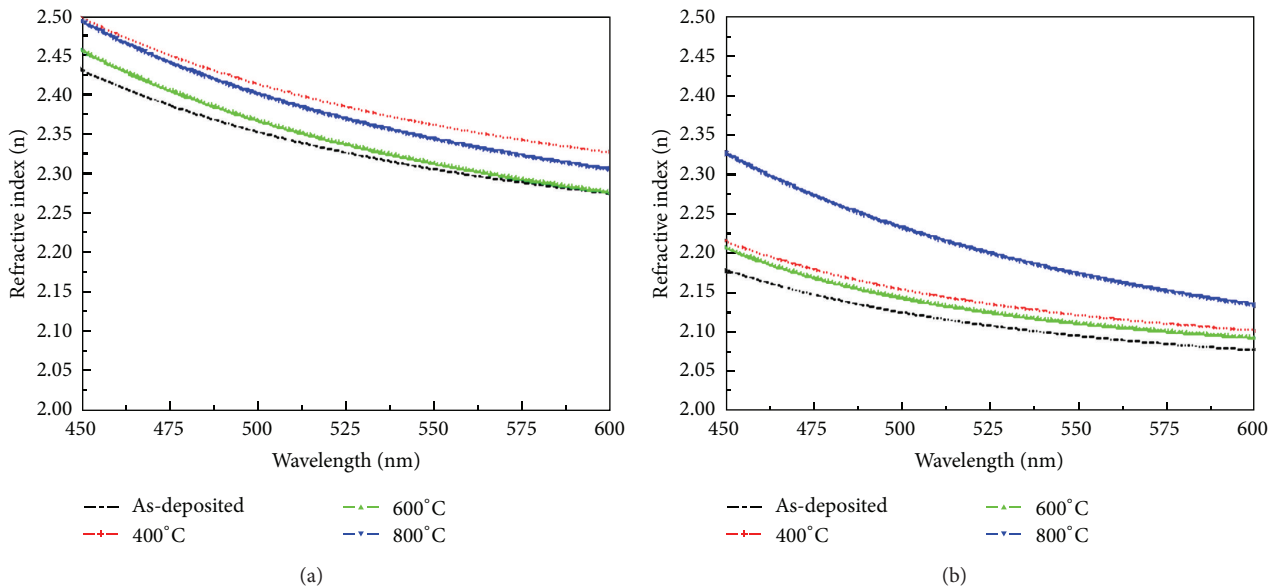


FIGURE 2: Refractive index obtained from (a) Ti_3O_5 and (b) TiO_2 starting materials at various thermal annealing temperatures.

temperature [11–13]. For example, Chen et al. reported that TiO_2 films were deposited from Ti_3O_5 starting material by ion-assisted deposition. The refractive index increased with the substrate temperature from 150°C to 250°C ; they thought that the deposited molecules had greater surface mobility, so the film was denser, with a higher refractive index. They also found that the refractive index with the substrate temperature of 150°C increased from 100°C to 200°C during annealing and declined as the annealing temperature decreased from 200°C to 300°C . Such a variation was caused by the loss of oxygen below 200°C during annealing and by the capture of oxygen as the temperature was increased above 200°C . Therefore,

some suboxides (TiO_x) were separated from titanium oxide and oxidized during annealing. These findings revealed that the film was too loose to have a large surface area, which made it lose and capture oxygen easily at a substrate temperature of 150°C [12]. Jaing et al. reported that TiO_2 films were deposited from Ti_3O_5 starting material by ion-assisted deposition. They showed that the refractive index fluctuated irregularly with the annealing temperature below 350°C . However, the refractive index increased with the annealing temperature from 350°C to 450°C ; they thought that the film became denser as the annealing temperature increased above 350°C because the refractive index showed the densification of the

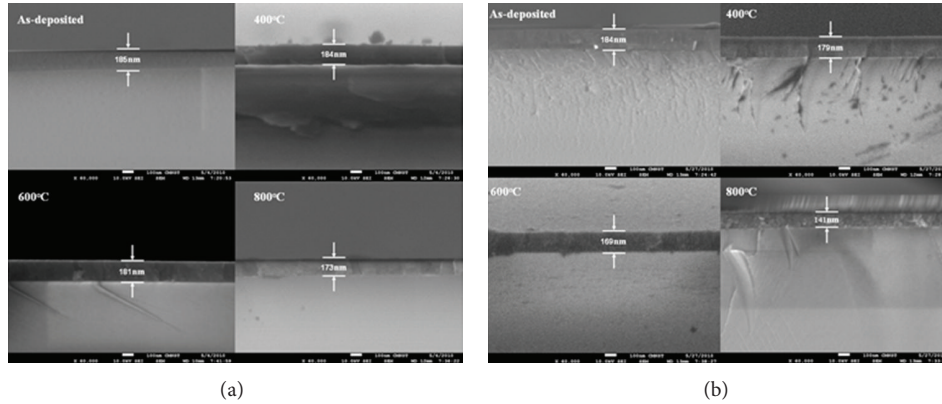


FIGURE 3: Cross-sectional view by SEM of the TiO_2 films from (a) Ti_3O_5 and (b) TiO_2 starting materials annealed at 400°C , 600°C , and 800°C .

film. This was due to the loss of oxygen and large thermal energy during annealing at temperatures of over 350°C [13]. According to the open literature, little further research was devoted to discuss the fluctuation of refractive index and the phenomenon of cutoff wavelength shift to longer wavelength when TiO_2 films from Ti_3O_5 starting material were annealed at above 400°C . The main aims of this research were to investigate the effect of annealing temperature on the theoretically explained reason for cutoff wavelength shift to long wavelength. We also compared with from TiO_2 starting material.

2. Experiment

TiO_2 films were deposited upon double-polishing sapphire substrate at room temperature by electron beam evaporation. Ti_3O_5 and TiO_2 were used as the starting materials, and the deposition rate was about 0.13 nm/s . The vacuum chamber was pumped to a base pressure of less than 5×10^{-5} torr before deposition, and the working pressure was kept at approximately 4×10^{-4} torr throughout the deposition process. During deposition, thickness controller with a quartz oscillator was used to monitor the thickness of TiO_2 films, which deposited at about 190 nm . Finally, TiO_2 films were annealed from 400°C to 800°C in step 200°C for 30 min by furnace in air environment. The crystallization of the film was analyzed by an X-ray diffraction meter (XRD). The thickness of the film was observed by a field emission scanning electron microscopy (JSM7000). The refractive index and transmittance were measured by n&k analyzer (n&k analyzer 1280). XPS surface analysis was performed using an Auger Electron Spectroscopy (JAMP9500F) employing an $\text{Mg K}\alpha$ X-ray source. The surface roughness was observed by atomic force microscopy (AFM). The root mean square (RMS) surface roughness values were obtained using the software which comes with the instrument.

3. Results and Discussion

Figure 1(a) presents the transmittance spectra of TiO_2 film from Ti_3O_5 starting material during thermal annealing. The

transmittance decreased weakly as the annealing temperature was increased to 400°C . In contrast, as the annealing temperature was increased to 600°C , the transmittance increased and the spectra shifted back to shorter wavelengths. On the other hand, the transmittance decreased slightly and the spectra shifted to longer wavelength as the annealing temperature was increased to 800°C . Figure 1(b) presents the transmittance spectra of TiO_2 film from TiO_2 starting material during thermal annealing. As the annealing temperature was increased to 400°C and 600°C , the transmittance decreased and the spectra shifted to longer wavelength. On the other hand, as the annealing temperature was increased to 800°C , the transmittance decreased and the spectra shifted to longer wavelength. Figure 2 plots the refractive index versus wavelength and annealing temperature. As shown in Figure 2(a), the refractive index rose as the annealing temperature was increased to 400°C but declined as the temperature was increased further from 400°C to 800°C . Such a variation was attributed to the loss of oxygen as the annealing temperature decreased below 400°C . The film contained some lower suboxides that were attributable to the titanium oxide [11]. As the annealing temperature was raised from 400°C to 800°C , the film captured oxygen from the air to yield the oxide. This finding is explained below with reference to XPS measurement. As shown in Figure 2(b), the refractive index rose as the annealing temperature increased to 800°C but declined as the annealing temperature decreased below 800°C . This finding is also explained below with reference to the XPS measurements. From measured results, we can find that the refractive index of as-deposited films from Ti_3O_5 starting material is higher than that of films as-deposited from TiO_2 starting material. In addition, it should be noted that the refractive indexes shown in Figure 2(b) fluctuate strongly as compared with those measured refractive indexes shown in Figure 2(a). This should be attributed to the fact that the deposited molecules had a higher packing density, such that the film was denser [9]. This finding is illustrated below with reference to SEM measurement. Thus, Ti_3O_5 material used as the starting material should be good choice for a high refractive index film. Figures 3(a) and 3(b) show the thickness of the TiO_2 films from Ti_3O_5 and TiO_2 starting

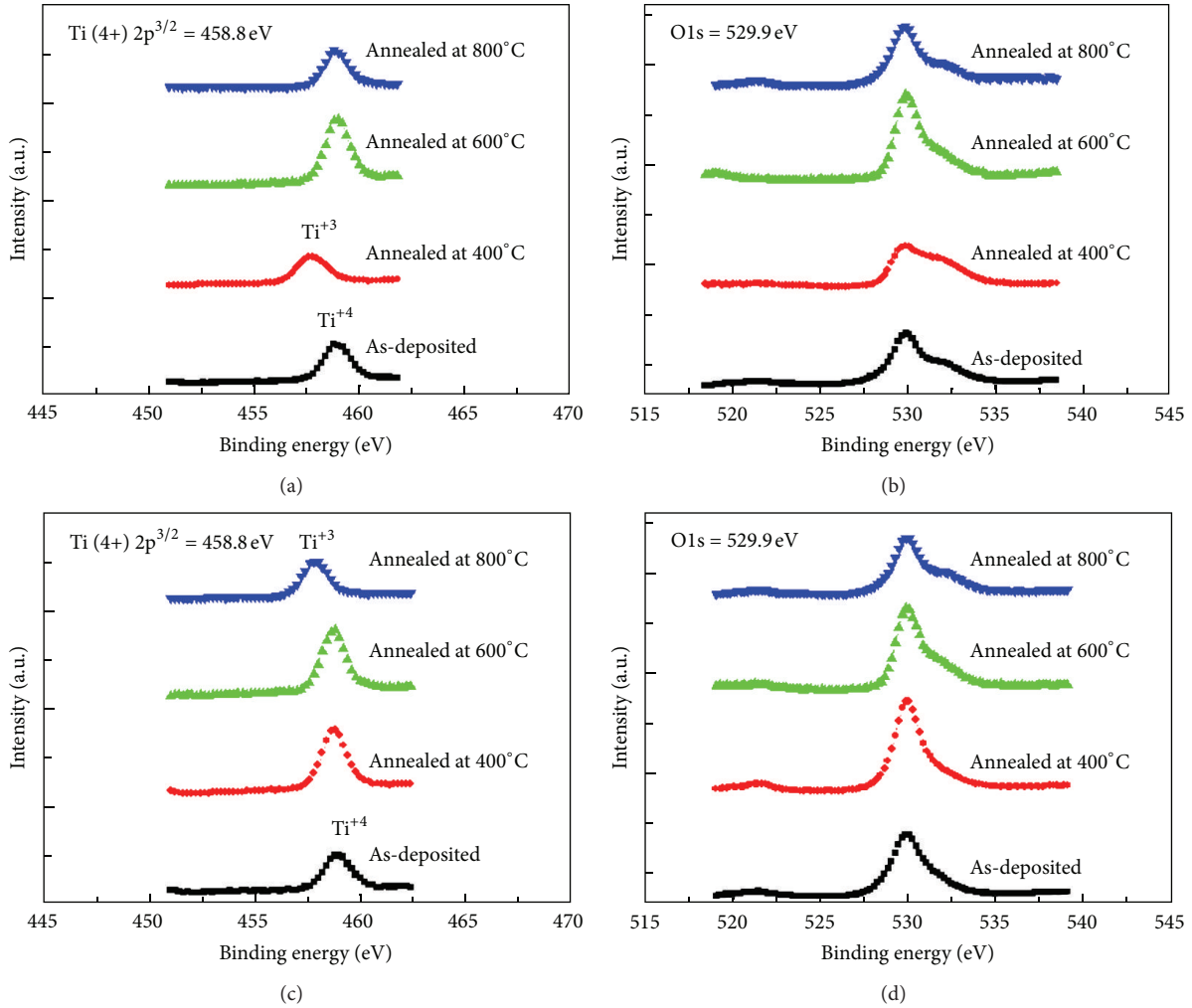


FIGURE 4: XPS spectra of TiO_2 films annealed at various temperatures: (a) $\text{Ti } 2p^{3/2}$ and (b) O1s from Ti_3O_5 starting material and (c) $\text{Ti } 2p^{3/2}$ and (d) O1s from TiO_2 starting material.

materials at different annealing temperatures, respectively. As shown in Figure 3(a), as the annealing temperature increased to 800°C , the loose film became less slim. On the other hand, as shown in Figure 3(b), as the annealing temperature increased to 800°C , the loose film became slimmer. Due to the aforementioned reason, from Figure 3(a), it is clear that the TiO_2 film from Ti_3O_5 starting material has higher packing density. In contrast, in Figure 3(b), it is apparent that the TiO_2 film has lower packing density.

As shown in Figure 4, X-ray photoelectron spectroscopy (XPS) measurement was used to certify both the binding energy of the $\text{Ti } 2p$ line and variation of the O1s line. The peaks at 458.8 and 457.8 eV in the spectra correspond to Ti^{4+} and Ti^{3+} , respectively [14]. Figure 4(a) shows that the binding energy of the $\text{Ti } 2p^{3/2}$ peak from 458.8 eV as-deposited, to 457.8 eV, 400°C annealed, corresponds to a transition from Ti^{4+} to Ti^{3+} ; this indicates that titanium oxides lost oxygen, exhibiting the properties of the lower suboxides. On the other hand, the binding energy (458.8 eV) of the film annealed at

600°C reveals that the film captured oxygen from the air to yield the oxide [11]. Figure 4(b) reveals that the O1s line (near 529.9 eV) varies with the annealing temperature. The peak at lower binding intensity, 529.9 eV, for the film annealed at 400°C is attributed to defective oxides. In contrast, the peak at higher binding energy, 529.9 eV, for the film annealed at 600°C is attributed to oxides. As shown in Figure 4(c), the $\text{Ti } 2p^{3/2}$ peak from 458.8 eV as-deposited, to 457.8 eV, 800°C annealed, corresponds to a transition from Ti^{4+} to Ti^{3+} ; this indicates that titanium oxides lost oxygen, exhibiting the properties of the lower suboxides. On the other hand, the binding energy (458.8 eV) of the film annealed at 600°C reveals that the film captured oxygen from the air to yield the oxide [14]. Figure 4(d) reveals that the O1s line (near 529.9 eV) varies with the annealing temperature. The peak at lower binding intensity, 529.9 eV, for the film annealed at 800°C is attributed to defective oxides. In contrast, the peak at higher binding intensity, 529.9 eV, for the film annealed at 600°C is attributed to oxides.

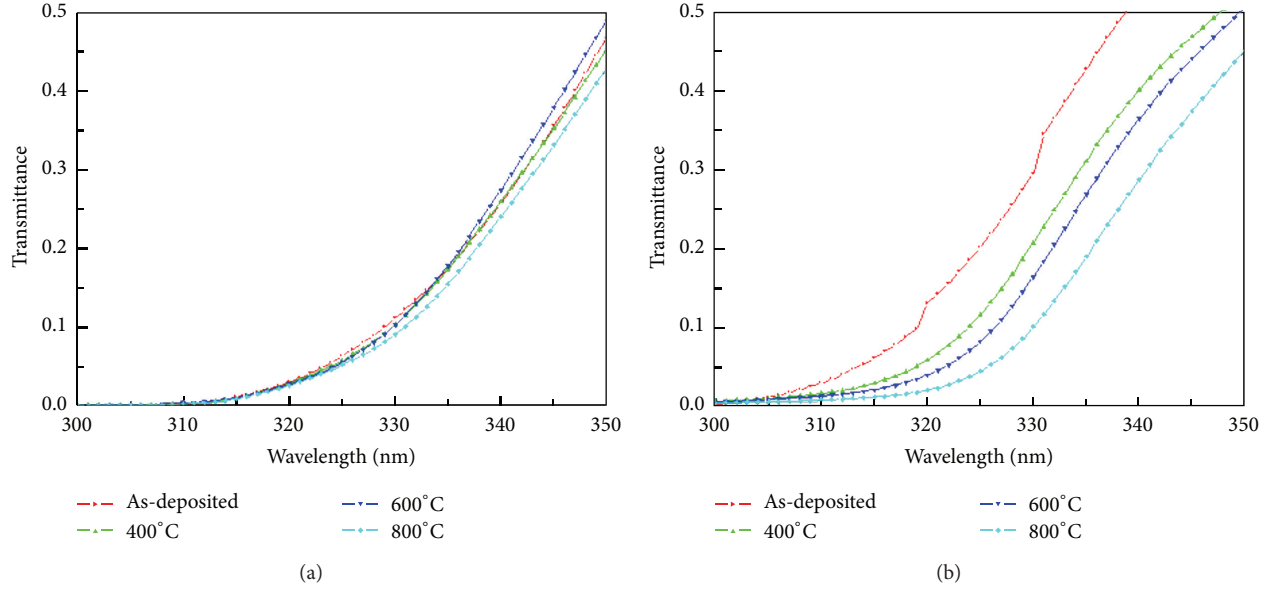


FIGURE 5: Partial enlarged drawing of transmittance spectra from (a) Ti_3O_5 and (b) TiO_2 starting materials in the wavelength region between 300 and 350 nm.

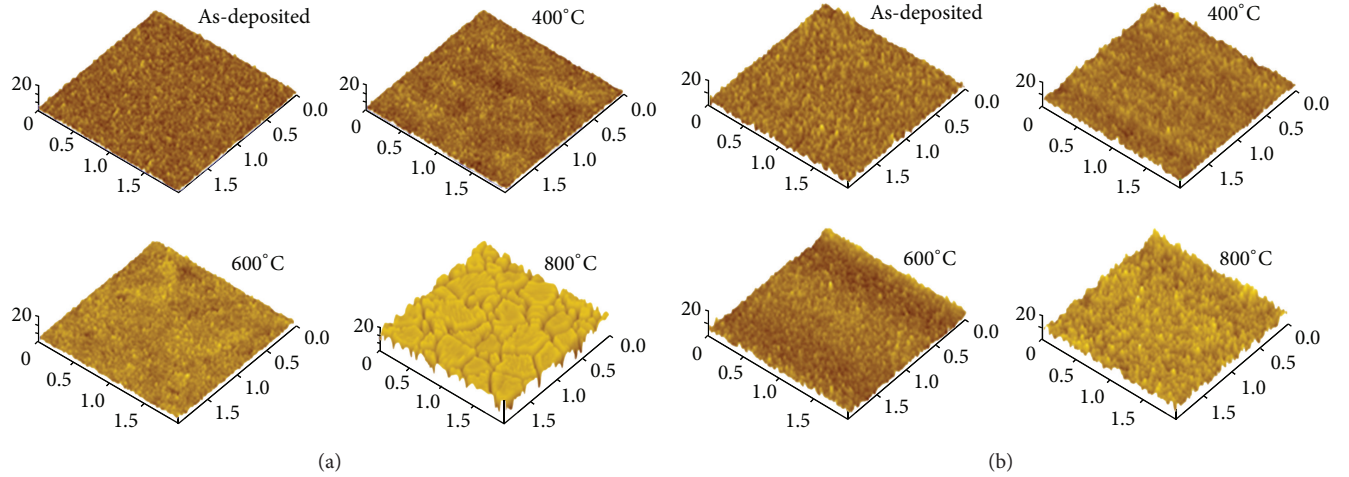


FIGURE 6: Surface morphology ($2 \times 2 \mu\text{m}$) by AFM of TiO_2 films from (a) Ti_3O_5 and (b) TiO_2 starting materials annealed at 400°C , 600°C , and 800°C .

In order to investigate the phenomenon of cutoff wavelength shift to longer wavelength, the partial enlarged drawing of transmittance spectra from Ti_3O_5 and TiO_2 starting material in the wavelength region between 300 and 350 nm is shown in Figure 5. As shown in Figure 5(a), the transmittance spectra indicate that the transmittance edge slightly shifts to longer wavelength with the annealing temperature increasing. Compared with TiO_2 starting material, the transmittance spectra indicate that the transmittance edge strongly shifts to longer wavelength with the same annealing temperature increasing as shown in Figure 5(b). It can be interpreted that both scattering and absorption loss increase as a result of surface roughness increase and absence of oxygen. The scattering loss results from surface roughness and bulk defects such as particles and microcracks. But the scattering loss posed by

surface roughness, namely, surface scattering loss (SSL), plays a principal role in general. If the value of the root mean square roughness is σ , we can deduce the transmission scattering loss that can be expressed as [15]

$$(\text{SSL})_t = T_0 \left\{ 1 - \exp \left[- \left(\frac{2\pi}{\lambda} \sigma (n_1 - n_0) \right)^2 \right] \right\}, \quad (1)$$

where T_0 is the transmittance of ideal smooth interface and n_0 and n_1 are the refractive index of interface bilateral dielectric. On the other hand, the relationship between absorption coefficient and concentration of free carriers can be written as [14]

$$a = \frac{Ne^2\lambda_0^2}{\epsilon_0 m^* 8\pi n c^3 \tau}, \quad (2)$$

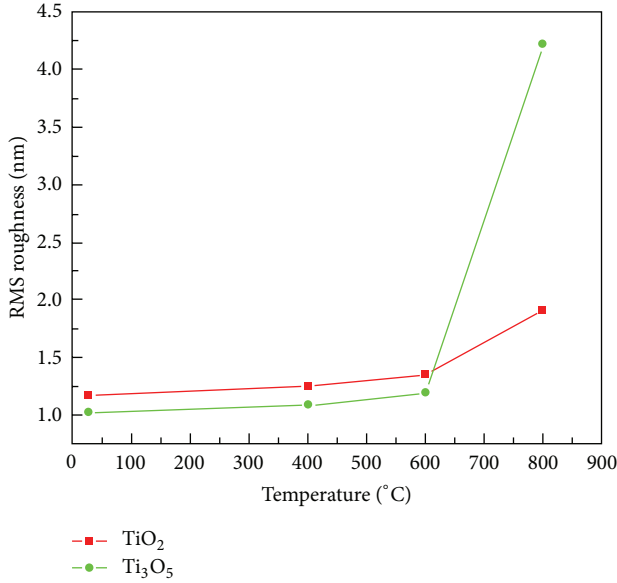


FIGURE 7: Influence of annealing temperature on RMS roughness of TiO₂ films from Ti₃O₅ and TiO₂ starting materials.

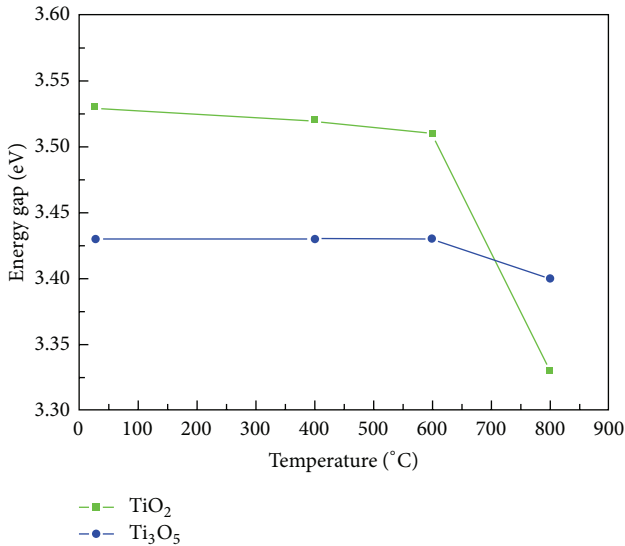


FIGURE 8: Optical band gap of as-deposited, annealed at 400°C, 600°C, and 800°C.

where a is absorption coefficient, N is the concentration of free carrier, n is the refractive index, m^* is the effective mass of free carrier, τ is relax time, and λ_0 is absorption wavelength. So the total optical loss I_{loss} of the transmittance at cutoff wavelength should consist of absorption α_a and scattering (SSL)_t:

$$I_{\text{loss}} = \alpha_a + (\text{SSL})_t. \quad (3)$$

Thus, based on the analysis above, we can conclude that the cutoff wavelength shift results from absence of oxygen

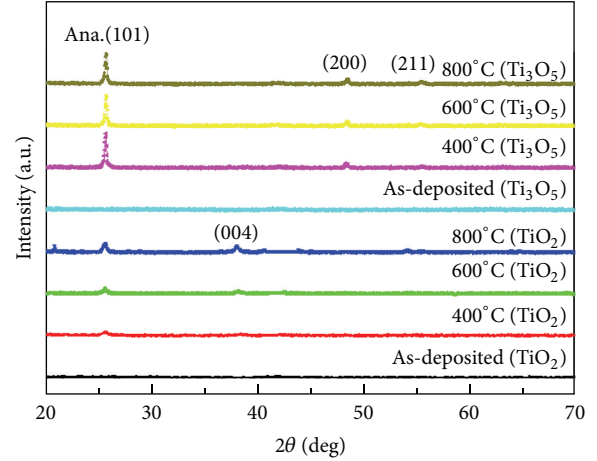


FIGURE 9: X-ray diffraction patterns of TiO₂ films from Ti₃O₅ and TiO₂ starting materials annealed at different temperature.

and scattering of rough surface. Clearly, the cutoff wavelength shift has great dependence on the surface topography. Therefore, we can acquire important information of surface topography. The evolution of surface topography by AFM of TiO₂ films from Ti₃O₅ and TiO₂ starting materials was illustrated in Figures 6(a) and 6(b), respectively, and the experimental results evidently indicated that surface topography depends strongly on the thermal treatment. The relationship between the root mean square (RMS) roughness by AFM and annealing temperature is shown in Figure 7. It is found that RMS of TiO₂ films from Ti₃O₅ starting material increases from 1.02 nm as-deposited to 1.08 nm at 400°C, and if the annealing temperatures increase further, the RMS value increases as well and reaches 4.22 nm for 800°C. It is also found that the grain size also grows from 40 nm to 101 nm. In contrast, it is found that RMS of TiO₂ films from TiO₂ starting material increases from 1.17 nm as-deposited to 1.25 nm at 400°C, and if the annealing temperatures increase further, the RMS value increases as well and reaches 1.91 nm for 800°C. The grain size also grows from 45 nm to 66 nm. Due to the aforementioned reason, we can find that TiO₂ film from TiO₂ starting material is very serious cutoff wavelength shift with the annealing temperature increasing. In contrast, the TiO₂ film from Ti₃O₅ starting material is less cutoff wavelength shift with the same annealing temperature increasing.

As shown in Figure 8, the direct optical band gap values (E_g) are 3.43, 3.43, and 3.4 eV for TiO₂ films from Ti₃O₅ starting material annealed at 400°C, 600°C, and 800°C, respectively. On the other hand, the direct optical band gap values (E_g) are 3.52, 3.51, and 3.33 eV for TiO₂ films from TiO₂ starting material annealed at 400°C, 600°C, and 800°C, respectively. From the graph, it is clear that the optical band gap of TiO₂ films is obviously affected by the absence of oxygen and scattering of rough surface. Specifically, the optical band gap of TiO₂ films from TiO₂ starting material from 3.53 eV as-deposited, to 3.33 eV, 800°C annealed, indicates serious absence of oxygen. In contrast, the optical band gap of TiO₂ films from Ti₃O₅ starting material from 3.43 eV

as-deposited, to 3.4 eV, 800°C annealed, indicates serious scattering of rough surface.

Figure 9 presents the X-ray diffraction patterns of the TiO₂ film from TiO₂ and Ti₃O₅ starting materials deposited onto the sapphire substrate and annealed at different temperature. The films are amorphous before annealing. At 400°C, 600°C, and 800°C the preferred (101) orientation reveals that the film exhibited a single phase anatase structure [11, 13, 14, 16]. In addition, there were two weak diffraction peaks, anatase (200) and (211), appearing in the pattern of TiO₂ films annealed at 400°C, 600°C, and 800°C. The crystallization of the TiO₂ films was evidently improved by annealing. After annealing, the structure of the TiO₂ film was in the anatase phases with the preferential crystalline orientation of (101). We can assume that the as-deposited films are amorphous due to the low mobility of molecules depositing on the cold substrate. We can find that the TiO₂ films from Ti₃O₅ starting material have strong diffraction peaks at 400°C, 600°C, and 800°C.

4. Conclusion

In this study, we deposited TiO₂ films from Ti₃O₅ and TiO₂ starting materials onto sapphire substrate with electron beam evaporation and then annealed as the temperature increased from 400°C to 800°C. We find that the refractive index of as-deposited films from Ti₃O₅ starting material is higher than that of films as-deposited from TiO₂ starting material. In addition, during thermal annealing, the refractive index fluctuates slightly as compared with TiO₂ films from TiO₂ starting material. This should be attributed to the fact that the deposited molecules had a higher packing density, such that the film was denser. The transmittance spectra of TiO₂ films from Ti₃O₅ starting material indicate that transmittance edge slightly shifts to longer wavelength with the annealing temperature increasing. Compared with TiO₂ starting material, the transmittance spectra indicate that the transmittance edge strongly shifts to longer wavelength with the same annealing temperature increasing. These findings should be attributed to the absence of oxygen and scattering of rough surface. The optical band gap of TiO₂ films from TiO₂ starting material from 3.53 eV as-deposited, to 3.33 eV, 800°C annealed, indicates serious absence of oxygen. In contrast, the optical band gap of TiO₂ films from Ti₃O₅ starting material from 3.43 eV as-deposited, to 3.4 eV, 800°C annealed, indicates serious scattering of rough surface.

References

- [1] S. J. Chang, C. F. Shen, M. H. Hsieh et al., "Nitride-based LEDs with a hybrid Al mirror +TiO₂/SiO₂ DBR backside reflector," *Journal of Lightwave Technology*, vol. 26, no. 17, pp. 3131–3136, 2008.
- [2] C. Yang, H. Fan, Y. Xi, J. Chen, and Z. Li, "Effects of depositing temperatures on structure and optical properties of TiO₂ film deposited by ion beam assisted electron beam evaporation," *Applied Surface Science*, vol. 254, no. 9, pp. 2685–2689, 2008.
- [3] Y.-C. Liu, Y.-F. Lu, Y.-Z. Zeng, C.-H. Liao, J.-C. Chung, and T.-Y. Wei, "Nanostructured mesoporous titanium dioxide thin film prepared by sol-gel method for dye-sensitized solar cell," *International Journal of Photoenergy*, vol. 2011, Article ID 619069, 2011.
- [4] A. D. Barros, K. F. Albertin, J. Miyoshi, I. Doi, and J. A. Diniz, "Thin titanium oxide films deposited by e-beam evaporation with additional rapid thermal oxidation and annealing for ISFET applications," *Microelectronic Engineering*, vol. 87, no. 3, pp. 443–446, 2010.
- [5] J. Shin, K. Lee, J. Koh et al., "Hydroxyapatite coatings on nanotubular titanium dioxide thin films prepared by radio frequency magnetron sputtering," *Journal of Nanoscience and Nanotechnology*, vol. 13, no. 8, pp. 5807–5810, 2013.
- [6] E. D. Palik, *Handbook of Optical Constants of Solids*, Academic Press, Washington, DC, USA, 1991.
- [7] Ö. Duyar, F. Placido, and H. Zafer Durusoy, "Optimization of TiO₂ films prepared by reactive electron beam evaporation of Ti₃O₅," *Journal of Physics D*, vol. 41, no. 9, Article ID 095307, 2008.
- [8] F. Waibel, E. Ritter, and R. Linsbod, "Properties of TiO_x films prepared by electron-beam evaporation of titanium and titanium suboxides," *Applied Optics*, vol. 42, no. 22, pp. 4590–4593, 2003.
- [9] H. Selhofer, E. Ritter, and R. Linsbod, "Properties of titanium dioxide films prepared by reactive electron-beam evaporation from various starting materials," *Applied Optics*, vol. 41, no. 4, pp. 756–762, 2002.
- [10] F. X. Wang, C. K. Hwangbo, B. Y. Jung, J. H. Lee, B. H. Park, and N. Y. Kim, "Optical and structural properties of TiO₂ films deposited from Ti₃O₅ by electron beam," *Surface and Coatings Technology*, vol. 201, no. 9–11, pp. 5367–5370, 2007.
- [11] C.-C. Lee, H.-C. Chen, and C.-C. Jaing, "Effect of thermal annealing on the optical properties and residual stress of TiO₂ films produced by ion-assisted deposition," *Applied Optics*, vol. 44, no. 15, pp. 2996–3000, 2005.
- [12] H.-C. Chen, C.-C. Lee, C.-C. Jaing, M.-H. Shiao, C.-J. Lu, and F.-S. Shieu, "Effects of temperature on columnar microstructure and recrystallization of TiO₂ film produced by ion-assisted deposition," *Applied Optics*, vol. 45, no. 9, pp. 1979–1984, 2006.
- [13] C.-C. Jaing, H.-C. Chen, and C.-C. Lee, "Effects of thermal annealing on titanium oxide films prepared by ion-assisted deposition," *Optical Review*, vol. 16, no. 3, pp. 396–399, 2009.
- [14] J. Yao, J. Shao, H. He, and Z. Fan, "Effects of annealing on laser-induced damage threshold of TiO₂/SiO₂ high reflectors," *Applied Surface Science*, vol. 253, no. 22, pp. 8911–8914, 2007.
- [15] G. Tian, L. Dong, C. Wei, J. Huang, H. He, and J. Shao, "Investigation on microstructure and optical properties of titanium dioxide coatings annealed at various temperature," *Optical Materials*, vol. 28, no. 8–9, pp. 1058–1063, 2006.
- [16] X. Cheng, S. Hu, P. Zeng, T. Kuang, G. Xie, and F. Gao, "Structure and properties of TiO₂ films prepared by ion beam assisted deposition," *Surface and Coatings Technology*, vol. 201, no. 9–11, pp. 5552–5555, 2007.